

IntechOpen

Chemical Reactions in Inorganic Chemistry

Edited by Saravanan Chandraleka



CHEMICAL REACTIONS IN INORGANIC CHEMISTRY

Edited by **Saravanan Chandraleka**

Chemical Reactions in Inorganic Chemistry

<http://dx.doi.org/10.5772/65823>

Edited by Saravanan Chandraleka

Contributors

Chandraleka Saravanan, Bhaskar Biswas, Chaoqun Ye, Ming-Der Su, Aijian Wang, Wei Zhao

© The Editor(s) and the Author(s) 2018

The rights of the editor(s) and the author(s) have been asserted in accordance with the Copyright, Designs and Patents Act 1988. All rights to the book as a whole are reserved by INTECHOPEN LIMITED. The book as a whole (compilation) cannot be reproduced, distributed or used for commercial or non-commercial purposes without INTECHOPEN LIMITED's written permission. Enquiries concerning the use of the book should be directed to INTECHOPEN LIMITED rights and permissions department (permissions@intechopen.com). Violations are liable to prosecution under the governing Copyright Law.



Individual chapters of this publication are distributed under the terms of the Creative Commons Attribution 3.0 Unported License which permits commercial use, distribution and reproduction of the individual chapters, provided the original author(s) and source publication are appropriately acknowledged. If so indicated, certain images may not be included under the Creative Commons license. In such cases users will need to obtain permission from the license holder to reproduce the material. More details and guidelines concerning content reuse and adaptation can be found at <http://www.intechopen.com/copyright-policy.html>.

Notice

Statements and opinions expressed in the chapters are those of the individual contributors and not necessarily those of the editors or publisher. No responsibility is accepted for the accuracy of information contained in the published chapters. The publisher assumes no responsibility for any damage or injury to persons or property arising out of the use of any materials, instructions, methods or ideas contained in the book.

First published in London, United Kingdom, 2018 by IntechOpen

eBook (PDF) Published by IntechOpen, 2019

IntechOpen is the global imprint of INTECHOPEN LIMITED, registered in England and Wales, registration number: 11086078, The Shard, 25th floor, 32 London Bridge Street

London, SE19SG – United Kingdom

Printed in Croatia

British Library Cataloguing-in-Publication Data

A catalogue record for this book is available from the British Library

Additional hard and PDF copies can be obtained from orders@intechopen.com

Chemical Reactions in Inorganic Chemistry

Edited by Saravanan Chandraleka

p. cm.

Print ISBN 978-1-78923-146-5

Online ISBN 978-1-78923-147-2

eBook (PDF) ISBN 978-1-83881-251-5

We are IntechOpen, the first native scientific publisher of Open Access books

3,450+

Open access books available

110,000+

International authors and editors

115M+

Downloads

151

Countries delivered to

Our authors are among the
Top 1%

most cited scientists

12.2%

Contributors from top 500 universities



WEB OF SCIENCE™

Selection of our books indexed in the Book Citation Index
in Web of Science™ Core Collection (BKCI)

Interested in publishing with us?
Contact book.department@intechopen.com

Numbers displayed above are based on latest data collected.
For more information visit www.intechopen.com



Meet the editor



Dr. Chandraleka Saravanan is currently working as an assistant professor at the Department of Chemistry, Urumu Dhanalakshmi College, Tiruchirappalli, Tamil Nadu, India. She has experience in the fields of coordination chemistry and bioinorganic chemistry. Her current research focuses on metal complex synthesis, structural characterization, and their utility in pharmacological and biological applications. She has published 20 research papers and 1 book on *Transition Metal Complexes: Biological Activity*. She guided eight MPhil candidates and participated in summer school on materials science. She has presented 16 research papers on national and international conferences/seminars. She is an editorial board member of national and international journals and an examiner committee member of MSc, MPhil, and PhD in Chemistry.

Contents

Preface XI

- Chapter 1 **Introductory Chapter: An Outline of Chemical Reagents and Reactions in Inorganic Synthesis 1**
Chandraleka Saravanan and Bhaskar Biswas
- Chapter 2 **Porphyrin and Phthalocyanine Covalently Functionalized Graphene and Carbon Nanotube Nanohybrids for Optical Limiting 9**
Aijian Wang and Wei Zhao
- Chapter 3 **Sol-Gel Processes of Functional Powders and Films 31**
Chao-Qun Ye
- Chapter 4 **The Effect of Substituent on Molecules That Contain a Triple Bond Between Arsenic and Group 13 Elements: Theoretical Designs and Characterizations 51**
Jia-Syun Lu, Ming-Chung Yang, Shih-Hao Su and Ming-Der Su
- Chapter 5 **Theoretical Investigations of Mechanisms for the Reactions of Seven-Member Ring N-Heterocyclic Carbene and Its Heavier Analogues 75**
Zheng-Feng Zhang, Ling-Hsuan Liu and Ming-Der Su

Preface

A chemical reagent is a molecule or compound, which helps to bring a chemical change during mixing with another molecule or is added to see if a reaction occurs or not. Although the terms reactant and reagent are often used interchangeably, a reactant is more specifically a “substance that is consumed in the course of a chemical reaction.” Before entering the main context of the write-up, it is better to present few sentences about the synthetic aspect in inorganic chemistry. Inorganic chemists have long been enthralled by the magnificent colors of inorganic compounds. From the historical perspective, in the early 15,000 BC, cave painters used iron oxides for the sources of yellows and reds, aluminum silicates for greens, and manganese oxide for browns. By 3000 BC, Egyptian and Syrian artisans and jewelers were staining metal surfaces with inorganic salts derived from ground minerals and alloys. The colors obtained mostly depended on the types of transition metals contained in the minerals and on their combinations. One of the first synthetic pigments, Egyptian Blue, $\text{CaCuSi}_4\text{O}_{10}$, was prepared by heating malachite/sand (quartz or silica) mixtures to a temperature of 800–900°C. Later in the fifteenth to eighteenth centuries, metal-containing pigments, such as copper carbonate and the brilliant ferric ferrocyanide coordination complex, Prussian Blue, $\text{Fe}_4[\text{Fe}(\text{CN})_6]_3$, were synthesized for use in the textile industry. Iron oxides, lead chromates, and the ubiquitous white pigment, titanium dioxide, are just a few of the many inorganic compounds that are still important in this industry today. The existence of ionic forces including some weak forces primarily accounts on the distinction of inorganic compounds than others.

A purely inorganic compound refers to a class of compound that does not contain a carbon to hydrogen (C-H) bond. Not all, but most inorganic compounds contain a metal. Actually, metal ions with labile reaction centers are generally used as geometry setters. For this reason, inorganic compounds have an overwhelming amount of applications and practical uses in the real world. Thus, in the recent spurt in research and advance academic framework, inorganic compounds are an exciting area that have important implications for the rational design of functional materials to be used as catalysts, conducting materials, molecular magnetic materials, nonlinear optical materials, liquid crystals, chemical sensors, and molecular recognitions. Syntheses of molecules and materials are a very important aspect behind the development of science, especially in chemistry. The attempts to synthesize new molecules and materials have always depended on the experience and extrapolation of the existing knowledge to new situations and new synthesis of molecules. The strategies adopted in syntheses of molecules and materials have undergone an enormous expansion in recent times, and research in inorganic synthesis has opened up a new vista in this direction. This book describes an overview of chemical reagents used in inorganic chemical reactions for the synthesis of different compounds including coordination, transition metal, organometallic, clus-

ter, bioinorganic, and solid-state compounds. It will be helpful for the graduate students, teachers, researchers, and chemistry professionals who are interested to fortify and expand their knowledge about sol-gel preparation and application, porphyrin and phthalocyanine, carbon nanotube nano hybrids, triple bond between arsenic and group 13 elements, and N-heterocyclic carbene and its heavier analogues.

The book comprises a total of five chapters from multiple contributors around the world including China, India, and Taiwan. I am grateful to all the contributors and leading experts for the submission of their stimulating and inclusive chapters in the preparation of the edited volume to bring the book on *Chemical Reactions in Inorganic Chemistry*. I offer our special thanks and appreciation to Ms. Romina Rovani, Publishing Process Manager, for her encouragement and help and IntechOpen publisher in bringing out the book in the present form. I am also indebted to the Secretary and Principal of Urumu Dhanalakshmi College for their concern, efforts, and support in the task of publishing this volume.

Dr. Chandraleka Saravanan

Assistant Professor

Department of Chemistry

Urumu Dhanalakshmi College

Kattur, Tiruchirappalli

Tamil Nadu, India

Introductory Chapter: An Outline of Chemical Reagents and Reactions in Inorganic Synthesis

Chandraleka Saravanan and Bhaskar Biswas

Additional information is available at the end of the chapter

<http://dx.doi.org/10.5772/intechopen.76536>

1. Introduction

A substance that is used in a chemical reaction to detect, measure, examine, or produce other substances is known as chemical reagent. A reagent in chemical science is a “substance or compound that is added to a system in order to bring a chemical reaction or is added to check whether a reaction is occurred or not.” Such a reaction is used to confirm the detection of the presence of another substance. Although the terms “reactant and reagent” are often used interchangeably, a reactant is more specifically a “substance that is consumed in the course of a chemical reaction.” Commonly, the involvement of solvents and catalysts in the course of a chemical reaction is not considered as reactants. Small organic molecules and metal salts/compounds in organic chemistry play a significant role in different organic reactions of laboratory and industrial importance [1].

Grade of chemical reagents remains very important in inorganic synthesis. Purity of a chemical agent can also be expressed in terms of the grade. Chemical reagents in scientific community are commonly found as spectroscopic grade, analytical grade (A.R. grade), synthetic grade, and laboratory grade (L.R. grade). Depending on the nature of uses, specially qualitative or quantitative, one can select the grade of reagents. Whatever the chemical substances we commonly use, a minimum quality must be maintained, and the purity of the chemical substances is determined by few organizations of international standard like ASTM International.

Inorganic chemistry, which is serving as a fundamental branch of chemistry, deals with the synthesis and behavior of inorganic and organometallic compounds. This field covers all chemical compounds consisting of most of the chemical bonding comprising ionic, covalent, coordinate, μ -bonding, δ -bonding, H-bonding, weak interactions, and so on. The important aspects of chemical bonding in inorganic compounds reflect their physicochemical properties

and the materialistic application in industrial catalysis, therapeutic agents, optical materials, magnetic materials, and conducting materials [2]. This chapter describes an overview of chemical reagents using inorganic chemical reactions for the synthesis of different compounds including coordination, organometallic, cluster, bioinorganic, solid state compounds, and so on.

2. Inorganic reaction types

A chemical reaction is basically a process in which an integral chemical change of a reactant is taken place during the conversion of reactant to products. In the chemical reactions, electronic motion involves to head a bond making and breaking. Different types of chemical reactions in inorganic chemistry may be classified more than a single way. Only some of the fundamental broad inorganic chemical reactions are categorized in the following.

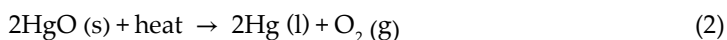
2.1. Combination reactions

This is a type of a chemical reaction in which two or more reactants react themselves to produce a product. Elemental sulfur reacts with molecular oxygen to form sulfur dioxide is an example of combination reaction.



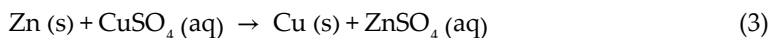
2.2. Decomposition reactions

Often, decomposition reactions are considered as an opposite type of combination reactions. A chemical entity in the decomposition reaction breaks down into two or more substances. Decomposition usually results from electrolysis or heating. An example of a decomposition reaction is the breakdown of mercury(II) oxide into its component elements.



2.3. Displacement reactions

A displacement reaction is occurred during the replacement of an atom or ion with another atom or ion in a compound. An example of a single displacement reaction is the displacement of copper ion in a copper sulfate solution by zinc metal ion to form zinc sulfate.



3. Classification of inorganic compounds

Inorganic chemistry includes different types of compounds comprising coordination compounds, simple metal compounds, organometallic compounds, cluster molecules, biological

compounds, supramolecules, coordination polymers, catalysts, magnetic compounds, and others [3]. A brief discussion on some classes of inorganic compounds is presented.

3.1. Coordination compounds

Coordination compounds cover a wide fundamental area in inorganic chemistry and primarily deal with coordination bonding between a ligand and a metal ion. Classical coordination compounds feature metals bound to “lone pairs” of electrons residing on the main group atoms of ligands such as H_2O , NH_3 , Cl^- , and CN^- . In modern coordination compounds, large numbers of ligands with different coordination motifs are available. Most of the metal complexes contain principally 3D metal ions with different ligand backbones. A. Werner, the founder of coordination chemistry showed different classes of coordination molecules. He also classified the ligands as classical/Werner type and non-classical/non-Werner type ligands. Commonly, in coordination compounds ligands are dominated by the elements belonging to groups 13–17 [4]. On the other hand, Schiff bases, a very common and widely used ligand systems, named after H. Schiff, are the condensation products between primary amines and aldehydes or ketones ($\text{RCH}=\text{NR}'$, where R and R' represent alkyl and aryl substituents), which are used for the preparation of complex compounds [5].

3.2. Transition metal compounds

Compounds with metal ions from group 4 to 11 are considered transition metal compounds. Compounds with a metal from group 3 or 12 are sometimes also incorporated into this group but often classified as main group compounds. Transition metal compounds also show rich coordination geometry, varying from coordination number 3 to 12, although tetrahedral, square planar, square pyramidal/trigonal bipyramid, and octahedral geometry for coordination geometries are commonly seen. A large number of transition elements are primarily responsible for carrying out different bio-functions in living systems like iron in heme proteins, zinc in carbonic anhydrase enzyme in respiration, Fe & Mo in nitrogen fixation, Mn in oxygen evolving complex in photosynthesis, Co in vitamin B_{12} , Cu in hemocyanin and different metallo-enzymes, and so on [6, 7].

3.3. Organometallic compounds

Usually, organometallic compounds are considered as a class of compound which contains at least one M–C bond which is exclusively covalent in character [8]. The metal (M) in these species can either be a main group element or a transition metal. Operationally, the definition of an organometallic compound is also more relaxed to include highly lipophilic complexes such as metal carbonyls, metal nitrosyls, and even metal alkoxides. These compounds have drawn considerable interest mainly as homogeneous and heterogeneous catalysts.

3.4. Cluster compounds

Cluster compounds can be classified as metallic cluster, non-metallic cluster, and metal complex cluster. Clusters can be found in all classes of chemical compounds. According to the

commonly accepted definition, a cluster consists minimally of a triangular set of atoms that are directly bonded to each other, but metal-metal bonded di-/tri-/polymetallic complexes are highly relevant to the area. Clusters occur in “pure” inorganic systems, organometallic chemistry, main group chemistry, and bioinorganic chemistry. The distinction between very large clusters and bulk solids is increasingly blurred. Few examples are $\text{Fe}_3(\text{CO})_{12}$, $\text{B}_{10}\text{H}_{14}$, $[\text{Mo}_6\text{Cl}_{14}]^{2-}$, and $4\text{Fe}-4\text{S}$.

3.5. Bioinorganic compounds

Bioinorganic compounds are one of the most significant classes of a compound in chemical science, which are not only integrally related to the basic processes of nature but also provided significant insights into exploring the chemistry in living world [9]. It is a branch of chemistry, which deals with the interface between chemistry and biology. Starting from DNA to RNA to photosynthesis to oxygen transport and storage to nitrogen fixation, each and every parts of the living world are engrossed with the bioinorganic compounds. Traditional bioinorganic chemistry focuses on electron- and energy-transfer in proteins relevant to respiration. Medicinal inorganic chemistry includes the study of both non-essential and essential elements with applications to diagnosis and therapies.

When bioorganic molecules or drugs are bound to metal ions, there is a drastic change in their biomimetic properties, therapeutic effects, and pharmacological properties. One such remarkable molecule is amino acid, and they form complexes with metal atoms and exhibit significant biological and enzymatic activities. Essential metal ions and their complexes are found to have antitumor, antimicrobial, cytotoxic, and anti-HIV activity [10]. It was, therefore, considered worthwhile to study the complexation and to determine the biological activity of these new complexes.

3.6. Solid state compounds

This important area focuses on structure [11], bonding, and the physical properties [12] of materials. In practice, solid state inorganic chemistry uses techniques such as crystallography to gain an understanding of the structure and structural aspects that result from collective interactions between the subunits of the solid. Metals and their alloys or intermetallic derivatives are included in solid state chemistry. Related fields are condensed matter physics, mineralogy, and materials science. Examples are silicon chips, zeolites, and $\text{YBa}_2\text{Cu}_3\text{O}_7$.

4. Characterization of inorganic compounds

4.1. Solubility test

Solubility is one of the basic parameters that help to understand the properties of a compound. The synthesized compounds are generally tested for their solubility in various polar

solvents like water, ethanol, methanol, dimethyl sulfoxide, and some nonpolar solvents like hexane, ethylacetate, benzene, etc.

4.2. Melting point

Melting point determination for any compound helps to identify the level of reactivity in solid state for any synthesized ligands and metal complexes. It also helps to predict the molecular composition of the complexes.

4.3. CHN analysis

Elemental analysis remains an important method to study the nature of elements (especially C, H, N, and O) exist in compounds. The analysis on the abundance of carbon, nitrogen and hydrogen in a compound also helps to determine the class of compounds in the scientific literature.

5. Structural characterization of metal complexes

Various spectroscopic methods are available in the determination of proposed structures for inorganic complexes. Among these, elemental analyses, FT-IR, UV-Vis, NMR, EPR, mass spectrometry, and thermogravimetric analysis are the most common techniques and widely used globally. But, the most authenticated technique in the determination of detail structural geometry is single crystal X-ray diffraction study. This particular analytical tool helps to locate the atomic position in a 3D structure with an absolute precise manner.

5.1. Electronic spectroscopy

The UV-Vis spectra of all the complexes are recorded in spectrophotometer using different solvents in the wave range of 200–1100 nm.

5.2. Magnetic susceptibility

Magnetic susceptibility measurements of the complexes in the solid state are determined by the Gouy balance at room temperature using metal as the calibrant.

5.3. Molar conductivity

The molar conductivity is measured with a conductivity meter.

5.4. Infrared spectroscopy (IR)

IR spectral analysis is one of the most widely used analytical tools, which is utilized to assign different functional chromophores in the molecule. Incorporation of ligand with metal ions

can be easily detected to draw a simple comparison between IR spectra of free ligand and compound. The principle involved during this spectral analysis is to examine the changes in stretching modes.

5.5. ^1H NMR spectroscopy

Proton nuclear magnetic resonance is probably the best analytical method to determine the geometry and structural backbone for a chemical species. Further, the involvement of the ligand with metal ions in the formation of metal complexes can also be predicted with this technique. The chemical shifts associated with the location of H-atom in the skeletal of ligand remain very important in different applications in material sciences such as proton transfer mechanism and metal organic framework.

5.6. ESR spectroscopy

Electron spin resonance spectral technique is one of the fundamental techniques in detecting the spin state of metal ion or free ligand in inorganic compounds. It actually helps to determine the important aspects of chemical bonding along with significant illumination on structural features for metal complexes. Not only the structural part, but also the generation of ligand centered radical in different organic transformations of laboratory and industrial significance during the investigation of catalytic pathways can also be defined with this particular analytical technique. ESR measurements for the inorganic complexes at different temperatures and in different phases bring additional importance to this technique.

5.7. Thermal analysis

The thermal behavior of the synthesized complexes has been studied to establish different decomposition processes and to confirm the proposed stoichiometry. The thermal behavior of synthesized complexes was characterized on the basis of TGA/DTG and DTA method. Thermal analysis plays an important role in studying the stability, melting point, structure, and decomposition properties of the metal complexes.

5.8. Single crystal X-ray diffraction analysis

The most authenticated way to determine the 3D structure of inorganic complexes is single crystal X-ray diffraction study. It helps to locate the perfect atomic position in a molecule.

Author details

Chandraleka Saravanan¹ and Bhaskar Biswas^{2*}

*Address all correspondence to: icbbiswas@gmail.com

1 Department of Chemistry, Urumu Dhanalakshmi College, Tiruchirppalli, India

2 Department of Chemistry, Surendranath College, Kolkata, India

References

- [1] IUPAC. Compendium of chemical terminology. In: McNaught AD, Wilkinson A, editors. The Gold Book. 2nd ed. Cambridge, UK: Royal Society of Chemistry; 1997
- [2] McCoy M, Reisch M, Tullo AH. Facts & figures of the chemical industry. Chemical and Engineering News. 2006;**84**:35
- [3] Lehn JM. Supramolecular Chemistry: Concepts and Perspectives. Weinheim: VCH; 1995. ISBN: 3-527-29311-6
- [4] Greenwood NN, Earnshaw A. Chemistry of the Elements. 2nd ed. Butterworth-Heinemann; 2nd ed. Oxford, Boston: Pergamon Press; 1997
- [5] Dhar DN, Taploo CL. Schiff bases and their applications. Journal of Scientific and Industrial Research. 1982;**41**:501-506
- [6] Paterson JW. Citation classic – The pharmacodynamics and metabolism of propranolol in man. Clinical Practice. 1982;**9**:20-22
- [7] Parashar RK, Sharma RC, Kumar A, et al. Stability studies in relation to IR data of some Schiff base complexes of transition metals and their biological and pharmacological studies. Inorganica Chimica Acta. 1988;**151**:201-208
- [8] Elschenbroich C, Salzer A. Organometallics: A Concise Introduction. 2nd ed. Weinheim: Wiley-VCH; 1992. ISBN: 3527281649
- [9] Lippard SJ, Berg JM. Principles of Bioinorganic Chemistry. Mill Valley, CA: University Science Books; 1994. ISBN: 0-935702-73-3
- [10] Li R, George LK, Fred CE, Chen X, Gong B, Dominguez JN, Davidson E, Kurzban G, Miller RE, Nuzum EO, Rosenthal PJ, McKerrow JH. In vitro antimalarial activity of chalcones and their derivatives. Journal of Medicinal Chemistry. 1995;**38**:5031-5037
- [11] Wells AF. Structural Inorganic Chemistry. Oxford: Clarendon Press; 1984
- [12] Wilkins RG. Kinetics and Mechanism of Reactions of Transition Metal Complexes. 2nd ed. Wiley-VCH; 1991. ISBN: 3-527-28389-7

Porphyrin and Phthalocyanine Covalently Functionalized Graphene and Carbon Nanotube Nano hybrids for Optical Limiting

Aijian Wang and Wei Zhao

Additional information is available at the end of the chapter

<http://dx.doi.org/10.5772/intechopen.69587>

Abstract

Optical limiters are smart materials that follow passive approaches to provide laser protection, which are useful for the protection of human eyes, optical elements, and optical sensors from intense laser pulses. Many functional materials have been widely investigated with the view to realize practical passive optical limiting application. However, preparation of the required nonlinear optical active materials for optical limiters still presents a significant chemical challenge. In particular, this chapter gives emphasis to the nonlinear properties modulation of porphyrin and phthalocyanine covalently functionalized graphene and carbon nanotubes nano hybrids for the function of optical power limiting aiming the achievement of effective systems through the appropriate combination and modulation of several structural components. The nonlinear optical mechanisms observed in inorganic-organic nano hybrids, i.e., nonlinear scattering, nonlinear absorption, nonlinear refraction, and others, are discussed in conjunction with the influence of the materials properties and the laser source on the optical limiting performances.

Keywords: porphyrin, phthalocyanine, graphene, carbon nanotubes, optical limiting

1. Introduction

Nonlinear optics, which investigates the interaction of intense pulse field with materials, is a relatively promising field in photoelectronics and photonics with many fundamental scientific and technological potential [1–3]. Select the topic “nonlinear optics” in the ISI Web of Science and I found 44,486 papers in January, 2017 (**Figure 1**). This is because nonlinear optics impacts a wide range of technical fields, including X-rays, quantum optics,

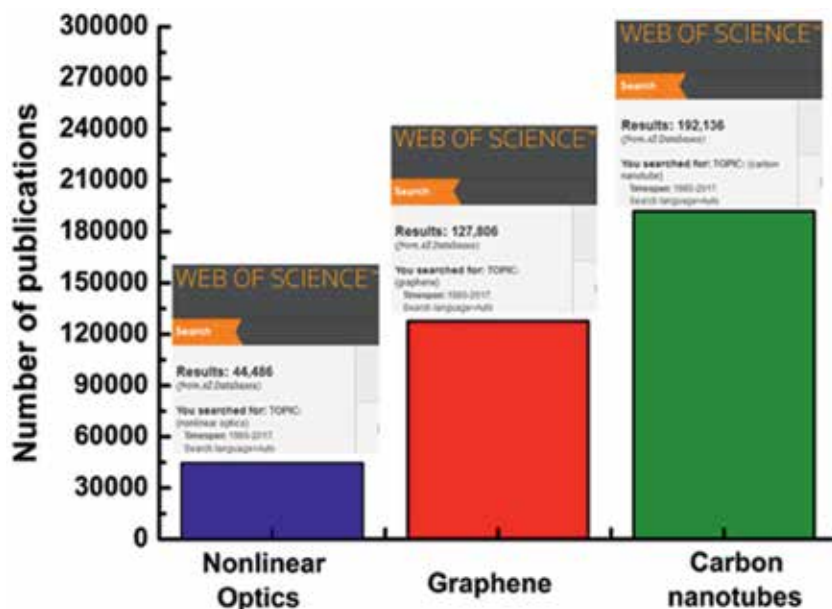


Figure 1. Publications statistics about nonlinear optics, graphene, and carbon nanotubes from Web of Science (Thomson-Reuters) database.

optical communications, fiber optics, ultrafast lasers, spectroscopy, photorefractivity, liquid crystals, polymers, semiconductors, organics, switching, ultraviolet, telecommunications, and signal processing [4, 5]. To further advance the performance of optical materials and devices, researchers have sought for lots of novel materials with improved nonlinear optical properties, including inorganic semiconductors, organic molecules, polymeric systems, and other nanomaterials [6, 7]. The latter, specifically, are of great interest because they present high nonlinear optical properties combined with versatility of available routes of synthesis, used to alter and optimize nanostructure to maximize nonlinear responses and other properties [8]. The rapid development of nanoscience and nanotechnology provides many unique opportunities for nonlinear optics. A growing number of nanomaterials, including graphene, carbon nanotubes, and their derivatives have been shown to possess remarkable nonlinear optical properties [9, 10], which promotes the design and fabrication of nanoscale optoelectronic and photonic materials. Materials that exhibit nonlinear optical performances are useful because they allow manipulation of the fundamental properties of laser light beams, and are hence of great technological importance in areas such as photonic switching, optical computing, and other optical data processing systems. It is thus of critical importance to explore innovative nonlinear optical materials required for the practical applications.

Basically, optical limiting, an important application of nonlinear optics, is useful for the protection of human eyes, optical elements, and optical sensors from intense laser pulses and is of great interest to the private industry and military [11]. As shown in **Figure 2**, ideal optical limiters have a linear transmittance at low input fluence, while above the threshold intensity the transmittance becomes constant. Over the past several decades, a huge pile of scientific reports

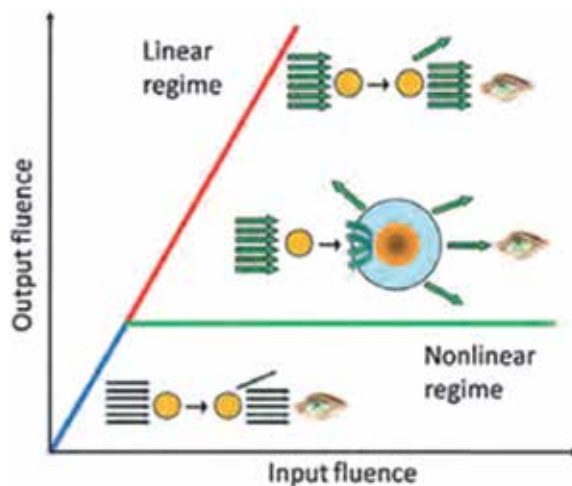


Figure 2. Trend of the light intensity (output fluence) transmitted by an ideal optical limiter versus the incoming light intensity (input fluence) [9].

has been published related to the study of these novel forms of carbon-based nanomaterials as highlighted in some prestigious reviews of graphene and carbon nanotubes with the view to realize practical passive optical limiting application [12–14]. The data about carbon nanomaterials have been swelled up so quickly that a single word of graphene and carbon nanotubes on web of science has resulted in thousands of publications statistics; the results are shown in **Figure 1**, which can help spur on the rapid development of carbon-based nanoscience. Porphyrins and phthalocyanines are attractive target materials for optical limiting applications due to the fact that they have a highly conjugated two-dimensional 18π -electron system resulting in a small HOMO-LUMO energy difference [15]. They also exhibit other additional advantages, i.e., exceptional stability, versatility, and processability features. The architectural flexibility of porphyrins and phthalocyanines can alter the electronic structure of the macrocyclic core, and thus, they allow the fine-tuning of the nonlinear optical performances [16]. Novel nonlinear optical materials may not be obtained from simple monomeric porphyrins or phthalocyanines, but be produced when strong electronic interactions between the highly delocalized π -electron systems and graphene/carbon nanotubes are induced by connecting them in a single system. Over times, the number of publications concerning the investigations and applications of porphyrins and phthalocyanines-functionalized graphene/carbon nanotubes has been an interesting observation. While phthalocyanine-functionalized graphene/carbon nanotubes have elicited wide interest in this area, porphyrins-functionalized graphene/carbon nanotubes have also increasingly attracted more attention (**Figure 3**). However, preparation of the required nonlinear optical active materials for optical limiters still presents a significant chemical challenge. Far from giving an exhaustive description of all the work that have been done in this area. This chapter will not explore application in detail, but only lay special stress on describing the recent achievements on the optical limiting properties of porphyrin and phthalocyanine covalently functionalized graphene/carbon nanotube nanohybrids. A great deal of information about nonlinear optics is now available on the ISI Web of Science.

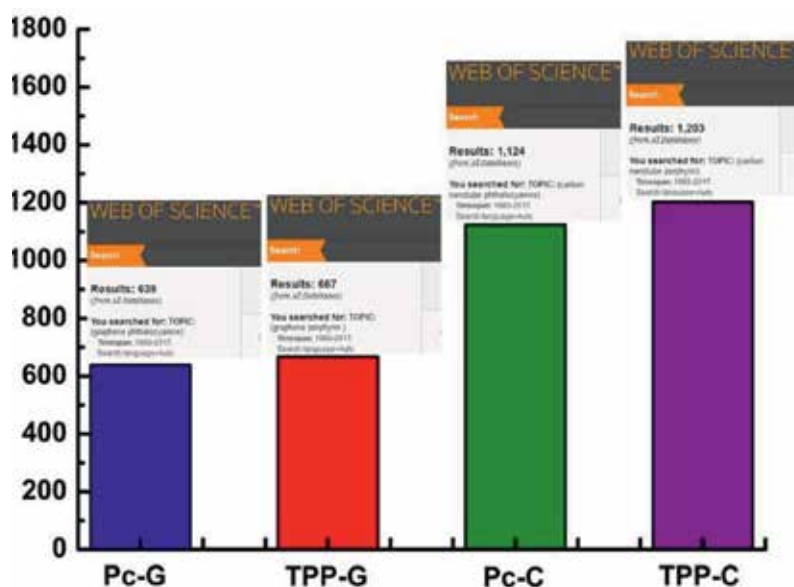


Figure 3. Publications statistics about phthalocyanine-functionalized graphene (Pc-G), porphyrin-functionalized graphene (TPP-G), phthalocyanine-functionalized carbon nanotubes (Pc-C), and porphyrin-functionalized carbon nanotubes (TPP-C) from Web of Science (Thomson-Reuters) database.

2. Experimental setup

With the aim to characterize the nonlinear optical absorption and optical limiting properties of a sample, the Z-scan technique, developed by Sheik-Bahae et al. [17, 18], can be used, which is widely used in optical nonlinearity, mainly due to the simplicity of the experimental setup and the easy interpretation of the results. The major advantage of this technique is that the magnitude and the sign of the nonlinearity can be provided simultaneously. The Z-scan is a nonlinear optical experiment in which the irradiance (or fluence) is continuously varied from the linear regime of the sample to an irradiance high enough to induce nonlinear effects and then back to the linear regime. Because of the light-induced lens-like effect, the sample has a tendency to recollimate or defocus the incident beam, depending on its z position with respect to the focal plane. This can be accomplished by translating the sample along the z -axis of a focused Gaussian beam, the results being shown in **Figure 4**. In order to avoid cumulative thermal effects, data were collected in single shot mode.

In the Z-scan experiment, a laser pulse is focused to a minimum waist at the focal point along the propagation direction (z -axis) of this pulse. By moving the sample along the z -axis, the input pulse intensity is varied in the sample. When the sample is placed at the focal point, nonlinear process can be observed because the pulse intensity is high. The pulse intensity within the sample is decreased when the sample is moved away from the focal point, producing no nonlinear process. The consecutive recording of the relative pulse intensity transmitted

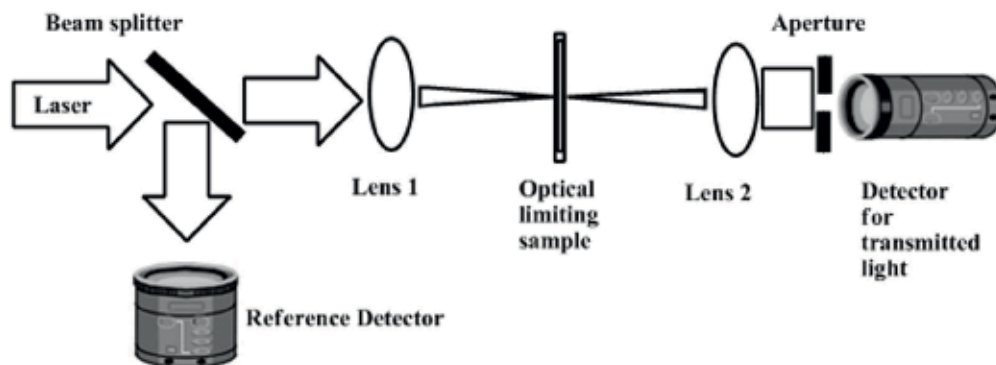


Figure 4. Experimental setup of the Z-scan technique with pulse trains, used to characterize the sample's nonlinear optical response [3].

through the samples as a function of the sample position along the axis provides important information about the imaginary part (the intensity-dependent absorption coefficient) and the real part (change in refractive index) of the third-order nonlinear susceptibility. Since the sample experiences different incident laser energy at each position as it moves along the z direction, any nonlinearity in transmission can be revealed by this measurement. The energy of the input (laser energy reaching the sample) and output (laser energy exiting the sample) laser pulses was monitored simultaneously by two energy detectors (Rjp-765 energy probe), which were linked to a computer by a general-purpose interface bus (GPIB) interface. To measure the nonlinear absorption of the samples, the Z -dependent transmittance was measured by using the open-aperture Z-scan method. In this technique, the aperture is absent, and so the total transmitted energy is detected, from which the nature of the absorptive optical nonlinearity can be determined alone. Division of the Z-scan curve obtained with an aperture by that without an aperture gives a curve with nonlinear absorption effectively eliminated and affords the nonlinear refraction response. The optical limiting measurements were performed when the sample was located at focal point by varying the input energy and recording the output energy. Both the incident and the transmitted energies were measured simultaneously by two pyroelectric detectors with Laser Probe Rjp-765 Energy Ratio meter.

3. Porphyrin and phthalocyanine covalently functionalized graphene and carbon nanotubes nanohybrids for optical limiting

3.1. Porphyrin and phthalocyanine covalently functionalized graphene

Graphene is the name given to a two-dimensional (2D) sheet of sp^2 -hybridized carbon packed in a hexagonal lattice, with a carbon-carbon distance of 0.142 nm. Long-range π -conjugation in graphene yields extraordinary thermal, physical, chemical, mechanical, and electrical properties, such as ultrafast carrier dynamics, superlative mechanical strength, large specific surface area, and high electrical and thermal conductivity, among others [19]. Thanks to these

extraordinary and superior properties, graphene has long been the interest of many theoretical studies and more recently became an exciting area for experimentalists with many commercial applications, including gas and energy storage, as well as micro- and optoelectronics [20]. Despite the great application potential, it is worth mentioning that pristine graphene has no appreciable solubility in most solvents. However, the solubility and processability are the primary problems for many prospective applications of graphene-based materials. To improve the dispersibility of graphene in common organic solvents and change its photophysical properties, a variety of methods for the graphene surface modification have been developed [19]. These graphene-based nanohybrids with different forms have different nonlinear optical properties and photophysical processes. In most cases, when organic molecules are covalently attached on the graphene surface, its extended aromatic character is perturbed, providing the opportunities to control its optoelectronic properties. Indeed, it is expected that the combination of graphene and optoelectronically active porphyrin and phthalocyanine molecules would afford species that possess not only the intrinsic properties of porphyrin and phthalocyanine but also some functions arising from the mutual π interaction between graphene and porphyrin/phthalocyanine; multifunctional nanometer-scale materials with enhanced optical limiting responses compared with that of the individual components may thereby be generated. The nonlinear optical properties of graphene-based materials have been extensively investigated, and this area has been reviewed [5, 8, 9, 13, 16]. The discussion here will be limited to selected highlights of our studies and more recent developments.

The electronic structure of porphyrin and phthalocyanine molecules can be tailored by altering the peripheral and axial functionalities or by either metal substitution at the central binding site, thus affording great versatility in controlling their optoelectronic properties [21–23]. For the nonlinear optical and optical limiting applications, Xu et al. designed and synthesized a novel soluble graphene nanohybrid material (TPP-NHCO-SPFGraphene) covalently functionalized with metal-free porphyrin (TPP-NH₂) via an amidation reaction [24]. Attachment of the metal-free porphyrin TPP-NH₂ improves the solubility and dispersion stability of the TPP-NHCO-SPFGraphene nanohybrids in organic solvents. For the donor-acceptor nanohybrids, the fluorescence of the metal free porphyrin TPP-NH₂ was effectively quenched due to a possible electron transfer process. The effective intramolecular energy quenching may also be facilitated by a through-bond mechanism, originating from the direct linkage mode of the two moieties by the amide bond. A superior optical limiting performance, better than the benchmark material C₆₀, the control samples, and the individual components (TPP-NH₂ and graphene oxide (GO)), is observed. Similarly, the preparation and nonlinear optical properties of two novel graphene nanohybrid materials covalently functionalized with porphyrin and C₆₀ were reported by Tian et al. [25]. The results displayed that covalently functionalizing graphene with porphyrin and C₆₀ can improve the nonlinear optical performance in the nanosecond regime (**Figure 5**).

Very recently, porphyrin-reduced graphene oxide (RGO-TPP) nanohybrids with a push-pull motif have been satisfactorily prepared by our group following the Prato protocol, via a 1,3-dipolar cycloaddition reaction of appropriate formyl derivatives with sarcosine [26]. Stepwise and “one-pot” procedures have been explored (**Scheme 1**): A straightforward Prato reaction (i.e., a 1,3-dipolar cycloaddition) with sarcosine and a formyl-containing porphyrin, and a stepwise

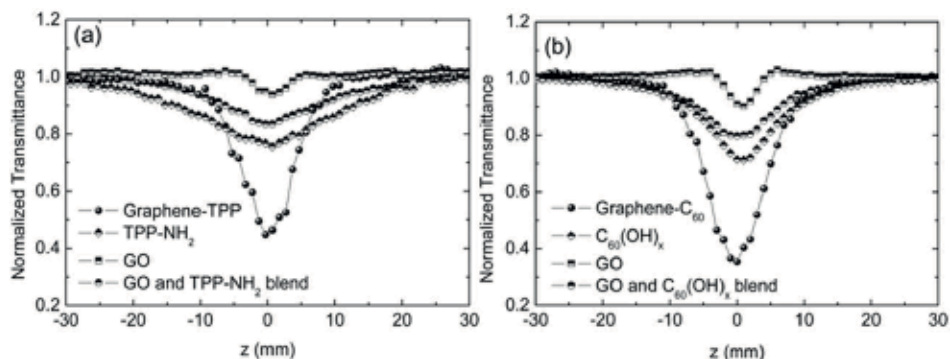
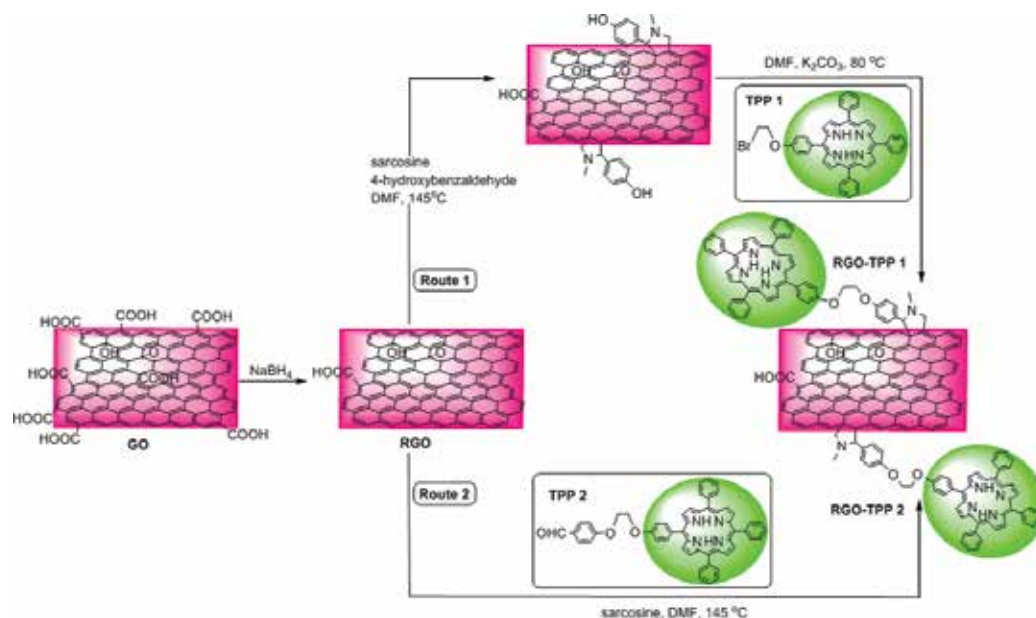


Figure 5. Open-aperture Z-scan curves of (a) Graphene-TPP, TPP-NH₂, GO, and GO and TPP-NH₂ blend, and (b) Graphene-C₆₀, C₆₀(OH)_x, GO, and GO and blend C₆₀(OH)_x [25].

method that involves a 1,3-dipolar cycloaddition to the RGO surface using 4-hydroxybenzaldehyde, followed by nucleophilic substitution with an appropriate porphyrin. The interaction between RGO and the porphyrins was followed by fluorescence spectroscopy, and significant fluorescence quenching was observed for both nanohybrids, indicating the presence of efficient electron/energy transfer. When compared to RGO and porphyrins (TPP 1 and TPP 2), both nanohybrids display better nonlinear optical performances (**Figure 6**), implying a synergistic effect between two components due to the covalent linkage. Effective combination of the



Scheme 1. Chemical routes to functionalize RGO with porphyrin molecules: preparation of RGO-TPP 1 (Route 1) and RGO-TPP 2 (Route 2) [26].

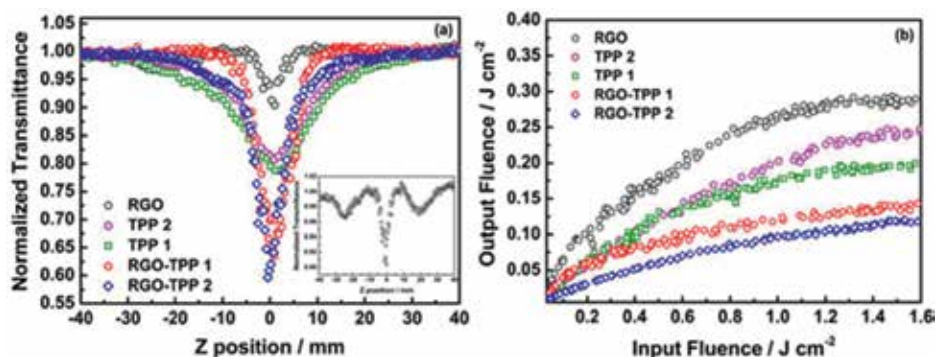


Figure 6. (a) Open-aperture Z-scan curves and (b) Optical limiting performances of RGO, TPP 2, TPP 1, RGO-TPP 1, and RGO-TPP 2 [26].

different nonlinear optical mechanisms, i.e., reverse saturable absorption, saturable absorption, excited absorption, nonlinear scattering, and photo-induced energy/electron transfer in the RGO-TPP nanohybrids leads to the improved nonlinear optical (including optical limiting) performances for 4 ns pulses at 532 nm. In the nanohybrid system, the nonlinear scattering originating from the graphene moieties can largely enhance the damage threshold of the nanohybrids. The similar accumulation effect leading to an increased nonlinear optical performance was also confirmed in RGO-TPP nanohybrid systems prepared by two synthetic routes that involve functionalization of the RGO by means of diazonium chemistry [27].

“Axial-bonding” at porphyrins may provide an approach for the preparation of arrays with tunable photoelectronic properties by changing the π -orbital interactions [28]. Axial substituents in porphyrins can favorably influence the nonlinear optical properties due to the presence of a dipole moment that is perpendicular to the macrocycle in the axially functionalized porphyrins. SnTPP and phosphorus-cored porphyrin (PTPP) (**Figure 7**) are well-known axial-bonding building blocks, the Sn-OH and P-Cl bonds being reactive toward carboxylates and aryloxides, respectively. By using the reactive activity of hydroxyl and carboxyl groups on the basal planes of GO, as shown in **Figure 7**, Wang et al. synthesized two novel graphene nanohybrids incorporating axially functionalized porphyrins (GO-PTPP and GO-SnTPP) [29]. Their nonlinear optical properties and optical limiting performance have been studied by using the Z-scan technique at 532 nm with 4 ns and 21 ps laser pulses. Both nanohybrids exhibited enhanced nonlinear optical and optical limiting properties in comparison to the individual GO and porphyrins in both the nanosecond and picosecond regimes, due to an effective combination of different nonlinear optical mechanisms, i.e., nonlinear scattering and/or two-photon absorption with reverse saturable absorption, and photo-induced electron or energy transfer from the electron-donor porphyrin moiety to the acceptor graphene.

Very recently, in order to optimize the RGO dispersion and enhance interfacial bonding, we reported two covalent functionalization approaches for the fabrication of RGO-TPP nanohybrid materials (**Scheme 2**) [30]. These are based on the initial covalent introduction of phenol groups onto the RGO surfaces by 1,3-dipolar cycloaddition or a diazotization reaction, and subsequent nucleophilic substitution at dichloro(5,10,15,20-tetraphenylporphyrinato)tin(IV) (SnTPP). The

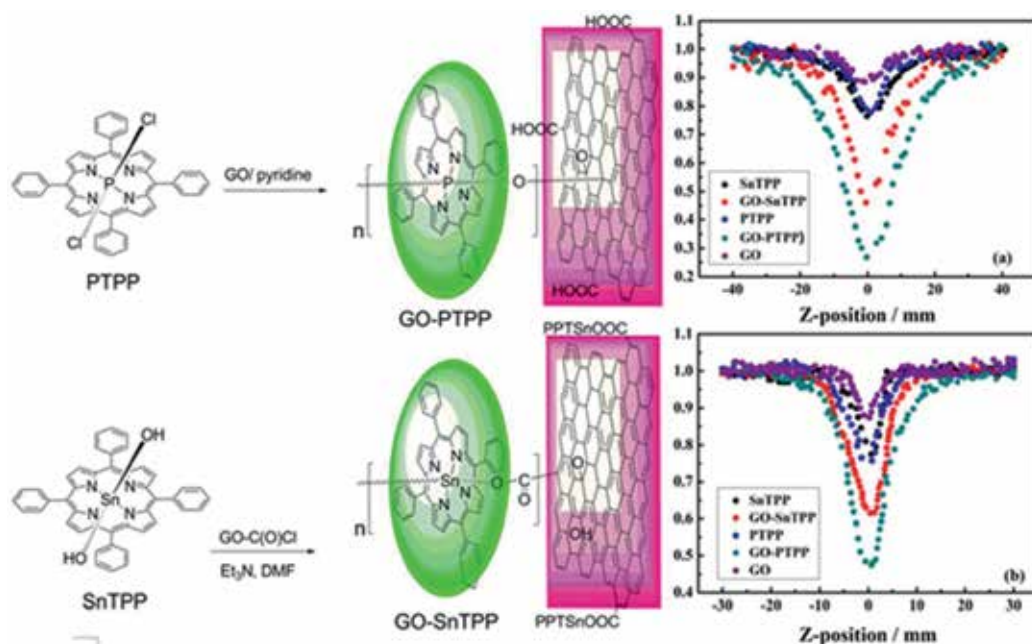
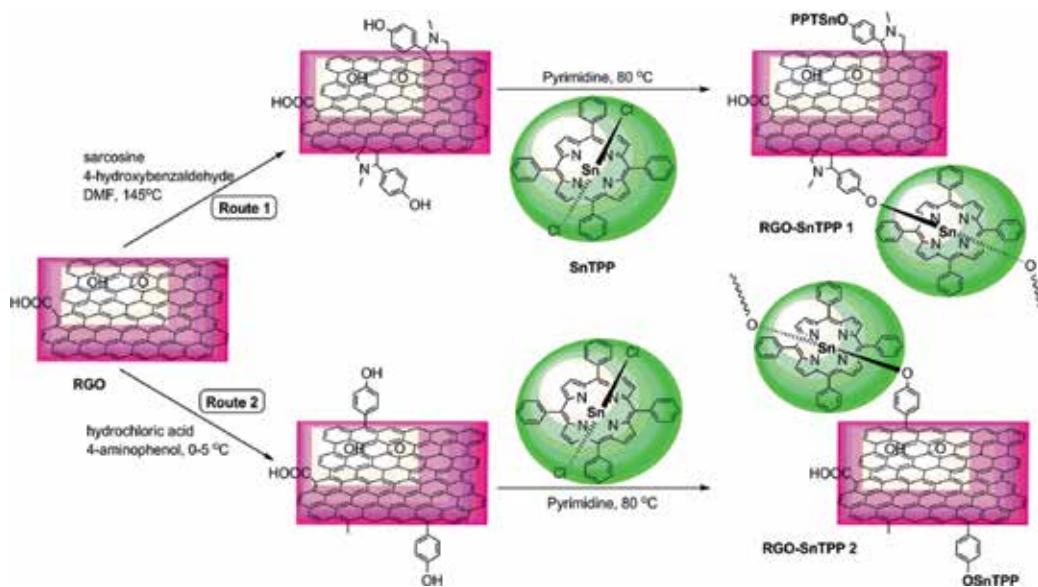


Figure 7. Synthetic routes of GO-PTPP and GO-SnTPP, and open-aperture Z-scan curves of GO, SnTPP, GO-SnTPP, PTPP, and GO-PTPP at 532 nm with (a) 4 ns and (b) 21 ps pulse duration [29].



Scheme 2. Syntheses of RGO-SnTPP 1 and RGO-SnTPP 2 [30].

porphyrin-functionalized RGO nano hybrids exhibited superior nonlinear optical performance to a RGO suspension at 532 nm under both picosecond and nanosecond regimes (**Figure 8**), due to a combination of mechanisms, while significant differences in their nonlinear optical

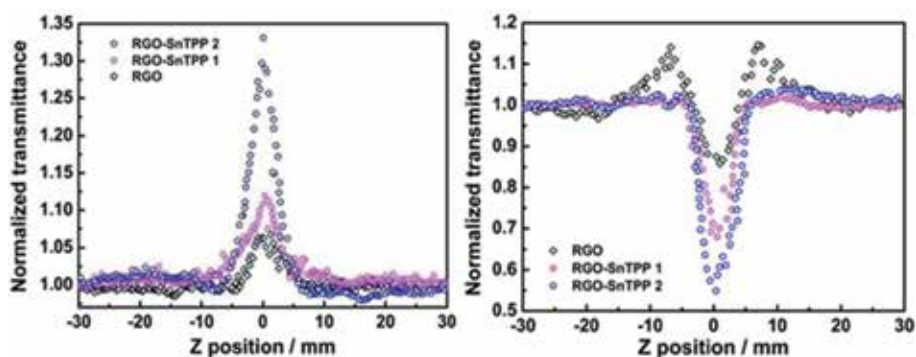


Figure 8. Left: Open-aperture Z-scan traces of RGO, RGO-SnTPP 1, and RGO-SnTPP 2 in dimethylsulfoxide (DMSO), obtained under 21 ps, 532 nm laser excitation. Right: Open-aperture Z-scan traces of RGO, RGO-SnTPP 1, and RGO-SnTPP 2 in DMSO, obtained under 4 ns, 532 nm laser excitation [30].

responses were observed, highlighting the influence on photophysical properties of the degree of functionalization and the synthetic approach employed. We also found that the two-photon absorption coefficients β_2 values increase on proceeding from the components RGO and SnTPP to the nanohybrids, and that the β_2 values of the nanohybrids under ns conditions differ significantly from that of the RGO/SnTPP blend, though being mindful of the errors associated with these measurements. Photo-induced electron or energy transfer mechanisms play an important role in the superior optical limiting performance. While nonlinear scattering dominates the optical limiting response, the photo-induced electron or energy transfer facilitates the deactivation of the nanohybrids, leading to energy dissipation via the nonradiative decay and thus, the effective heat accumulation in the nanohybrids or heat transfer from RGO to the adjacent solvent.

As porphyrin analogs, the structurally similar and biologically phthalocyanine are also effective optical limiters. Zhu et al. reported the synthesis and optical limiting performances of a soluble GO covalently functionalized with zinc phthalocyanine (GO-PcZn) by an amidation reaction [31]. A superior nonlinear optical effect and broadband optical limiting performance, better than GO and PcZn, are observed for GO-PcZn at both 532 and 1064 nm, suggesting a remarkable accumulation effect as a result of the covalent link between GO and PcZn. Similarly, a soluble GO axially substituted gallium phthalocyanine nanohybrid material (GO-PcGa) was prepared and designed by Li et al. [32]. At the same level of concentration of 0.1 g/L, this material displays much better optical limiting than the other three samples (GO, PcGa, and the benchmark optical limiting material C_{60}) at both 532 and 1064 nm. The improved optical limiting performance was assigned to the effective combination of the different optical limiting mechanisms, i.e., reverse saturable absorption in PcGa, and nonlinear scattering and two-photon absorption in GO. For PcGa and C_{60} , only reverse saturable absorption dominates at 532 nm, and no obvious nonlinear scattering was observed. Although the origin of the enhancement of the optical limiting effect for GO-PcGa at 1064 nm is not clear yet, the PcGa should certainly play an important but unknown role in this system due to the fact that GO-PcGa possesses much better broadband nonlinear optical and optical limiting performances than GO and PcGa alone.

Song et al. demonstrated the surface functionalization of RGO with zinc phthalocyanine (ZnPc), based on the initial covalent linkage of ZnPc to GO and subsequent *in situ* reduction of GO moiety to RGO during mild thermal treatment in dimethylformamide solvent [33]. The results display that the new nanohybrids allow the formation of stable colloidal solutions in various polar solvents such as dimethylsulfoxide, increasing the manipulation and processing of RGO. The nonlinear optical properties of the RGO-ZnPc nanohybrid were investigated by using the Z-scan technique. At a concentration of 0.13 mg/L, the RGO-ZnPc nanohybrid showed much larger nonlinear absorption coefficient β and better optical limiting performance than those of individual GO, ZnPc, and GP-ZnPc nanohybrids, ascribed to a combination of two-photon absorption resulting from the sp^3 domains, saturable absorption from the sp^2 carbon clusters, and excited state absorption from numerous localized sp^2 configurations in RGO moiety, reverse saturable absorption resulting from ZnPc moiety, and the contribution of improved photo-induced electron/energy transfer from ZnPc to RGO. Indeed, an improved photo-induced electron/energy transfer process with more efficient fluorescence quenching and energy release is observed in RGO-ZnPc than that of GO-ZnPc. In addition, the effect of peripheral substituents attached to phthalocyanines on the third-order nonlinear optical properties of graphene oxide-zinc(II) phthalocyanine hybrids, and the effects of central metals on the photophysical and nonlinear optical properties of reduced graphene oxide-metal(II) phthalocyanine hybrids were also reported [34, 35].

3.2. Porphyrin and phthalocyanine covalently functionalized carbon nanotubes

Carbon nanotubes (CNTs) are structures from the fullerene family consisting of a honeycomb nanosheet of sp^2 bonded carbon atoms rolled seamlessly into itself to form a cylinder. Typically, CNTs are divided into two distinct types, both with high structural perfection: single-walled carbon nanotubes (SWCNTs) that are made from one graphene sheet rolled as a tube and multiwalled carbon nanotubes (MWCNTs) that are obtained when several stacked graphitic shells are built to give concentric cylinders or graphene sheets are rolled [36]. CNTs have attractive mechanical, electrical, and thermal properties, which have found many potential applications in the field of nanoscience and nanotechnology. CNTs exhibit remarkable optical limiting properties on intense laser beams with ultrafast recovery time and broad bandwidth operation [37]. The advantage of CNTs-based nanomaterials manifests themselves in tailorable chemical properties by combining functional materials. Most importantly, the one-dimensional nanostructure of CNTs acts a favorable host for functional materials, forming versatile optical limiting nanocomposites [38]. It is therefore that CNTs are becoming a key component toward the development of nonlinear photonic devices. However, a CNTs system alone is not sufficient to fulfill all of the specifications of optical limiting. Indeed, various systems need to be coupled to extend the spectral and temporal ranges of effective optical limiting.

A CNT possesses one of the most extensive delocalized π -electron systems, which has been observed to be effective in optical limiting material and extends outside the range of many other optical limiting materials [39]. Covalently functionalized CNTs with porphyrins naturally pursued. For instance, Liu et al. reported the preparation and optical limiting

performances of three covalently functionalized SWCNTs with porphyrins [40]. The optical limiting properties were determined by Z-scan experiments with linearly polarized 5 ns pulses at 532 nm generated from a frequency doubled Q-switched Nd:YAG laser. The structures of the porphyrin-functionalized SWCNTs are illustrated in **Figure 9**. The optical limiting performances of the three SWCNTs-based nanohybrids are better than not only the individual porphyrins, SWCNTs, and C_{60} but also the blended system of SWCNTs and porphyrins. The optical limiting thresholds approximately 70, 100, and 150 mJ/cm^2 were determined for I, II, and III, respectively, all of which are much smaller than those of C_{60} (300 mJ/cm^2) and SWCNTs (250 mJ/cm^2).

Recently, Liu et al. reported the preparation of tetraphenylporphyrin covalently functionalized MWCNTs (MWCNT-TPP) with diameter ranges of <10, 10–30, and 40–60 nm by the reaction of MWCNTs with *in situ* generated porphyrin diazonium compounds (**Scheme 3**) [41]. A considerable quenching of the fluorescence intensity was found in the photoluminescence spectrum due to the fact that the unique direct linkage mode facilitates the effective photo-induced electron transfer between the excited porphyrin moiety and the extended π -system of MWCNTs. As laser pulse width increased from 5.6 to 11.7 ns, an obvious enhancement in the optical nonlinearities of MWCNT-TPP nanohybrid materials was observed (**Figure 10**), due to the improved efficiency of photo-induced electron transfer from porphyrin to MWCNTs with the increasing of pulse width.

Nanohybrids MWCNT-TPP and MWCNT-AIBN were prepared by radical polymerization (**Scheme 4**) [42]. The open-aperture Z-scan technique at 532 nm with 4 ns laser pulses was used to investigate the optical limiting performances; the results suggested that these nanohybrids exhibited generically good nonlinear optical properties. Comparison between the optical limiting performances of nanohybrids MWCNT-TPP and MWCNT-AIBN and that of TPP, MWCNTs, and mixture of both was effectuated. All samples displayed that the output fluence increased linearly with increasing input fluence at low laser pulse and deviations from linearity with further increase in input fluence pointed to the occurrence of optical limiting response. The order of the decreases in output fluence was MWCNT-TPP > TPP > MWCNT-AIBN > MWCNTs, implying that the optical limiting effect of MWCNT-TPP was superior to that of the MWCNT-AIBN and to that of the individual porphyrin as well as MWCNTs. As shown in **Figure 11**, at the wavelength used, the mechanism of

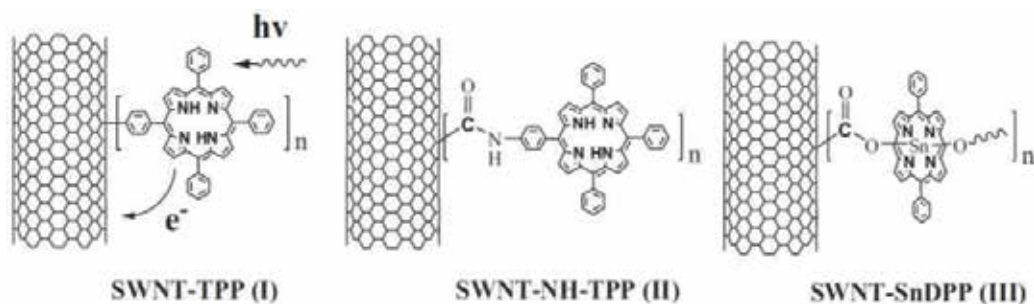
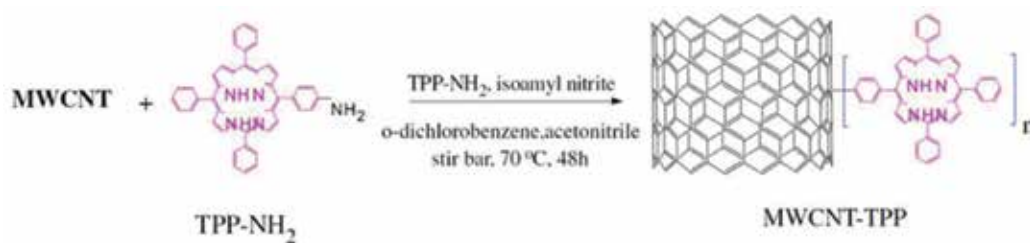


Figure 9. Structures of porphyrins covalently functionalized SWCNTs I, II, and III [40].



MWCNT-TPP(I), $d < 10\text{nm}$; (II), $d = 10\text{--}30\text{nm}$; (III), $d = 40\text{--}60\text{nm}$.

Scheme 3. Synthetic routes of MWCNT-TPP [41].

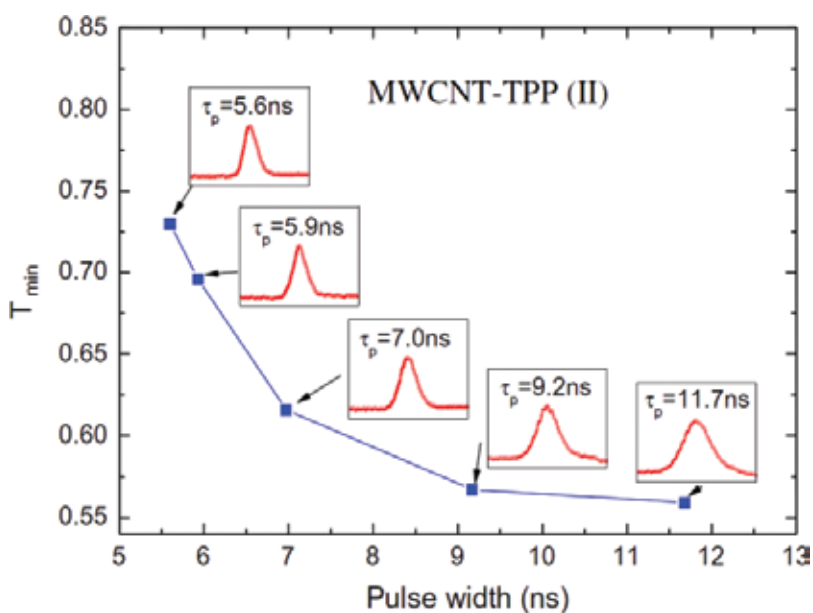
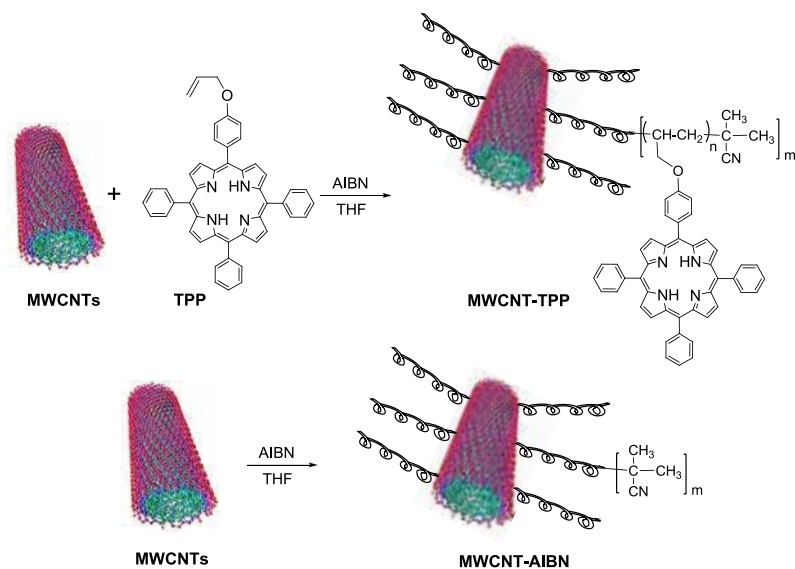


Figure 10. Transmittance valleys (T_{\min}) of Z-scan curves of MWCNT-TPP (II) with different pulse width of 5.6, 5.9, 7.0, 9.2, and 11.7 ns [41].

increased optical limiting may be ascribed to reverse saturable absorption, nonlinear scattering, and photo-induced electron/energy transfer between the MWCNTs and the porphyrin moieties. The covalent attachment of porphyrins onto the surfaces of MWCNTs is expected to facilitate the fabrication of devices requiring the use of CNTs in optical limiting applications.

Two porphyrin covalently functionalized MWCNTs nanohybrids, MWCNT-ZnTPP and MWCNT-TPP, have been prepared directly from pristine MWCNTs through 1,3-dipolar cycloaddition reactions (**Scheme 5**), and the respective optical limiting properties of the materials were compared to those of zinc and free-base meso-tetraphenylporphyrins (ZnTPP and TPP) [43]. The nanohybrids displayed improved optical limiting ability. At the highest



Scheme 4. Synthetic routes of MWCNT-TPP and MWCNT-AIBN [42].

input fluence used in the experiments (1.65 J/cm^2), the output fluences were determined to be 0.90, 0.83, 0.75, 0.40, and 0.27 J/cm^2 for TPP, ZnTPP, MWCNTs, MWCNT-ZnTPP, and MWCNT-TPP, respectively. This clearly suggested that MWCNT-ZnTPP and MWCNT-TPP possessed the best optical limiting effect. In addition, the closed-aperture Z-scan measurements were also performed at 532 nm with both nanosecond and picosecond pulses for TPP, ZnTPP, MWCNT-TPP, and MWCNT-ZnTPP. As shown in **Figure 12**, all samples exhibit a self-defocusing effect, corresponding to a negative nonlinearity as revealed by the peak-valley signature, and the differences between the normalized transmittance values and

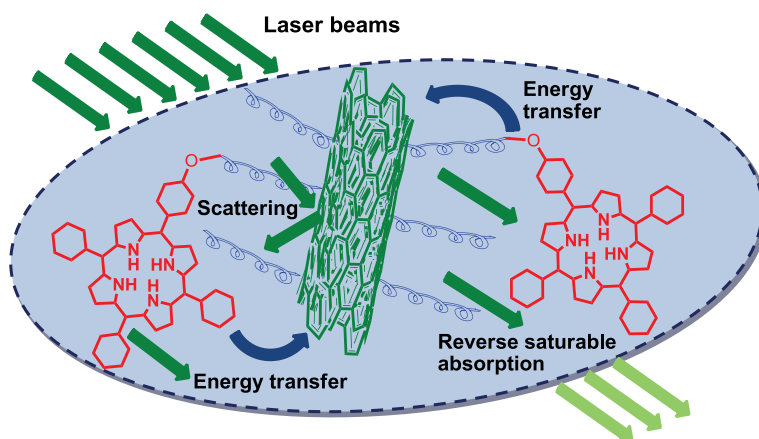
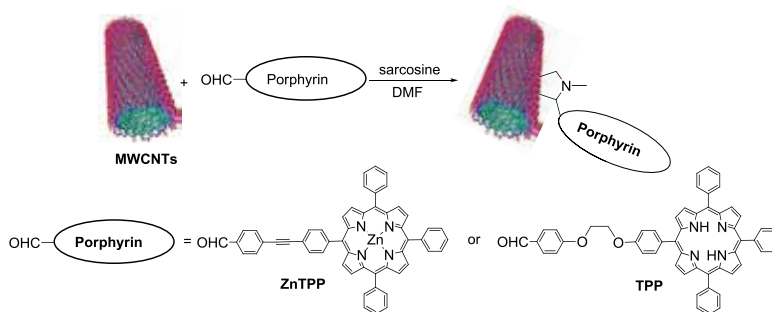


Figure 11. Possible mechanisms for the enhanced optical limiting effect of MWCNT-TPP [42].



Scheme 5. Preparation of MWCNT-ZnTPP and MWCNT-TPP hybrid materials through a 1,3-dipolar cycloaddition reaction [43].

valley positions for MWCNT-TPP and MWCNT-ZnTPP are larger than those for the other compounds in this study. This clearly indicated that the porphyrin-functionalized MWCNT nanohybrids possess larger nonlinear refraction coefficients than the individual components, presumably originating from their covalent linkage.

Wang et al. synthesized axially coordinated metal-porphyrin-functionalized multiwalled carbon nanotubes nanohybrids via two different synthetic approaches (**Scheme 6**, a one-pot 1,3-dipolar cycloaddition reaction and a stepwise approach that involved 1,3-dipolar cycloaddition followed by nucleophilic substitution) [44], namely MWCNT-SnTPP 1 and MWCNT-SnTPP 2. The attachment of the tin porphyrin as an electron-donor onto the surface of the MWCNTs resulted in an increased electron absorption than its parent compound in the whole spectral region and an efficient fluorescence quenching. The resultant materials exhibit significant reverse saturable absorption or saturable absorption when nanosecond or picosecond pulses, respectively, are employed. A combination of the outstanding properties of MWCNTs and the chemically attached metal-porphyrins should be responsible for the improvement in the nanosecond

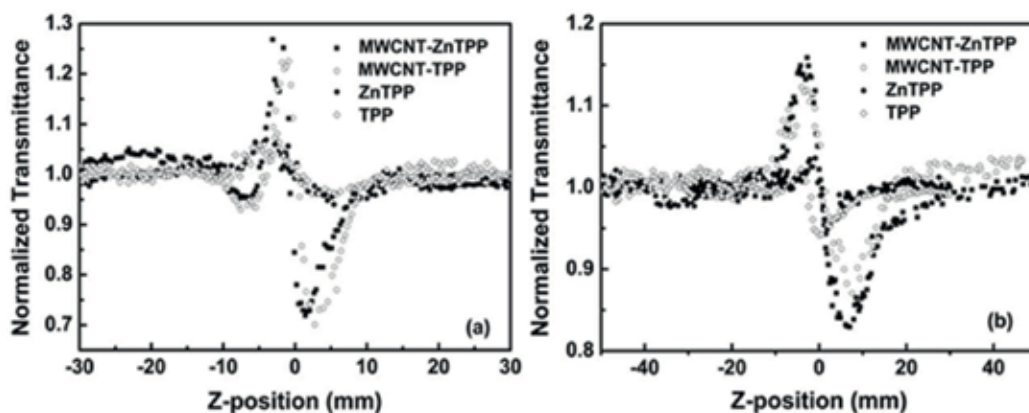
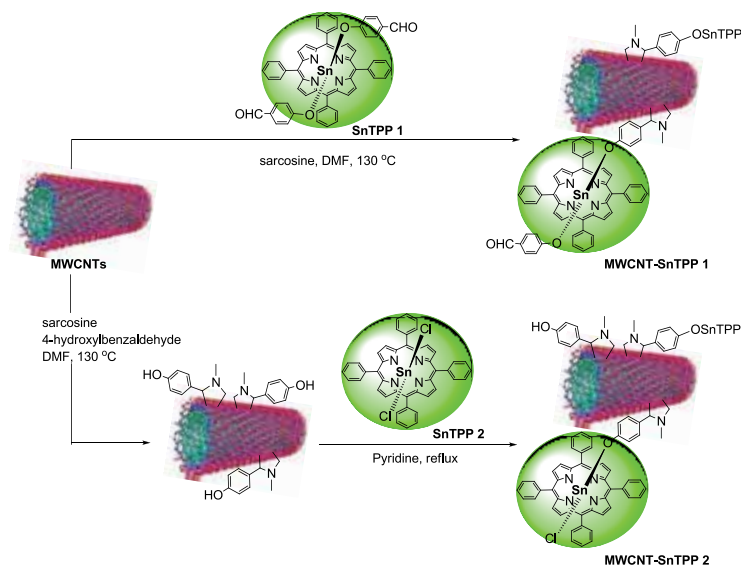


Figure 12. Normalized closed-aperture Z-scan curves of TPP, ZnTPP, MWCNT-TPP, and MWCNT-ZnTPP in *N,N*-dimethylformamide (DMF) with (a) 4 ns and (b) 21 ps pulse durations [43].



Scheme 6. Preparation of MWCNT-SnTPP 1 and MWCNT-SnTPP 2 [44].

regime nonlinear absorption. It is well-known that nonlinear absorption performance is strongly affected by the pulse width. Indeed, the behaviors of MWCNT-SnTPP 1 and MWCNT-SnTPP 2 were quite different at the ns and ps time scales. Both nanohybrids exhibit saturable absorption performance in the ps regime, while reverse saturable absorption was observed in the ns regime. This change was ascribed to the result of transitions from the first excited state to higher excited states arising from the temporally longer pulse width under ns conditions.

CNTs in combination with Pcs were also investigated as optical limiting materials. Several reports appeared on the preparation and nonlinear optical properties of covalently functionalized CNTs with Pcs. For instance, the nonlinear optical properties of a novel unsymmetrically substituted metal-free phthalocyanine covalently functionalized MWCNTs nanohybrid (PcH₂-MWCNTs) were investigated by using the Z-scan technique at 532 nm in the ns time scale [45]. Strong nonlinear scattering was observed for this material at higher intensities, which evidently comes from the MWCNTs moiety. However, no obvious nonlinear scattering was observed from the pristine PcH₂ solution, indicating that the optical limiting effect totally originates from reverse saturable absorption. The nonlinear optical response of PcH₂ is ascribed to reverse saturable absorption, while that of PcH₂-MWCNTs is due to both reverse saturable absorption and nonlinear scattering. Both nonlinear mechanisms may be conflicting for optical limiting, suppressing the whole nonlinear response of PcH₂-MWCNTs. However, an improved nonlinear absorption was observed for indium phthalocyanine-SWCNTs composite in DMSO, when compared to the nonlinked phthalocyanine counterpart [46]. The optical properties of this composite were found to display high sensitivity toward the change of solvent matrix. Due to quenching by the counterionic DMF species, the triplet quantum yield values of the materials in DMF were found to be lower than those of their values in DMSO. In other words, solvents that can generate resonance-stabilized counterions as shown for DMF may tend to lower the inherent optical limiting effect of materials. However, the longest-lived triplet lifetimes with a

highest triplet quantum yield was observed for the nanocomposite in DMSO, and thus the best optical limiting properties can be expected when compared to the other systems investigated.

4. Summary and outlook

Many functional materials have been widely investigated with the view to realize practical passive optical limiting application. However, preparation of the required nonlinear optical active materials for optical limiters still presents a significant chemical challenge. As we mentioned above, the excellent chemical activity of graphene and CNTs provides a broad platform for various functional counterparts, forming multi-component, multifunctional hybrid composites with wider spatial and temporal responses for optical limiting, which are suitable candidates to satisfy the requirements for the next generation of photonic components. The porphyrins and phthalocyanines covalently functionalized graphene and carbon nanotubes nanohybrids described in this work are the product of recent efforts spent in designing effective nanomaterial structures for optical limiting applications. The nanohybrids exhibited a strong optical limiting behavior, and the incorporation of porphyrins and phthalocyanines significantly increased the nonlinear optical performances of graphene and CNTs. The nonlinear optical mechanisms observed in inorganic-organic nanohybrids, i.e., nonlinear scattering, nonlinear absorption, nonlinear refraction, and others, are discussed in conjunction with the influence of the materials properties and the laser source on the optical limiting performances.

Generally speaking, covalent functionalization of graphene and CNTs materials results in better optical limiting effect than noncovalent functionalization. This is because the covalent link can more effectively improve photo-induced energy or electron transfer from the functional moiety to the graphene and CNTs. In most of such nanohybrids, it is being attached importance to the photo-induced energy or electron transfer from functional moieties to graphene or CNTs, which is considered playing an important role on improving optical limiting performance. However, the data are very fragmentary, a detailed understanding of the factors affecting the nonlinear response is still necessary, and further work should be devoted to this objective. Multifunctional optical limiters are expected to have broad application range for various laser sources. The plasticity and flexibility of graphene and CNTs allow one to design and fabricate a range of structures to meet different demands. Graphene- and CNTs-based nanomaterials are still in their infancy, current demonstrations only show modest results, and while the very high third-order susceptibility combined with the fast optical response is promising, significant developments will need to be made before optical limiting by graphene- and CNTs-based nanomaterials can become a reality in a realistic commercial application. Looking toward the future use of graphene- and CNTs-based nanomaterials, it may be that in expanding on the already studied synthetic procedures lies a key to unlock a realm of opportunities for these materials. From a practical application of view, many efforts have been currently invested into the research of graphene- and CNTs-based nanocomposites in an attempt to allow for the fabrication of solid-state films or embedded solid-state thin films, which is very significant but challenging, and will undoubtedly open a way to design and fabricate the industrially applicable optical limiters.

Acknowledgements

This research was supported financially by the National Natural Science Foundation of China (51506077, 51602130), the Natural Science Foundation of Jiangsu Province (BK20150488), the Natural Science Foundation of Jiangsu High School (15KJB430007, 15KJB610003), the China Postdoctoral Foundation (2016M601733), and Research Foundation of Jiangsu University (13JDG066, 15JDG156).

Author details

Aijian Wang^{1*} and Wei Zhao²

*Address all correspondence to: wajajs@ujs.edu.cn

1 School of Chemistry and Chemical Engineering, Jiangsu University, Zhenjiang, PR China

2 School of Energy and Power Engineering, Jiangsu University, Zhenjiang, PR China

References

- [1] Perry JW, Mansour K, Lee IYS, Wu XL. Organic optical limiter with a strong nonlinear absorptive response. *Science*. 1996;**273**:1533-1536
- [2] He GS, Yong KT, Zheng QD, Sahoo Y, Baev A, Rysanyanskiy AI, Prasad PN. Multi-photon excitation properties of CdSe quantum dots solutions and optical limiting behavior in infrared range. *Optics Express*. 2007;**15**:12818-12833
- [3] Calvete M, Yang GY, Hanack M. Porphyrins and phthalocyanines as materials for optical limiting. *Synthetic Metals*. 2004;**141**:231-243
- [4] Shirk JS, Pong RFS, Flom SR, Heckmann H, Hanack M. Effect of axial substitution on the optical limiting properties of indium phthalocyanines. *The Journal of Physical Chemistry A*. 2000;**104**:1438-1449
- [5] Liu ZB, Zhang XL, Yan XQ, Chen YS, Tian JG. Nonlinear optical properties of graphene-based materials. *Chinese Science Bulletin*. 2012;**57**:2971-2982
- [6] Leonardo DB, Daniel SC, Cleber RM. Nonlinear optical absorption of organic molecules for applications in optical devices. In: Costa N, Cartaxo A, editors. *Advances in Lasers and Electro Optics*. Croatia: InTech; 2010. pp. 33-58
- [7] Zhao W, Wang Y, Wang AJ, Qian J, Zhu WH, Dou SP, Wang Q, Zhong Q, Chen AH. Novel Bi₂O₂CO₃/polypyrrole/g-C₃N₄ nanocomposites with efficient photocatalytic and nonlinear optical properties. *RSC Advances*. 2017;**7**:7658-7670
- [8] Wang J, Blau WJ. Inorganic and hybrid nanostructures for optical limiting. *Journal of Optics A: Pure and Applied Optics*. 2009;**11**:024001

- [9] Wang J, Chen Y, Li RH, Dong HX, Zhang L, Lotya M, Coleman JN, Blau WJ. Nonlinear optical properties of graphene and carbon nanotube composites. In: Yellampalli S, editors. *Carbon Nanotubes - Synthesis, Characterization, Applications*. Croatia: InTech; 2011. pp. 397-424
- [10] Martinez A, Yamashita S. Carbon nanotube-based photonic devices: Applications in nonlinear optics. In: Marulanda JM, editors. *Carbon Nanotubes Applications on Electron Devices*. Croatia: InTech; 2011. pp. 367-386
- [11] Tutt LW, Boggess TF. A review of optical limiting mechanisms and devices using organics, fullerenes, semiconductors and other materials. *Progress in Quantum Electronics*. 1993;**17**:299-338
- [12] Wang J, Chen Y, Blau WJ. Carbon nanotubes and nanotube composites for nonlinear optical devices. *Journal of Materials Chemistry*. 2009;**19**:7425-7443
- [13] Chen Y, Bai T, Dong NN, Fan F, Zhang SF, Zhuang XD, Sun J, Zhang B, Zhang XY, Wang J, Blau WJ. Graphene and its derivatives for laser protection. *Progress in Materials Science*. 2016;**84**:118-157
- [14] Dini D, Calvete MJF, Hanack M. Nonlinear optical materials for the smart filtering of optical radiation. *Chemical Reviews*. 2016;**116**:13043-13233
- [15] Senge MO, Fazekas M, Notaras EGA, Blau WJ, Zawadzka M, Locos OB, Mhuircheartaigh EMN. Nonlinear optical properties of porphyrins. *Advanced Materials*. 2007;**19**:2737-2774
- [16] De la Torre G, Vazquez P, Agullo-Lopez F, Torres T. Role of structural factors in the nonlinear optical properties of phthalocyanines and related compounds. *Chemical Reviews*. 2004;**104**:3723-3750
- [17] Sheik-Bahae M, Said AA, van Stryland EW. High-sensitivity, single-beam n_2 measurements. *Optical Letters*. 1989;**14**:955-957
- [18] Sheik-Bahae M, Said AA, Wei TH, Hagan DJ, van Stryland EW. Sensitive measurement of optical nonlinearities using a single beam. *IEEE Journal of Quantum Electronics*. 1990;**26**:760-769
- [19] Georgakias V, Otyepka M, Bourlinos AB, Cgandra V, Kim N, Kemp KC, Hobza P, Zboril R, Kim KS. Functionalization of graphene: Covalent and non-covalent approaches, derivatives and applications. *Chemical Reviews*. 2012;**112**:6156-6214
- [20] Paula M, Gil G, Sandra C, Nuno A, Manoj SJG, António S. Functionalized graphene nanocomposites. In: Hashim A, editors. *Advances in Nanocomposite Technology*. Croatia: InTech; 2011. pp. 247-272
- [21] Chen Y, Hanack M, Araki Y, Ito O. Axially modified gallium phthalocyanines and naphthalocyanines for optical limiting. *Chemical Society Reviews*. 2005;**34**:517-529
- [22] Wang AJ, Long LL, Meng SC, Li XF, Zhao W, Song YL, Cifuentes MP, Humphrey MG, Zhang C. Cooperative enhancement of optical nonlinearities in a porphyrin derivative bearing a pyrimidine chromophore at the periphery. *Organic & Biomolecular Chemistry*. 2013;**11**:4250-4257

- [23] Li GF, Wang AJ, Song JB, Zhou Q. A novel zinc tetraphenylporphyrinate substituted in the axial position with one E-stilbazole: Synthesis, structure, and nonlinear optics. *Inorganic Chemistry Communications*. 2015;**57**:47-50
- [24] Xu YF, Liu ZB, Zhang XL, Wang Y, Tian JG, Huang Y, Ma YF, Zhang XY, Chen YS. A graphene hybrid material covalently functionalized with porphyrin: Synthesis and optical limiting property. *Advanced Materials*. 2009;**21**:1275-1279
- [25] Liu ZB, Xu YF, Zhang XY, Zhang XL, Chen YS, Tian JG. Porphyrin and fullerene covalently functionalized graphene hybrid materials with large nonlinear optical properties. *The Journal of Physical Chemistry B*. 2009;**113**:9681-9686
- [26] Wang AJ, Yu W, Xiao ZG, Song YL, Long LL, Cifuentes MP, Humphrey MG, Zhang C. A 1,3-dipolar cycloaddition protocol to porphyrin-functionalized reduced graphene oxide with a push-pull motif. *Nano Research*. 2015;**8**:870-886
- [27] Wang AJ, Yu W, Huang ZB, Zhou F, Song JB, Song YL, Long LL, Cifuentes MP, Humphrey MG, Zhang L, Shao JD, Zhang C. Covalent functionalization of reduced graphene oxide with porphyrin by means of diazonium chemistry for nonlinear optical performance. *Scientific Reports*. 2016;**6**:23325
- [28] Xu T, Lu R, Liu X, Zheng X, Qiu X, Zhao Y. Phosphorous(V) porphyrins with axial carbazole-based dendritic substituents. *Organic Letters*. 2007;**9**:797-800
- [29] Wang AJ, Long LL, Zhao W, Song YL, Humphrey MG, Cifuentes MP, Wu XZ, Fu YS, Zhang DD, Li XF, Zhang C. Increased optical nonlinearities of graphene nanohybrids covalently functionalized by axially-coordinated porphyrins. *Carbon*. 2013;**53**:327-338
- [30] Wang AJ, Song JB, Jia D, Yu W, Long LL, Song YL, Cifuentes MP, Humphrey MP, Zhang L, Shao JD, Zhang C. Functionalization of reduced graphene oxide with axially-coordinated metal-porphyrins: Facile syntheses and temporally-dependent nonlinear optical properties. *Inorganic Chemistry Frontiers*. 2016;**3**:296-305
- [31] Zhu JH, Li YX, Chen Y, Wang J, Zhang B, Zhang JJ, Blau WJ. Graphene oxide covalently functionalized with zinc phthalocyanine for broadband optical limiting. *Carbon*. 2011;**49**:1900-1905
- [32] Li YX, Zhu JH, Chen Y, Zhang JJ, Wang J, Zhang B, He Y, Blau WJ. Synthesis and strong optical limiting response of graphite oxide covalently functionalized with gallium phthalocyanine. *Nanotechnology*. 2011;**22**:205704
- [33] Song WN, He CY, Zhang W, Gao YC, Yang YX, Wu YQ, Chen ZM, Li XC, Dong YL. Synthesis and nonlinear optical properties of reduced graphene oxide hybrid material covalently functionalized with zinc phthalocyanine. *Carbon*. 2014;**77**:1020-1030
- [34] Wang Z, He CY, Song WN, Gao YC, Chen ZM, Dong YL, Zhao C, Li ZL, Wu YQ. The effect of peripheral substituents attached to phthalocyanines on the third order nonlinear optical properties of graphene oxide-zinc(II) phthalocyanine hybrids. *RSC Advances*. 2015;**5**:94144-94154

- [35] Song WN, He CY, Dong YL, Zhang W, Gao YC, Wu YQ, Chen ZM. The effects of central metals on the photophysical and nonlinear optical properties of reduced graphene oxide-metal(II) phthalocyanine hybrids. *Physical Chemistry Chemical Physics*. 2015;**17**:7149-7157
- [36] Muhammad S, Nasayoshi N, Al-Sehemi AG, Kitagawa Y, Irfan A, Chaudhry AR, Kishi R, Ito S, Yoneda K, Fukuda K. Role of a single diradical character in carbon nanomaterials: A novel hot spot for efficient nonlinear optical materials. *Nanoscale*. 2016;**8**: 17998-18020
- [37] Avouris P, Freitag M, Perebeinos V. Carbon-nanotube photonics and optoelectronics. *Nature Photonics*. 2008;**2**:341-350
- [38] Xu Y, Xiong GG. Third-order optical nonlinearity of semiconductor carbon nanotubes for third harmonic generation. *Chemical Physics Letters*. 2004;**388**:330-336
- [39] Liu XC, Si JH, Chang BH, Xu G, Yang QG, Pan ZW, Xie SS, Ye PX. Third-order optical nonlinearity of the carbon nanotubes. *Applied Physics Letters*. 1998;**74**:164-166
- [40] Liu ZB, Tian JG, Guo Z, Ren DM, Du F, Zheng JY, Chen YS. Enhanced optical limiting effects in porphyrin-covalently functionalized single-walled carbon nanotubes. *Advanced Materials*. 2008;**20**:511-515
- [41] Liu ZB, Guo Z, Zhang XL, Zheng JY, Tian JG. Increased optical nonlinearities of multi-walled carbon nanotubes covalently functionalized with porphyrin. *Carbon*. 2013;**51**:419-426
- [42] Wang AJ, Fang Y, Yu W, Long LL, Song YL, Zhao W, Cifuentes MP, Humphrey MG, Zhang C. Allyloxyporphyrin-functionalized multiwalled carbon nanotubes: Synthesis by radical polymerization and enhanced optical-limiting properties. *Chemistry-An Asian Journal*. 2014;**9**:639-648
- [43] Wang AJ, Fang Y, Long LL, Song YL, Yu W, Zhao W, Cifuentes MP, Humphrey MG, Zhang C. Facile synthesis and enhanced nonlinear optical properties of porphyrin-functionalized multi-walled carbon nanotubes. *Chemistry-A European Journal*. 2013;**19**: 14159-14170
- [44] Wang AJ, Song JB, Huang ZP, Song YL, Yu W, Dong HL, Hu WP, Cifuentes MP, Humphrey MG, Zhang L, Shao JD, Zhang C. Multi-walled carbon nanotubes covalently functionalized by axially coordinated metal-porphyrins: Facile syntheses and temporally dependent optical performance. *Nano Research*. 2016;**9**:458-472
- [45] He N, Chen Y, Bai JR, Wang J, Blau WJ, Zhu JH. Preparation and optical limiting properties of multiwalled carbon nanotubes with π -conjugated metal-free phthalocyanine moieties. *The Journal of Physical Chemistry C*. 2009;**113**:13029-13035
- [46] Sanusi K, Amuhaya EK, Nyokong T. Enhanced optical limiting behavior of an indium phthalocyanine-single-walled carbon nanotube composite: An investigation of the effects of solvents. *The Physical of Physical Chemistry C*. 2014;**118**:7057-7069

Sol-Gel Processes of Functional Powders and Films

Chao-Qun Ye

Additional information is available at the end of the chapter

<http://dx.doi.org/10.5772/intechopen.69588>

Abstract

The key principles of sol-gel process and its characteristics are outlined and its major control parameters are summarized. Different samples of functional powders and films with magnetic, optical, and dielectric properties prepared by the sol-gel method are described. To determine the relationship between microstructure and properties, the effects of preparation conditions on the size and microstructure and electric properties, dielectric properties, optical properties, and magnetic properties are analyzed.

Keywords: sol-gel, magnetic, optical properties, dielectric, CCTO, multiferroics, hexagonal ferrite, YFeO_3

1. Introduction

Sol-gel processing is a well-recognized, cost-competitive, bottom-up synthesis technique, which is used in the field of material science and ceramic engineering for the generation of oxide nanopowder and composite NPs from a sol followed by a gel formation [1]. Functionality refers to typical chemophysical properties owned by materials, which makes them possible to be exploited in technological applications, as in electrical conductors, thermoelectrics, ferroelectrics, magnets, and transparent optical devices. The sol-gel process of functionality opens promising applications in many areas, such as optics, electronics, ionics, mechanics, energy, environment, biology, medicine, for example as membranes and separation devices, fuel and solar cells, catalysts, sensors, and functional smart coatings. Sol-gel-derived coatings provide a wide range of applications, such as corrosion protective, hydrophilic, hydrophobic, antireflective, and antifog coatings; migration barriers against liquid and volatile compounds; antibacterial modification of textiles and water-repellent antistatic textiles; and self-cleaning coatings [2].

The sol-gel method initial study can be traced back to 1846, when Ebelmen found SiCl_4 mixed with ethanol in the wet air hydrolysis and formation of gel. The process of making tofu in ancient China may be the first method to use sol-gel technology in a purposeful and effective way; the soybean protein solution was flocculated into a solid bean curd (gel). Until the end of 1930s, W. Geffeken can conduct oxide film preparation through metal alkoxide hydrolysis and gelation. In 1971 in Germany, H. Dislich reported sol by the hydrolysis of metal alkoxides, after gelation and retreatment in 923–973 K and high pressure resulting in the formation of $\text{SiO}_2\text{-B}_2\text{O}_3\text{-Al}_2\text{O}_3\text{-Na}_2\text{O-K}_2\text{O}$ multicomponent glass, which aroused great interest and attention in the field of material science. In 1975, B. E. Yoldas and M. Yamane dried the gel to prepare monolithic ceramic materials and porous transparent alumina films. Since 1980s, sol-gel technology has been successfully applied in glass, oxide coatings, and functional ceramic powders, especially composite oxide such as high critical temperature superconducting oxide material synthesis which is difficult to prepare by traditional method.

2. Key principles of sol-gel process and its characteristics

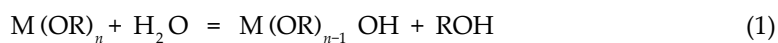
Sol is a system of tiny solid particles suspended in the liquid phase and constantly showing Brownian movement. Because the Gibbs free energy of the interface atoms is higher than that of the internal atoms, the sol is thermodynamically unstable. The particles tend to agglomerate spontaneously, reaching a low surface energy state. If the process is reversible, it is called flocculation; if not reversible, it is called gelation. The gel is a kind of solid feature of the colloidal system composed of fine particles in three-dimensional network structure and a continuous medium consisting of dispersed phase. The transition process to the gel can be briefly described as the formation of the polymer or the particle aggregates formed by the condensation reaction into a small particle cluster and gradually connected to a three-dimensional network structure. Therefore, the gelation process can be regarded as a small particle cluster connected to each other as a continuous solid network.

Sol-gel processes are mainly based on hydrolysis and condensation reactions of metal alkoxides, the molecular precursors that develop an oxide network in a liquid medium [3].

The structures of oxide materials change from nanoparticles to gel according to the reaction rate and the subsequent drying and post-treatment [2, 4–6].

Accurate control of the sol-gel reaction parameters can be designed to produce many forms of certain properties of the materials in the form of glass, fiber, ceramic powder, and thin film (Figure 1).

According to the types of precursors, the sol-gel process can be divided into two types: organic and inorganic. The organic route is that the sol-gel is prepared by metal alkoxides which can be considered as a two-step inorganic polymerization. The first step is the hydrolysis of alkoxide ligands to yield hydroxylated metal centers [7]:



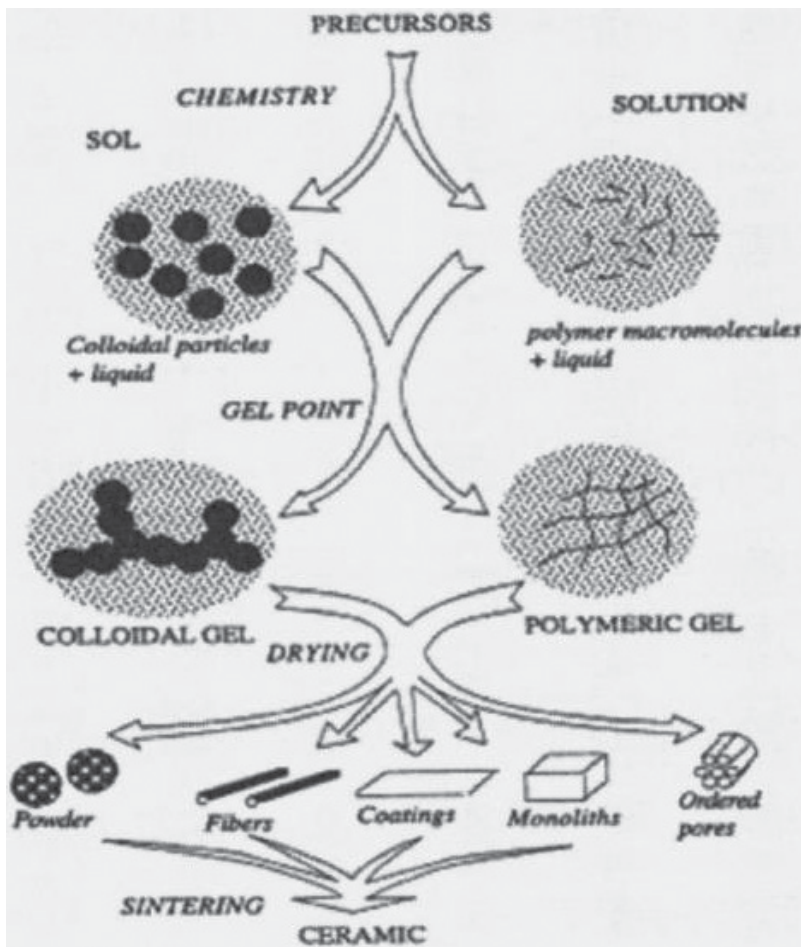


Figure 1. Schematic diagram of the sol-gel process.

The second step is the condensation of the hydroxylated species to form oxypolymers, involving an oxylation reaction which creates oxygen bridges and expels XOH species as follows [7]:



3. Major control parameters of sol-gel process

The macroscopic properties of the material are determined by its microstructure, and the microstructure is determined by the conditions of the material.

Generally speaking, the sintering properties of the powder vary in different preparation methods. While using large surface area and high surface activity of monodisperse ultrafine

ceramic powder, due to short diffusion distance and only need lower sintering temperature and activation energy.

Factors that influence the properties of final products, acquired by sol-gel technique, include hydrolysis ratio, acidity of the hydrolyzing agent, gelation condition, drying condition and procedures and types of solvent.

3.1. Chemical compositions of the precursors

The nature of the precursor can significantly affect the sol-gel reaction kinetics and final products.

3.2. Hydrolysis ratio

The hydrolysis ratio, as defined by Eq. (3), is the main external parameter and has been shown to be important in controlling the hydrolysis and condensation of metal alkoxides [5]:

$$h = [\text{H}_2\text{O}]/[\text{M}(\text{OR})_z] \quad (3)$$

where $[\text{H}_2\text{O}]$ and $[\text{M}(\text{OR})_z]$ are the molar numbers for the water and metal alkoxide, respectively; z is the valance charge of metal M.

The lower amount of water added is easy to form the product of low crosslinking, and the viscosity of the sol is increased; the higher amount of water added is easy to form a highly cross-linked product, and the viscosity is decreased. Therefore, the amount of water has an important effect on the structure of the product and the viscosity and gelation time. When $h < 1$, water molecules are not sufficient for complete hydrolysis, and thus gelation or precipitation cannot occur. When $1 < h < z$, chain oxypolymers can form. When $h > z$, cross-linked oxypolymers can be obtained and nanoparticles or gels can be formed. The hydrolysis ratio also has a great influence on the hydrolysis and condensation rate. When h is low ($< \sim 1$), the hydrolysis rate is low, so the sol-gel reaction rate including hydrolysis and condensation is also slow. When h is high ($> \sim 7$), the hydrolysis rate is high, but the condensation rate is low, the result being a slow sol-gel reaction. When h is intermediate ($1 < h < 7$), the sol-gel reaction is the fastest because of high rates of both hydrolysis and condensation [7].

3.3. Catalysts

Both acids and bases can catalyze sol-gel reactions. The hydrolysis and condensation reactions can be explained by SN2 nucleophilic substitution reaction mechanism. Take alcohol as an example, it is not easy to hydrolyze silicon alkoxide, and its hydrolysis and polymerization are usually catalyzed by acid or alkali. The inorganic acid can make the partially negatively charged alkoxy matrix, so that it is easy to break away from the silicon atom. Alkali provides nucleophilic hydroxyl OH in alkali-catalyzed hydrolysis, and Si—OH loss of protons, thereby accelerating polymerization. In the presence of excess water, because of the acid-catalyzed hydrolysis reaction, Si(OH) can be formed. The rate of polymerization is faster than that of

hydrolysis under the condition of alkali catalysis. Acid or base catalysis is not the only catalyst. Some nucleophiles, such as NaF or 2-methylpyridine, also have the ability to improve the reaction rate.

3.4. pH value

Zinc oxide (ZnO) nanoparticles were prepared and synthesized via sol-gel method, using citric acid as a precursor. The annealing temperature was fixed at 600°C. The impact of pH on the particle size was investigated. Three different pH (3.0, 5.0, and 1.01) for the precursor were chosen, and it was revealed that the Zn NPs size increased with the alkalinity of the precursor [8]. The pH value of the sol-gel solution will change when added with acids and alkalis to catalyze the reactions. Experimental results show that the pH value and hydrolysis ratio have a synergistic effect on the morphologies of the products.

3.5. Reaction temperature

Generally, increasing temperature results in both hydrolysis and condensation rate increase [6, 7].

4. Advantages and shortages of sol-gel processing

The sol-gel process provides samples with high purity, homogeneity, and structure of easy control. The most important advantages of the sol-gel process in the preparation of functional materials are as follows:

- (i) In all stages, the temperatures required are low and close to room temperature. Then, thermal decomposition of organic material and any entrapped species is minimized leading to high purity and stoichiometry [2].
- (ii) As the organometallic precursors for different metals are miscible, the homogeneous sol solutions are easily achieved [2]. Since the sol-gel is initiated by the reaction of the solution, the materials are very uniform and easy to modify, which is crucial for controlling the physical and chemical properties of the material.
- (iii) Precursors such as metal alkoxides and mixed alkyl/alkoxides are easily purified by common techniques (e.g., distillation or sublimation), which lead to high-purity products [2].
- (iv) The chemical conditions are mild in sol-gel process. Hydrolysis and condensation are catalyzed by acid or alkali under mild pH conditions [2, 9].
- (v) Highly porous and nanocrystalline materials can be synthesized by this method [2].
- (vi) Colloid particle size and pore size, porosity, and chemistry of the final product can be optimized by chemical treatment of the precursors, controlled rates of hydrolysis, and by condensation [2].

- (vii) Incorporating several components in a single step or in two steps [2].
- (viii) Production of samples in different physical forms [2, 10]. Starting from the same raw material, changing the process can get different products, such as fiber, powder, or film and composite materials.
- (ix) Treating temperature is low, the inorganic materials can be synthesized under the condition of low temperature at about 600°C, the composition and the structure of the product are uniform, the grain size is small, the activity of the material particles is increased, and the performance of the material is expanded.
- (x) Suitable for large-scale industrial production.

The negative factors of sol-gel processing include high precursor cost, overall high cost, and environmental problems associated with the disposal of large quantities of organic by-products. A common theme out of the negative comments was wet chemical processing using alkoxides as precursors [11].

The sol-gel process is more complex in terms of the difficulty in phase control, which is the different chemical and crystal morphology formation at different temperatures. The morphology is relatively simple, generally, spherical particles.

Gelation, drying, and heat treatment take a lot of time to prepare the sample. In the stage of drying and heat treatment, the sample has a great weight loss and residual stress, film prone to cracking and objectively restricting the thickness of thin film and result in film residual porosity.

5. Sol-gel processing of functional powder materials

5.1. Multiferroic properties of powder materials

First, $\text{Y}(\text{NO}_3)_3 \cdot 5\text{H}_2\text{O}$ and $\text{Fe}(\text{NO}_3)_3 \cdot 9\text{H}_2\text{O}$ were dissolved in deionized water in the molar ratio of $n(\text{Y}):n(\text{Fe}) = 1:1$, then citric acid and metal cations were added in the molar ratio of 1.5:1 to dissolve them completely and for the full complexation with metal ions. The acrylamide monomer is added in the ratio of 9:1 to the cation. The mixture at 358 K temperature is heated to polymerize to form a gel at 393 K. The dry gel is crushed into fine powder with a mortar, placed in a muffle furnace with different calcination temperature for 10 h, with the furnace cooling to room temperature to get fine powders of YFeO_3 . Vibrating sample magnetometer (VSM, Model 7300, Lake Shore) and MPMS magnetic measurement system (SQUID, Quantum, Design) were used at room temperature to measure the temperature curve of the magnetic hysteresis loop. The powder samples and a small amount of ethanol were mixed after grinding and were compressed at a molding pressure of about 300 Mpa in the muffle furnace sintering at 923 K and 1173 K for 2 h. Silver paste dried at 353 K was used as the electrode. The sample thickness was about 1.5 mm, and the diameter was about 15 mm. The capacitance and loss were measured by Agilent 4980E LCR analyzer and TH 2617 capacitance measuring instrument, and the temperature and magnetic field were controlled by ET 9000 low-temperature measuring system.

Figure 2 shows the room temperature hysteresis loop and magnetization temperature curve of h-YFO powder. As can be seen from **Figure 2**, h-YFO has a weak magnetism, and the hysteresis loop is narrow and small, which belongs to the soft magnet. The remanent magnetization (M_r) and coercive field (H) are 0.11 memu g^{-1} and 0.19 kOe , respectively. The coercivity and saturation magnetization of possible impurities $\text{Y}_3\text{Fe}_5\text{O}_{12}$ and $\gamma\text{-Fe}_2\text{O}_3$ are about 100 Oe and 26.0 memu g^{-1} and 150 Oe and 70 memu g^{-1} at room temperature, respectively [12, 13].

The magnetization of h-YFO is very small and the coercive field is much larger, so it is possible to exclude the influence of impurities on the magnetic properties of the samples, which is characterizing the magnetic properties of h-YFO.

Figure 3 shows the h-YFO magnetization-temperature relationship curve (M-T) and its first derivative curve (dM/dT -T), measured at the external magnetic field strength of $H = 1000 \text{ Oe}$ using temperature mode. It can be seen from the figure that the magnetization of h-YFO is gradually reduced from 0.72 memu g^{-1} to about zero in the temperature range of 750 K to 877 K , which indicates that h-YFO has a complex magnetic phase transition in this temperature range.

Figure 4 shows the hysteresis loop and the magnetization temperature curve of o-YFO powder at room temperature. Compared to h-YFO, the hysteresis loop of o-YFO is wide which belongs to hard magnet, and the magnetization and coercive field of o-YFO is 0.72 memu g^{-1} and 24.5 kOe respectively which is much larger than h-YFO. It is also shown that the influence of impurities on the magnetic properties is small. From the extension direction of the loop line, o-YFO has a certain antiferromagnetic property.

It is worth noting that **Figure 4** illustrations for the hysteresis curve of o-YFO on a small magnetic field ($<10 \text{ kOe}$) that shows a peculiar shape with a sudden change magnetization in $H = 0 \text{ kOe}$, which is considered to be the inherent characteristic of o-YFO. The causes of the abnormal YFeO_3 hysteresis loop are produced by the interaction of the same iron ions, the interaction with the external magnetic field, the DM antisymmetric interaction, and the anisotropy effect of the magnetic crystal. The adjacent two iron ions in YFeO_3 is of a slight distortion,

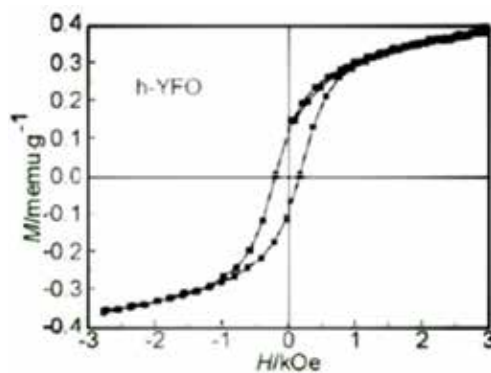


Figure 2. M-H hysteresis curve of h-YFO powder.

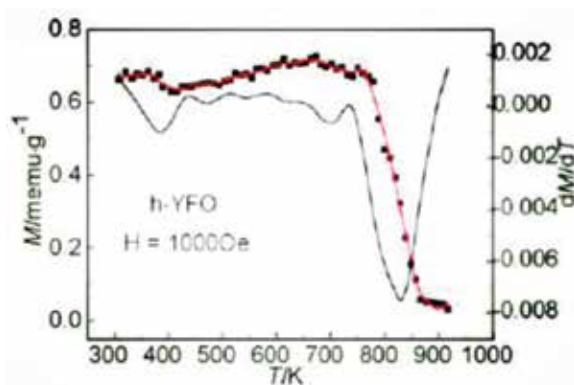


Figure 3. M-T curve of h-YFO powder and its derivative curve.

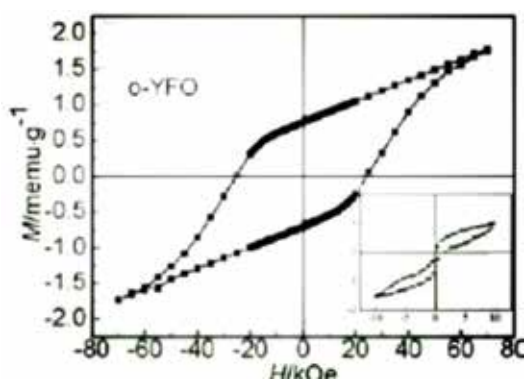


Figure 4. M-H hysteresis curve of o-YFO powder. Inset: M-H hysteresis curve of o-YFO at lower magnetization field.

rather than a strict spin antiparallely which reveals overall magnetic anisotropy. When the external magnetic field is too small to overcome the anisotropic magnetic field of the magnetic material, the magnetic behavior will be different.

Figure 5 shows the magnetization-temperature curve (M-T) and its first derivative curve (dM/dT-T) for o-YFO, measured in the same way those for h-YFO. The magnetic properties of o-YFO become smaller in the range of 540 K till 645 K, the magnetization is 0, which is similar to the Nair temperature $T_N = 640$ K of the orthorhombic phase YFO, which indicates that the magnetic phase transition process is from antiferromagnetic to paramagnetic.

Figures 6 and 7 show the ϵ_r and dielectric loss $\tan \delta$ of h-YFO variation with temperature in the range of 1 kHz to 300 kHz. It can be seen from the figure that the dielectric constant of h-YFO in the whole frequency range is relatively low, about 10–30, and the dielectric constant and dielectric loss of the sample decrease slightly with the increase in the measurement frequency. In the whole temperature range, there are three obvious dielectric anomalies. The first dielectric anomaly was observed in 125–250 K; the ϵ_r -T curve shows the dielectric relaxation and frequency dispersion characteristics. With the

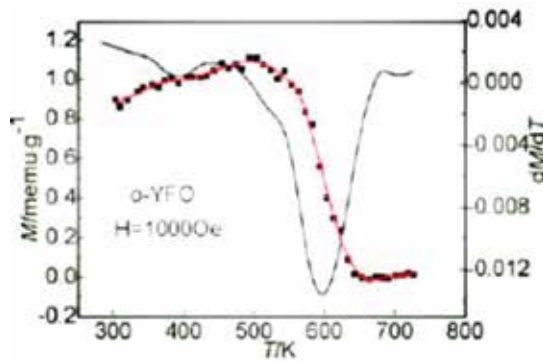


Figure 5. M-T curve of o-YFO powder and its derivative curve.

increase in the electric field frequency, the relaxation peak moves to the high temperature and the peak value decreases gradually. At the same time, the dielectric loss curve also has the corresponding loss peak, the loss peak moves to the high temperature with the increase in the frequency, and the peak value of the loss increases. The second dielectric anomaly appeared between 250 and 340 K and h-YFeO₃ showed a dielectric anomaly peak at 297 K, and the dielectric peak does not change with the frequency shows that the peak is not caused by the thermal activation, but by a structural phase transition. The third anomalous dielectric is at above 340 K where exists a strong frequency dispersion and the loss increases obviously. It is because the thermal activation mobility of charge carrier increases with the temperature rises, which result in the increase of conductivity. At 300 kHz, the dielectric loss was relatively stable, the main reason was that no electric charge was generated with the change of external electric field. It can be seen from the figure that ϵ_r and dielectric loss $\tan \delta$ of o-YFeO₃ have a trend of decline in the highest temperature.

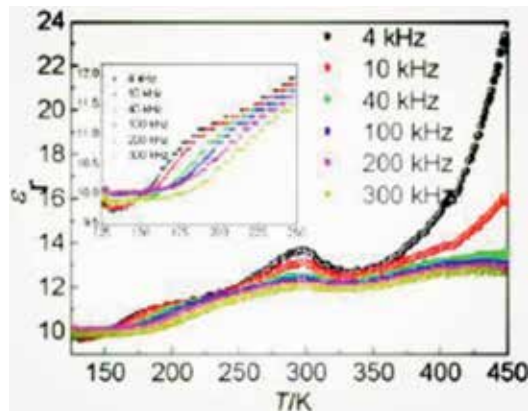


Figure 6. Temperature dependence of dielectric constant ϵ_r of h-YFO.

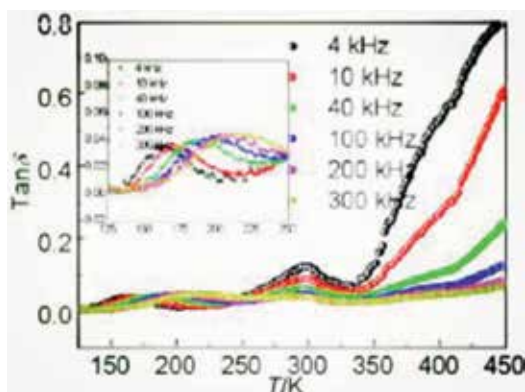


Figure 7. Temperature dependence of dielectric loss $\tan \delta$ of h-YFO.

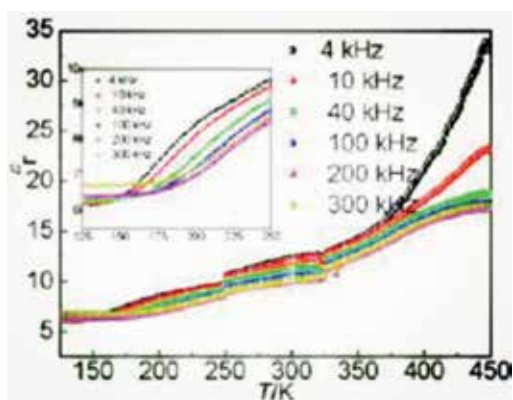


Figure 8. Temperature dependence of dielectric constant ϵ_r of o-YFO.

Figures 8 and 9 show the dielectric constant and dielectric loss $\tan \delta$ variation with temperature at different frequency from 1 kHz to 300 kHz of o-YFeO₃. As can be seen from the figure, o-YFeO₃ has two obvious dielectric anomalies in the whole range of temperature. The ϵ_r - T curve of o-YFeO₃ shows the dielectric relaxation and frequency dispersion phenomenon in the range of 125–340 K. With the increase in electric field frequency, the dielectric constant decreased, the dielectric loss increased, and the dielectric peak shifted to high temperature with the longer dielectric platform afterward. After 340 K, there are second obvious dielectric anomalies, showing a strong frequency dispersion, which is consistent with the change of h-YFeO₃. The dielectric relaxation behavior of o-YFeO₃ is the result of the decrease of dielectric constant.

5.2. Optical properties of powder materials

For semiconductor nanomaterials, the optical absorption is closely related to the band gap. The short wavelength cutoff in the transmission is due to the fundamental band gap excitation

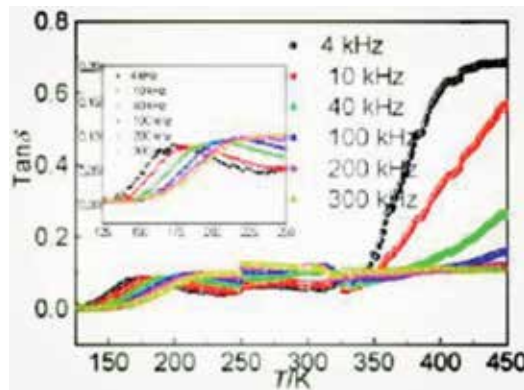


Figure 9. Temperature dependence of dielectric loss $\tan \delta$ of o-YFO.

from the valence band to the conduction band. Energy band gap of samples can be evaluated from the absorption spectra.

$(\text{La}_{(1-x)}\text{Sr}_x)(\text{Fe}_{(1-x)}\text{Ni}_x)\text{O}_3$ ($x = 0.0, 0.1$ and 0.2) NPs were synthesized by sol-gel combustion method. The raw materials were used in analytical grade (AR). Lanthanum nitrate hexahydrate ($\text{La}(\text{NO}_3)_3 \cdot 6\text{H}_2\text{O}$), ferric nitrate nonahydrate ($\text{Fe}(\text{NO}_3)_3 \cdot 9\text{H}_2\text{O}$), strontium nitrate ($\text{Sr}(\text{NO}_3)_2$), and nickel nitrate hexahydrate ($\text{Ni}(\text{NO}_3)_2 \cdot 6\text{H}_2\text{O}$) were used as oxidizing agents, whereas citric acid ($\text{C}_6\text{H}_8\text{O}_7$) was used as fuel. All chemicals were completely dissolved in 100 mL diluted water in a beaker under the constant stirrer at 60°C until the homogeneous sol was formed. Ammonia (NH_3) was slowly added to adjust the pH to 7. Afterward, the homogeneous sol was heated at 120°C for 2.5 h. The sol color and viscosity changed and got ignited for further heating automatically. The solid dry gel was calcinated at 600°C in air for 5 h. The UV-Vis absorbance was carried out using Perkin Elmer spectrophotometer [14].

The optical absorption spectra as a function of wavelength of $(\text{La}_{(1-x)}\text{Sr}_x)(\text{Fe}_{(1-x)}\text{Ni}_x)\text{O}_3$ ($x = 0.0, 0.1$ and 0.2) NPs is shown in (**Figure 10**). The band gap of semiconductor materials can be estimated by UV-Vis absorption spectroscopy by the Tauc relation given below:

$$(\alpha h\nu)^m = K(h\nu - E_g) \quad (4)$$

where α is the absorption coefficient, K is a constant, m is an integer whose value depends on the nature of transition. The value of m is 2, $1/2$, $2/3$, and $1/3$ for acceptable direct transition, permitted indirect transition, forbidden direct transition, and forbidden indirect transition, respectively [14].

The plots of $(\alpha h\nu)^2$ versus photon energy ($h\nu$) for direct transitions to determine the band gap of the $(\text{La}_{(1-x)}\text{Sr}_x)(\text{Fe}_{(1-x)}\text{Ni}_x)\text{O}_3$ ($x = 0.0, 0.1$ and 0.2) NPs are displayed in **Figure 11**, which indicate that the band gap increases with increasing Sr and Ni concentrations. The increase in the band gap could be attributed to the Burstein-Moss effect with an obvious blue shift of the absorption edge [14].

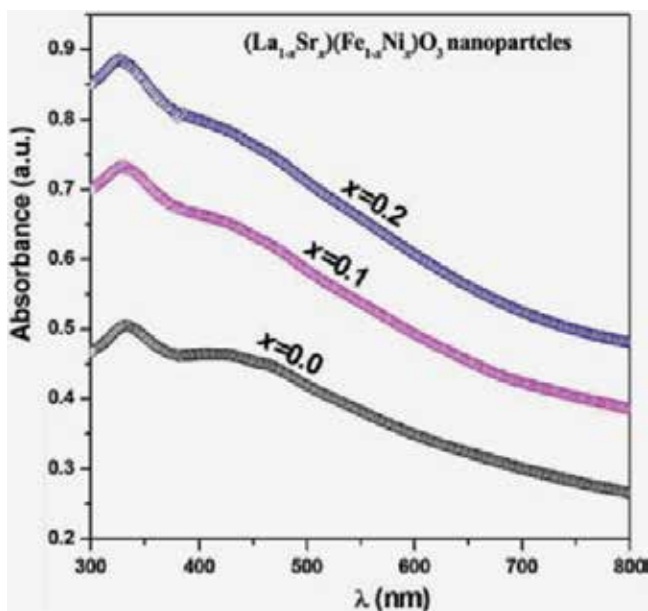


Figure 10. UV-Vis absorption spectrum of the NPs of $(La_{1-x}Sr_x)(Fe_{1-x}Ni_x)O_3$ ($x = 0.0, 0.1$ and 0.2).

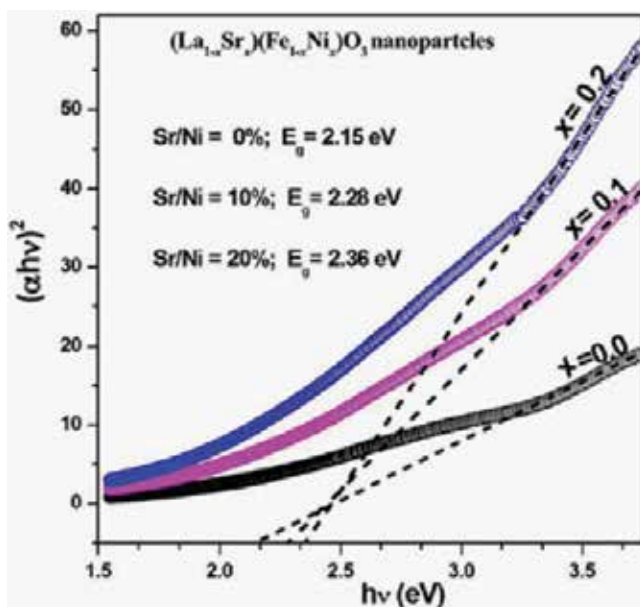


Figure 11. Plot of $(\alpha hv)^2$ versus hv for NPs of $(La_{1-x}Sr_x)(Fe_{1-x}Ni_x)O_3$ ($x = 0.0, 0.1$ and 0.2) NPs.

With the increase in the concentration of doping, the donor states push the Fermi level higher in energy, which shift close to the conduction band above the occupied donor state. In the degenerate semiconductor, only an electron can be excited from the valence band into

conduction band above the Fermi level. Based on the Pauli's exclusion principle this excitation into occupied states is prohibited, resulting in the increase in the optical band gap [14].

6. Sol-gel processes of functional film

Sol-gel-derived coating film is suitable for substrates with large areas. Preferred crystal orientation can be given depending on the conditions of preparation. The techniques can be applied to accomplishing a large variety of functional films with optical, electronic, magnetic, chemical, and mechanical functions.

In sol-gel process, the key film-forming method mainly includes the dip-coating method, the rotating method, the sputtering method, and so on. The dip-coating method is elevating impregnated substrate from uniform solution, after gelling process, to become gel, and the film with nanoparticles can be obtained after a certain temperature, and the film thickness can be controlled by the number of pulling speed or spin coating. The rotation method is a method of liquid film coating on substrate, the film thickness reduces with the increase in the substrate rotation speed. Sputtering is a method of forming film by spraying the solution from one to several stationary sputtering guns onto a preheated substrate which runs at a certain speed.

6.1. Dielectric properties of the perovskite-related oxide CCTO film

Perovskite-related oxide $\text{CaCu}_3\text{Ti}_4\text{O}_{12}$ (CCTO) ceramic has an extremely high dielectric constant ($\sim 10,000$ for bulk and $\sim 10^5$ for single crystals) and moderately lower dielectric loss (~ 0.1) at low frequencies with centrosymmetric bcc structure (space group $\text{Im}\bar{3}$ (no. 204), lattice parameter $a = 0.7391$ nm and $Z = 2$). And it retains its high dielectric constant from 100 to 600 K. Hence, it is capable of potential industrial application for miniaturizing electronic devices [15].

Calcium nitrate ($\text{Ca}(\text{NO}_3)_2 \cdot 4\text{H}_2\text{O}$), copper nitrate ($\text{Cu}(\text{NO}_3)_2 \cdot 4\text{H}_2\text{O}$), and tetrabutyl titanate ($\text{Ti}(\text{OC}_4\text{H}_9)_4$) were selected as solutes; ethylene glycol monomethyl ether ($\text{CH}_3\text{OCH}_2\text{CH}_2\text{OH}$) as solvent; dilute nitric acid as stabilizer; acetic acid as chelating agent; and citric acid as colloidal complexing agent. Zirconium nitrate ($\text{Zr}(\text{NO}_3)_4$) was used to introduce Zr elements as doping agents in the sol. Stoichiometric calcium nitrate ($\text{Ca}(\text{NO}_3)_2 \cdot 4\text{H}_2\text{O}$) and copper nitrate ($\text{Cu}(\text{NO}_3)_2 \cdot 4\text{H}_2\text{O}$) were dissolved in methoxyethanol. Subsequently, the solution was heated and stirred to be fully clarified and was cooled to room temperature (select appropriate amount of zirconium nitrate ($\text{Zr}(\text{NO}_3)_4$) as the introduction of Zr doping agents for the preparation of Zr-doped $\text{CaCu}_3\text{Ti}_4\text{O}_{12}$) with a certain dose of dilute nitric acid, and then a stoichiometric amount of tetrabutyl titanate was added. Citric acid ($\text{C}_6\text{H}_8\text{O}_7 \cdot \text{H}_2\text{O}$) in the ratio of 1:1.5 of sum of the metal ions to the number of moles of citric acid was placed into the solution as complexing agent. By mixing completely, the transparent homogeneous solution of concentration 0.15 mol/L was formed. The solution was aged for 24 h to prepare the powder. Then it was calcined at 450°C for pyrogenic decomposition, and a brown, black powder was obtained. As-prepared powder was made into bulk samples, 10 mm in diameter and 2 mm

in thickness at 20 MPa pressure. Samples were sintered at 1000°C in silicon carbide furnace for 2 h and dense polycrystalline ceramic flakes were formed. The furnace heating rate was 100°C/h and the cooling rate was 150°C/h.

The densities of samples were measured by Archimedes method. The crystalline phases were identified by powder X-ray diffraction analysis installation of a spectrum analyzer with CuK_α radiation ($\lambda = 0.154056 \text{ nm}$) (XRD, D/max-IIIC) in a wide range of 2θ ($5^\circ \leq 2\theta \leq 85^\circ$). The samples' microstructure were characterized by SEM (Philips XL30 ESEM-TMP). For the electrical characterization, the ceramics were cut into small pieces of $5 \times 5 \text{ mm}$, and gold electrodes with 3 mm radii were sputtered at the center on both sides of each sample. The dielectric properties and impedance analyses were carried out using the precision LCR meter (Agilent 4284A) in the frequency range from 20 Hz to 1 MHz over the temperature range of 150–550 K. The measurement accuracy of the instrument is better than 5%. The dielectric permittivity was evaluated using the standard relation $\epsilon_r = C \cdot d / (\epsilon_0 \cdot A)$, where C is capacitance, d is the thickness of the sample, $\epsilon_0 = 8.854 \times 10^{-12} \text{ F/m}$, and A is the effective area of the sample. Dielectric strength measurements were carried out as per the procedure outlined in ASTM D149.

The $\text{CaCu}_3\text{Zr}_{0.05}\text{Ti}_{3.95}\text{O}_{12}$ was confirmed by X-ray diffraction. The X-ray diffraction patterns of pure $\text{CaCu}_3\text{Ti}_4\text{O}_{12}$ and $\text{CaCu}_3\text{Zr}_{0.05}\text{Ti}_{3.95}\text{O}_{12}$ are shown in **Figure 12**. It shows the room temperature XRD patterns obtained for the $\text{CaCu}_3\text{Zr}_{0.05}\text{Ti}_{3.95}\text{O}_{12}$ nanocrystalline powder compared well with the ICDD data (01-075-1149). The samples reveal quite similar diffraction profiles and diffraction peaks corresponding to oxide $\text{CaCu}_3\text{Ti}_4\text{O}_{12}$ phase (JCPDS No. 75-2188) with bcc cubic perovskite-related structure. All the XRD patterns of the main diffraction peaks can be attributed to the CCTO phase. It can determine the crystalline CCTO phase generated. Two curves can be found similar from the figure, which indicate that the content of zirconium has almost no effect on the crystal phase. From the point of view of the ionic radius of Ca^{2+} , Cu^{2+} , and Ti^{4+} , the ionic radius of Ca^{2+} , Cu^{2+} , and Ti^{4+} are 100 pm, 73 pm, and 60.5 pm, respectively, whereas the ionic radius of Zr^{4+} is 79 pm. Through the solution rule of thumb, zirconium is

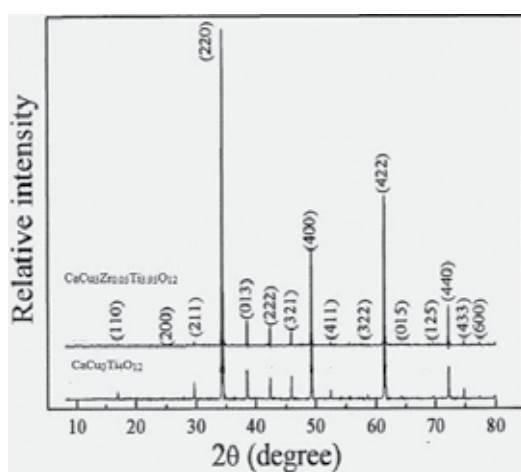


Figure 12. The XRD diffraction patterns for $\text{CaCu}_3\text{Ti}_4\text{O}_{12}$ and $\text{CaCu}_3\text{Zr}_{0.05}\text{Ti}_{3.95}\text{O}_{12}$ powder prepared by the sol-gel process.

likely to replace titanium ions at B site belonging to the perovskite ABO_3 structural ceramics in case of the occurrence of solid solution.

The temperature dependence of dielectric properties of $CaCu_3Ti_4O_{12}$ and $CaCu_3Zr_{0.05}Ti_{3.95}O_{12}$ were studied and are illustrated in **Figure 13**. The dielectric temperature spectra of $CaCu_3Ti_4O_{12}$ and $CaCu_3Zr_{0.05}Ti_{3.95}O_{12}$ ceramics were measured at 100 kHz. Dielectric properties' variation with temperature is relatively flat in the range of 100–350 K. As the temperature increases, the thermal stabilities of $CaCu_3Ti_4O_{12}$ and $CaCu_3Zr_{0.05}Ti_{3.95}O_{12}$ deteriorate. The dielectric property stable temperature zone of $CaCu_3Zr_{0.05}Ti_{3.95}O_{12}$ is narrower than that of $CaCu_3Ti_4O_{12}$, whereas the peak width of $CaCu_3Zr_{0.05}Ti_{3.95}O_{12}$ is larger than that of $CaCu_3Ti_4O_{12}$. In the low frequency regime, the dielectric permittivity of $CaCu_3Zr_{0.05}Ti_{3.95}O_{12}$ increased from 50,000 to 500,000 when the temperature was increased from 420 K to 450 K. This sudden increase in dielectric permittivity observed at 100 kHz may be assigned to the space charge/interfacial polarization effects.

Figures 14 and **15** show the frequency dependence of dielectric permittivity and loss at room temperature for pure $CaCu_3Ti_4O_{12}$ and $CaCu_3Zr_{0.05}Ti_{3.95}O_{12}$, respectively. As the frequency increases in the range of 1 KHz to 1000 KHz, the dielectric constant of CCTO-based ceramics decreased. However, the dielectric loss increased significantly with increasing frequency. The dielectric loss of the test samples in the lower frequency at room temperature are relatively closed and nearly keep constant. With increasing frequency, the dielectric constants of pure $CaCu_3Ti_4O_{12}$ and $CaCu_3Zr_{0.05}Ti_{3.95}O_{12}$ decrease rapidly at low-frequency ranges. Both the CCTO-based ceramics possess large dielectric constant in low-frequency ranges, which is attributed to the interfacial polarization at the interfaces between the two components.

As shown in **Figures 3** and **4**, each sample has similar dielectric behavior at room temperature. The dielectric constant displays a steep decrease at a certain frequency, and at the same time the dielectric loss shows a relaxation peak. There is a clear relaxation characteristic and the relaxation is closely related to the measurement frequency, which shows a typical Debye relaxation.

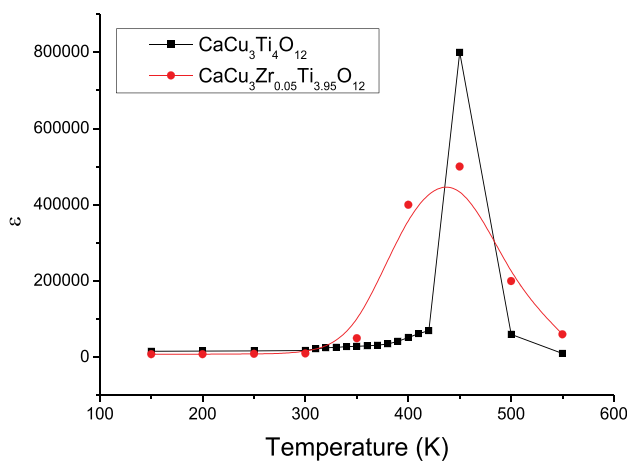


Figure 13. Temperature-dependent dielectric permittivities at 100 kHz for $CaCu_3Ti_4O_{12}$ and $CaCu_3Zr_{0.05}Ti_{3.95}O_{12}$.

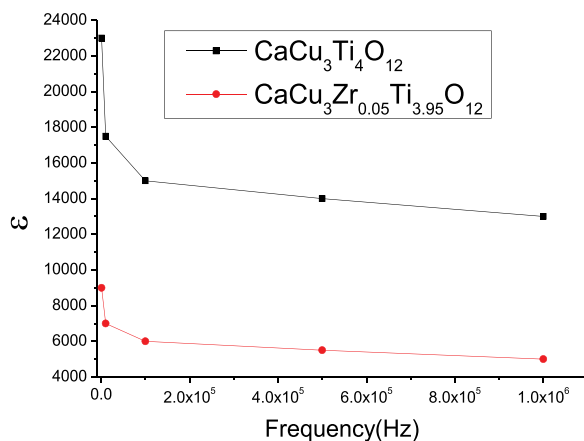


Figure 14. Frequency dependence of room temperature dielectric permittivities for $\text{CaCu}_3\text{Ti}_4\text{O}_{12}$ and $\text{CaCu}_3\text{Zr}_{0.05}\text{Ti}_{3.95}\text{O}_{12}$.

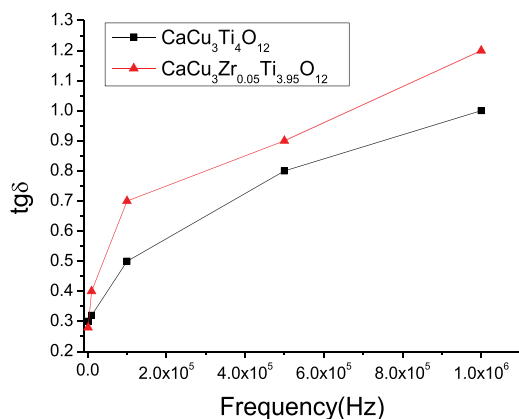


Figure 15. The room temperature dielectric losses for $\text{CaCu}_3\text{Ti}_4\text{O}_{12}$ and $\text{CaCu}_3\text{Zr}_{0.05}\text{Ti}_{3.95}\text{O}_{12}$ at various frequencies.

It is obvious that all of these samples exhibit the giant permittivity at low frequency. As the frequency increases, permittivity has a sudden drop in the frequency range below 100 kHz; and then becomes flat. The permittivity increased with decreasing frequency which signaled the possibility of the presence of interfacial polarization. It is probably that the charge carriers may be blocked at an electrode interface when migrated under the influence of an electric field, which causes interfacial polarization. At the same time, the frequency response of dielectric properties of CCTO-based ceramics is closely linked to the polycrystalline microstructure. CCTO ceramics are of very high permittivity, the performance is more obvious especially in the condition of lower frequency, which happens on account of the famous Maxwell-Wagner effect.

It can be seen from the SEM photographs in **Figure 16** that the powder particles are homogeneous and dense, the particle sizes are less than 100 nm estimated from the figure. Crystalline

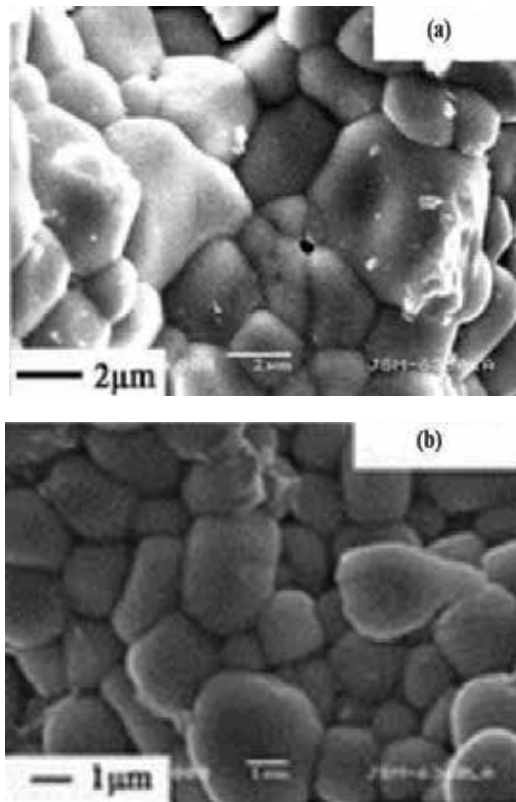


Figure 16. SEM images of CCTO-based ceramics sintered at 1120°C for 2 h. (a) $\text{CaCu}_3\text{Ti}_4\text{O}_{12}$; (b) $\text{CaCu}_3\text{Zr}_{0.05}\text{Ti}_{3.95}\text{O}_{12}$.

phase was obtained which can be confirmed from XRD and SEM photographs. The powder prepared by sol-gel process helped in the uniform mixing of all the elements in nanoscale, and corresponding nanocrystals were formed. From the SEM photographs, it is evident that prepared samples of $\text{CaCu}_3\text{Ti}_4\text{O}_{12}$ and $\text{CaCu}_3\text{Zr}_{0.05}\text{Ti}_{3.95}\text{O}_{12}$ are composed of many grain, the grain boundary effect can make a major contribution to the high dielectric constant of polycrystalline CCTO-based ceramics.

6.2. Optical properties of magnetic films

Iron-based semiconducting oxide magnetic nanoparticles, for instance spinel ferrites with general formula $\text{M}^{2+}(\text{Fe}^{3+})_2\text{O}_4$ (where $\text{M}^{2+} = \text{Mn}^{2+}, \text{Co}^{2+}, \text{Ni}^{2+}, \text{Cu}^{2+}, \text{Zn}^{2+}$, etc.), have become a prominent family in the magnetic materials due to their high electrical resistivity, high value of magnetic permeability, and use in advanced technologies like microwave devices, magnetic information storage devices, and biomedical applications [16]. Ferrites are one of the most effective photocatalysts for the ejection of toxic dyes from the industrial sewage.

Analytical grade $\text{Fe}(\text{NO}_3)_3 \cdot 9\text{H}_2\text{O}$, $(\text{Co}(\text{NO}_3)_2 \cdot 6\text{H}_2\text{O})$, $(\text{Mg}(\text{NO}_3)_2 \cdot 6\text{H}_2\text{O})$, and citric acid ($\text{C}_6\text{H}_8\text{O}_7$) were used as starting materials for the preparation of $\text{Co}_{(1-x)}\text{Mg}_x\text{Fe}_2\text{O}_4$ ($x = 0.0$,

0.3, 0.6, 0.9 and 1.0) ferrites. The molar ratio between metal nitrates and citric acid was adjusted to 1:2. After stoichiometric calculations and weighing, the appropriate quantity of all metal nitrates and citric acid were dissolved in 50 mL deionized water to form a mixed solution. A little quantity of ammonia was included dropwise to maintain the pH value at 7.0. The aqueous solution was heated at 95°C, stirred using a magnetic stirrer, and a viscous solution was obtained. With gel formation, the temperature was raised to 300°C which led to a self-sustaining combustion process followed by the formation of a loose powder. The powder was calcined at 600°C for 6 h with a heating rate of 8.5°C/min resulting in the formation of the final spinel structure samples. Energy band gaps of powder samples were determined using diffused reflection accessory attached with UV-Vis spectrophotometer.

UV-visible spectra were utilized to determine the band gap energies (E_g) of all the samples. Diffuse reflection spectra of Mg substituted CoFe_2O_4 powder samples were recorded as shown in **Figure 17**. It shows that the E_g values were decreased tremendously from 2.4 eV to 1.8 eV with Mg substitution increase that ended in the visible range of e.m. spectra [16].

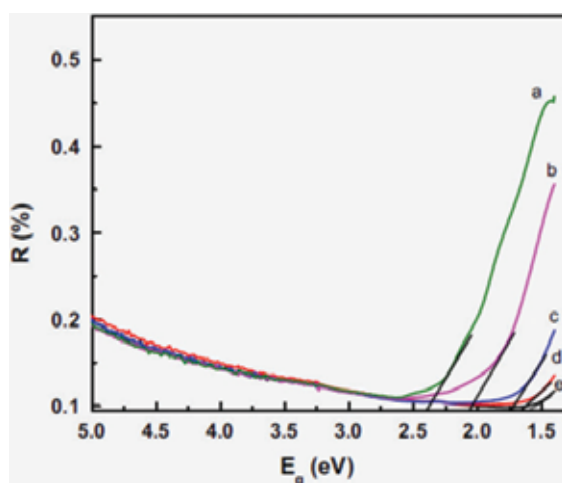


Figure 17. UV-visible diffuse reflectance spectra of $\text{Co}_{(1-x)}\text{Mg}_x\text{Fe}_2\text{O}_4$ (a) $x = 0.0$, (b) $x = 0.3$, (c) $x = 0.6$, (d) $x = 0.9$, and (e) $x = 1.0$.

7. Conclusion

The preparation methods of the thin films or powders and the heat treatment conditions have a crucial influence on the grain growth of the film. It affects not only the grain size of the film but also the surface morphology of the film, which affects the dielectric properties of the material. Microstructure has effects on the dielectric properties, optical properties, and magnetic properties of samples. Sol-gel method is a reasonable way to prepare function materials. Polycrystalline and nanocrystalline materials can be prepared by this process.

Author details

Chao-Qun Ye

Address all correspondence to: ycq1998@gmail.com

School of Biological and Chemical Engineering, Nanyang Institute of Technology, Nanyang, Henan, People's Republic of China

References

- [1] Bhushan, B. *Encyclopedia of Nanotechnology*, Dordrecht: Springer Nature; 2016. DOI: 10.1007/978-94-017-9780-1
- [2] Amiri S, Rahimi A. Hybrid nanocomposite coating by sol-gel method: A review. *Iranian Polymer Journal*. 2016;**25**:6. DOI: 10.1007/s13726-016-0440-x
- [3] Rahimi A. Inorganic and organometallic polymers: A review. *Iranian Polymer Journal*. 2004;**13**:149-164
- [4] Rabinovich EM, Klein LC. *Sol-Gel Technology for Thin Films, Fibers, Preforms, Electronics and Specialty Shapes*. New Jersey, USA: Noyes Publications; 1988. DOI: 10.1016/0025-5408(89)90225-0
- [5] Kessler VG, Spijksma GI, Seisenbaeva GA, Hakansson S, Blank DHA, Bouwmeester HJM. New insight in the role of modifying ligands in the sol-gel processing of metal alkoxide precursors: A possibility to approach new classes of materials. *Journal of Sol-Gel Science and Technology*. 2006;**40**:163-179. DOI: 10.1007/s10971-006-9209-6
- [6] Livage J, Henry M, Sanchez C. Sol-gel chemistry of transition metal oxides. *Progress in Solid State Chemistry*. 1988;**18**:259-341. DOI: 10.1016/0079-6786(88)90005-2
- [7] Liu C, Shaw L. Nanoparticulate materials and core/shell structures derived from wet chemistry methods. In: Bharat Bhushan, Editors. *Encyclopedia of Nanotechnology*. Dordrecht: Springer Netherlands; 2015. p. 1-21. DOI: 10.1007/978-94-007-6178-0_100906-1
- [8] Lee K, Guan BH, Zaid HM, Soleimani H, Ching DLC. Impact of pH on zinc oxide particle size by using sol-gel process. In: 4th International Conference on Fundamental and Applied Sciences (ICFAS 2016); 15-17 August 2016; Kuala Lumpur, MALAYSIA. New York: AIP; 2016. p. 1787
- [9] Kickelbick G. *Hybrid Materials: Synthesis, Characterization and Applications*. Weinheim: Wiley; 2007
- [10] Xiong J, Das SN, Shin B, Kar JP, Choi JH, Myoung JM. Biomimetic hierarchical ZnO structure with super hydrophobic and antireflective properties. *Journal of Colloid and Interface Science*. 2010;**350**:344-347. DOI: 10.1016/j.jcis.2010.06.053

- [11] Uhlmann DR. The future of sol-gel science and technology. *Journal of Sol-Gel Science and Technology*. 1997;**8**(1-3):1083-1091. DOI: 10.1007/BF02436988
- [12] Nguyet DTT, Duong NP, Satoh T, et al. Temperature-dependent magnetic properties of yttrium iron garnet nanoparticles prepared by citrate sol-gel. *Journal of Alloys and Compounds*. 2012;**541**(22):18-22. DOI: 10.1016/j.jallcom.2012.06.122
- [13] Kishimoto M, Minagawa M, Yanagihara H, et al. Synthesis and magnetic properties of platelet γ -Fe₂O₃ particles for medical applications using hysteresis-loss heating. *Journal of Magnetism and Magnetic Materials*. 2012;**324**(7):1285-1289. DOI: 10.1016/j.jmmm.2011.11.036
- [14] Pankove IJ, Aigrain P. Optical absorption of arsenic-doped degenerate germanium. *Physical Review*. 1962;**126**(3):956-962. DOI: 10.1103/PhysRev.126.956
- [15] Qun YC, Ding L. Dielectric properties of Zr-doped CCTO based ceramics prepared via sol-gel method. *Advanced Materials Research*. 2012;**528**:121-125. DOI: 10.4028/www.scientific.net/AMR.528.121
- [16] Assi H, Atiq S, Rammay SM, Alzayed NS, Saleem M, Riaz S, Naseem S. Substituted Mg-Co-nanoferrite: Recyclable magnetic photocatalyst for the reduction of methylene blue and degradation of toxic dyes. *Journal of Materials Science: Materials in Electronics*. 2017;**28**(2):2250-2256. DOI: 10.1007/s10854-016-5795-4

The Effect of Substituent on Molecules That Contain a Triple Bond Between Arsenic and Group 13 Elements: Theoretical Designs and Characterizations

Jia-Syun Lu, Ming-Chung Yang, Shih-Hao Su and Ming-Der Su

Additional information is available at the end of the chapter

<http://dx.doi.org/10.5772/intechopen.69586>

Abstract

The effect of substitution on the potential energy surfaces of $RE_{13}\equiv AsR$ (E_{13} = group 13 elements; $R = F, OH, H, CH_3,$ and SiH_3) is determined using density functional theory (M06-2X/Def2-TZVP,B3PW91/Def2-TZVP, and B3LYP/LANL2DZ+dp). The computational studies demonstrate that all triply bonded $RE_{13}\equiv AsR$ species prefer to adopt a bent geometry that is consistent with the valence electron model. The theoretical studies also demonstrate that $RE_{13}\equiv AsR$ molecules with smaller substituents are kinetically unstable, with respect to the intramolecular rearrangements. However, triply bonded $R'E_{13}\equiv AsR'$ species with bulkier substituents ($R' = SiMe(Si^tBu_3)_2,$ $Si^iPrDis_2,$ and NHC) are found to occupy the lowest minimum on the singlet potential energy surface, and they are both kinetically and thermodynamically stable. That is to say, the electronic and steric effects of bulky substituents play an important role in making molecules that feature an $E_{13}\equiv As$ triple bond as viable synthetic target.

Keywords: arsenic, group 13 elements, triple bond, density functional theory, multiple bond

1. Introduction

In the past two decades, studies that have been performed by many synthetic chemists have successfully synthesized and characterized homonuclear heavy alkyne-like $RE_{14}\equiv E_{14}R$ ($E_{14} = Si, Ge, Sn,$ and Pb) molecules [1–23]. Recently, heteronuclear ethyne-like compounds, $RC\equiv E_{14}R,$ have also been experimentally studied [24, 25, 26] and theoretically predicted [27, 28, 29].

However, from the valence electron viewpoint, $RE_{13}\equiv E_{15}R$ (E_{13} = group 13 elements and E_{15} = group 15 elements) is isoelectronic with the $RE_{14}\equiv E_{14}R$ species. Therefore, triply bonded $RE_{13}\equiv E_{15}R$ is the next synthetic challenge. To the best of the authors' knowledge, only R_2BN molecules that contain a $B\equiv N$ triple bond have been experimentally demonstrated to exist [30–40].

2. Theoretical methods

This chapter reports the possible existence of triply bonded $RE_{13}\equiv AsR$ molecules, from the viewpoint of the effect of substituents, using density functional theories (DFT): M06-2X/Def2-TZVP, B3PW91/Def2-TZVP, and B3LYP/LANL2DZ+dp for small substituents and B3LYP/LANL2DZ+dp//RHF/3-21G* for large substituents. It is hoped that this theoretical study will stimulate further research into the synthetic chemistry of triply bonded $RE_{13}\equiv AsR$ species.

3. Results and discussion

3.1. Small ligands on substituted $RE_{13}\equiv AsR$

The effect of the electronegativity of six types of small substituents ($R = F, OH, H, CH_3,$ and SiH_3) on the stability of the triply bonded $RE_{13}\equiv AsR$ molecules is determined using the three DFT methods. The molecular properties (geometrical parameters, singlet-triplet energy splitting, natural charge densities, binding energies (BE), and the Wiberg Bond Index (WBI)) are all listed in **Tables 1–5**. The reaction profiles for the unimolecular rearrangement reactions for the $RE_{13}\equiv AsR$ compounds are also given in **Figures 1–5**.

There are three noteworthy features of **Tables 1–5** and **Figures 1–5**.

1. From the tables, the three DFT calculations show that the triple bond distances (\AA) for $B\equiv As$, $Al\equiv As$, $Ga\equiv As$, $In\equiv As$, and $Tl\equiv As$ are estimated to be 1.835–1.908 (**Table 1**), 2.218–2.358 (**Table 2**), 2.239–2.364 (**Table 3**), 2.404–2.546 (**Table 4**), and 2.426–2.570 (**Table 5**). As previously mentioned, no experimental values for these triple bond lengths have been reported, so these computational data are a prediction.
2. In **Tables 1–5**, these DFT computations all demonstrate that the triply bonded $RE_{13}\equiv AsR$ molecules favor a bent structure, rather than a linear structure. This is explained by the bonding model, as shown in **Figure 6**. Because there is a significant difference between the sizes of the valence s and p atomic orbitals in the As atom, hybrid orbitals between the valence s and p orbitals are not easily formed (the so-called orbital non-hybridization effect or the inert s -pair effect) [41–44]. Therefore, $RE_{13}\equiv AsR$ molecules that have a heavier As center are predicted to favor a bent angle $\angle E_{13}-As-R$ (close to 90°). The DFT computational data that are shown in **Tables 1–5** confirm this prediction.

R	F	OH	H	CH3	SiH3
B≡As (Å)	1.901	1.892	1.837	1.839	1.814
	(1.898)	(1.888)	(1.835)	(1.839)	(1.820)
	[1.908]	[1.906]	[1.849]	[1.861]	[1.839]
∠R–B–As (°)	177.2	179.5	178.1	175.1	175.3
	(177.8)	(179.5)	(174.6)	(175.1)	(172.4)
	[177.0]	[179.1]	[177.5]	[174.3]	[174.8]
∠B–As–R (°)	93.03	92.73	81.22	94.69	68.92
	(92.71)	(92.21)	(89.39)	(94.69)	(68.98)
	[92.39]	[92.95]	[78.37]	[96.15]	[72.25]
∠R–B–As–R (°)	180.0	179.8	180.0	179.8	148.7
	(180.0)	(180.0)	(180.0)	(179.8)	(180.0)
	[180.0]	[176.2]	[179.0]	[176.3]	[179.4]
Q_B¹	0.354	0.184	–0.017	–0.007	0.037
	(0.262)	(0.108)	(–0.028)	(–0.057)	(0.036)
	[0.232]	[0.070]	[–0.106]	[–0.160]	[–0.407]
Q_{As}²	0.243	0.080	–0.152	–0.073	–0.085
	(0.255)	(0.097)	(–0.134)	(–0.040)	(–0.017)
	[0.238]	[0.086]	[0.034]	[–0.035]	[0.030]
BE (kcal mol^{–1})³	63.56	56.97	114.7	94.39	79.90
	(63.34)	(60.28)	(120.1)	(137.6)	(74.75)
	[57.45]	[55.28]	[113.7]	[132.6]	[73.79]
WBI⁴	1.800	1.830	2.141	2.027	2.204
	(1.813)	(1.823)	(2.158)	(2.029)	(2.168)
	[1.835]	[1.836]	[2.135]	[2.041]	[2.185]

1 The natural charge density on the B atom.

2 The natural charge density on the As atom.

3 BE = E(triplet state for R–B) + E(triplet state for R–As) – E(singlet state for RB≡AsR).

4 The Wiberg bond index (WBI) for the B–As bond: see [45, 46].

Table 1. The main geometrical parameters, the singlet-triplet energy splitting (ΔE_{ST}), the natural charge densities (Q_B and Q_{As}), the binding energies (BE), and the Wiberg Bond Index (WBI) for RB≡AsR using the M06-2X/Def2-TZVP, B3PW91/Def2-TZVP (in round brackets), and B3LYP/LANL2DZ+dp (in square brackets) levels of theory.

R	F	OH	H	CH3	SiH3
Al≡As (Å)	2.327	2.321	2.218	2.253	2.227
	(2.325)	(2.323)	(2.221)	(2.256)	(2.236)
	[2.355]	[2.358]	[2.269]	[2.285]	[2.292]
∠R-Al-As (°)	178.6	174.4	172.5	172.8	168.4
	(179.5)	(174.3)	(172.2)	(172.0)	(167.3)
	[178.8]	[173.9]	[177.5]	[171.1]	[173.7]
∠Al-As-R (°)	93.07	91.08	66.95	98.77	91.93
	(93.51)	(92.45)	(67.45)	(100.7)	(95.83)
	[90.64]	[90.97]	[75.97]	[100.5]	[90.36]
∠R-Al-As-R (°)	180.0	180.0	180.0	174.2	174.7
	(179.8)	(178.5)	(179.6)	(176.8)	(175.7)
	[180.0]	[179.0]	[178.0]	[174.5]	[176.8]
Q_{Al}^1	0.555	0.4574	0.2401	0.293	0.291
	(0.530)	(0.443)	(0.234)	(0.280)	(0.313)
	[0.784]	[0.540]	[0.504]	[0.353]	[0.245]
Q_{As}^2	0.158	0.015	-0.276	-0.170	-0.262
	(0.142)	(-0.007)	(-0.246)	(-0.156)	(-0.209)
	[0.056]	[-0.032]	[-0.209]	[-0.284]	[-0.290]
BE (kcal mol ⁻¹) ³	33.90	28.23	71.86	56.47	53.22
	(38.90)	(31.24)	(77.42)	(60.57)	(54.98)
	[33.89]	[25.68]	[69.27]	[52.63]	[67.74]
WBI ⁴	1.532	1.523	1.714	1.649	1.647
	(1.567)	(1.553)	(1.742)	(1.679)	(1.675)
	[1.557]	[1.545]	[1.714]	[1.690]	[1.550]

1 The natural charge density on the Al atom.

2 The natural charge density on the As atom.

3 BE = E(triplet state for R-Al) + E(triplet state for R-As) - E(singlet state for RAl=AsR).

4 The Wiberg bond index (WBI) for the Al-As bond: see [45, 46].

Table 2. The main geometrical parameters, the singlet-triplet energy splitting (ΔE_{ST}), the natural charge densities (Q_{Al} and Q_{As}), the binding energies (BE), and the Wiberg Bond Index (WBI) for RAl=AsR using the M06-2X/Def2-TZVP, B3PW91/Def2-TZVP (in round brackets), and B3LYP/LANL2DZ+dp (in square brackets) levels of theory.

3. In terms of the stability of the $RE_{13}\equiv AsR$ species, the three DFT computations are used to study the energy surfaces for the $RE_{13}\equiv AsR$ systems, and the theoretical results are shown in **Figures 1–5**. These figures show three local minima (i.e., $R_2E_{13}=As$, $RE_{13}\equiv AsR$, and $E_{13}=AsR_2$) and two saddle points that connect them. It is seen that regardless of the type of small substituent, triply bonded $RE_{13}\equiv AsR$ molecules are unstable on the potential energy surfaces, so they easily undergo a 1,2-migration reaction to produce the most stable doubly bonded isomers. There is strong theoretical evidence that there is no possibility of observing triply bonded $RE_{13}\equiv AsR$ compounds in transient intermediates or even in a matrix.

3.2. Large ligands on substituted $R'E_{13}\equiv AsR'$

Bulky substituents are used to determine the possible existence of triply bonded $R'E_{13}\equiv AsR'$ ($R' = SiMe(Si^iBu_3)_2$, Si^iPrDis_2 , and NHC; (Scheme 1)) molecules. The molecular properties, the natural bond orbital (NBO) [45, 46], and the natural resonance theory (NRT) [47, 48, 49] analyses of $R'E_{13}\equiv AsR'$ are computed at the B3LYP/LANL2DZ+dp//RHF/3-21G* level of theory, and the results are shown in **Tables 6, 7** ($R'B\equiv AsR'$), **8, 9** ($R'Al\equiv AsR'$), **10, 11** ($R'Ga\equiv AsR'$), **12, 13** ($R'In\equiv AsR'$), and **14 and 15** ($R'Tl\equiv AsR'$).

R	F	OH	H	CH3	SiH3
$Ga\equiv As$ (Å)	2.261 (2.319) [2.364]	2.339 (2.314) [2.364]	2.239 (2.224) [2.263]	2.330 (2.243) [2.285]	2.243 (2.242) [2.270]
$\angle R-Ga-As$ (°)	179.5 (178.5) [179.3]	173.2 (177.4) [176.2]	176.2 (178.6) [179.1]	169.9 (173.6) [171.1]	168.5 (179.1) [179.2]
$\angle Ga-As-R$ (°)	92.80 (94.36) [91.81]	93.16 (94.54) [93.68]	76.00 (79.18) [80.30]	103.0 (99.37) [100.4]	93.43 (73.64) [76.86]
$\angle R-Ga-As-R$ (°)	180.0 (180.0) [173.1]	175.6 (178.1) [177.4]	179.6 (179.1) [178.2]	175.7 (178.4) [174.5]	173.5 (175.6) [178.1]
Q_{Ga}^1	0.7067 (0.554) [0.706]	0.592 (0.410) [0.474]	0.310 (0.215) [0.435]	0.4451 (0.260) [0.295]	0.3352 (0.241) [0.174]
Q_{As}^2	0.0899 (0.154) [0.133]	-0.047 (0.023) [0.006]	-0.374 (-0.262) [-0.184]	-0.256 (-0.151) [-0.246]	-0.3697 (-0.222) [-0.284]
BE (kcal mol ⁻¹) ³	28.56 (30.61) [27.65]	23.82 (25.96) [90.75]	67.79 (71.91) [65.14]	53.57 (58.12) [50.32]	49.26 (51.77) [62.24]
WBI^4	1.476 (1.486) [1.487]	1.498 (1.503) [1.495]	1.691 (1.717) [1.707]	1.648 (1.652) [1.668]	1.646 (1.596) [1.615]

1 The natural charge density on the Ga atom.

2 The natural charge density on the As atom.

3 $BE = E(\text{triplet state for } R-Ga) + E(\text{triplet state for } R-As) - E(\text{singlet state for } RGA\equiv AsR)$.

4 The Wiberg bond index (WBI) for the Ga-As bond: see [45, 46].

Table 3. The main geometrical parameters, the singlet-triplet energy splitting (ΔE_{st}), the natural charge densities (Q_{Ga} and Q_{As}), the binding energies (BE), and the Wiberg Bond Index (WBI) for $RGA\equiv AsR$ using the M06-2X/Def2-TZVP, B3PW91/Def2-TZVP (in round brackets), and B3LYP/LANL2DZ+dp (in square brackets) levels of theory.

R	F	OH	H	CH3	SiH3
In≡As (Å)	2.511	2.512	2.412	2.431	2.411
	(2.495)	(2.497)	(2.399)	(2.418)	(2.404)
	[2.535]	[2.546]	[2.432]	[2.459]	[2.444]
∠R-In-As (°)	179.9	178.8	179.3	173.6	170.9
	(179.9)	(176.9)	(179.9)	(173.3)	(168.4)
	[177.8]	[175.2]	[179.8]	[172.5]	[167.4]
∠In-As-R (°)	92.32	95.31	81.43	99.72	93.85
	(93.86)	(96.11)	(82.67)	(100.4)	(99.59)
	[91.08]	[94.22]	[82.28]	[100.5]	[102.0]
∠R-In-As-R (°)	180.0	169.3	177.3	174.7	177.1
	(180.0)	(166.8)	(175.9)	(173.0)	(177.4)
	[180.0]	[163.8]	[179.6]	[179.8]	[178.2]
Q_{In}¹	1.288	1.233	1.012	1.144	0.8840
	(1.196)	(1.123)	(0.912)	(1.037)	(0.7881)
	[1.343]	[1.287]	[1.076]	[1.121]	[0.9682]
Q_{As}²	0.138	0.036	-0.624	-0.388	-0.767
	(0.146)	(0.047)	(-0.571)	(-0.335)	(-0.703)
	[0.077]	[-0.005]	[-0.591]	[-0.367]	[-0.748]
BE (kcal mol⁻¹)³	22.14	18.30	55.63	53.87	57.82
	(19.72)	(20.13)	(60.95)	(50.24)	(57.34)
	[24.06]	[16.22]	[57.18]	[53.36]	[54.39]
WBI⁴	1.536	1.551	1.773	1.719	1.726
	(1.546)	(1.554)	(1.798)	(1.738)	(1.749)
	[1.572]	[1.562]	[1.780]	[1.729]	[1.710]

1 The natural charge density on the In atom.

2 The natural charge density on the As atom.

3 BE = E(triplet state for R-In) + E(triplet state for R-As) - E(singlet state for RIn≡AsR).

4 The Wiberg bond index (WBI) for the In-As bond, see [45, 46].

Table 4. The main geometrical parameters, the singlet-triplet energy splitting (ΔE_{ST}), the natural charge densities (Q_{In} and Q_{As}), the binding energies (BE), and the Wiberg Bond Index (WBI) for RIn≡AsR using the M06-2X/Def2-TZVP, B3PW91/Def2-TZVP (in round brackets), and B3LYP/LANL2DZ+dp (in square brackets) levels of theory.

R	F	OH	H	CH3	SiH3
$\Pi \equiv \text{As}$ (Å)	2.535	2.531	2.426	2.446	2.431
	(2.533)	(2.536)	(2.428)	(2.450)	(2.432)
	[2.558]	[2.570]	[2.429]	[2.459]	[2.433]
$\angle \text{R}-\Pi-\text{As}$ (°)	179.9	178.2	180.0	176.6	176.5
	(179.9)	(175.8)	(179.5)	(175.0)	(173.4)
	[179.2]	[177.0]	[179.5]	[173.8]	[177.7]
$\angle \Pi-\text{As}-\text{R}$ (°)	91.49	94.88	84.22	97.14	90.08
	(93.64)	(96.73)	(84.51)	(99.33)	(93.68)
	[92.21]	[96.20]	[84.07]	[99.33]	[89.37]
$\angle \text{R}-\Pi-\text{As}-\text{R}$ (°)	180.0	175.5	173.0	178.0	179.2
	(179.3)	(176.7)	(178.1)	(178.2)	(178.5)
	[180.0]	[172.9]	[179.6]	[177.6]	[177.2]
Q_{Π}^1	0.736	0.640	0.3883	0.482	0.3051
	(0.656)	(0.538)	(0.352)	(0.428)	(0.382)
	[0.817]	[0.549]	[0.472]	[0.361]	[0.244]
Q_{As}^2	0.190	0.035	-0.4169	-0.251	-0.3290
	(0.163)	(0.013)	(-0.351)	(-0.208)	(-0.291)
	[0.139]	[0.021]	[-0.204]	[-0.273]	[-0.336]
BE (kcal mol ⁻¹) ³	13.48	10.36	50.28	38.25	29.93
	(16.73)	(13.88)	(55.13)	(43.44)	(30.60)
	[15.13]	[8.720]	[49.40]	[37.22]	[45.10]
WBI^4	1.109	1.148	1.456	1.382	1.409
	(1.143)	(1.174)	(1.492)	(1.416)	(1.407)
	[1.168]	[1.175]	[1.484]	[1.413]	[1.411]

1 The natural charge density on the Π atom.

2 The natural charge density on the As atom.

3 $\text{BE} = E(\text{triplet state for R}-\Pi) + E(\text{triplet state for R}-\text{As}) - E(\text{singlet state for R}\Pi \equiv \text{AsR})$.

4 The Wiberg bond index (WBI) for the Π -As bond, see [45, 46].

Table 5. The main geometrical parameters, the singlet-triplet energy splitting (ΔE_{ST}), the natural charge densities (Q_{Π} and Q_{As}), the binding energies (BE), and the Wiberg Bond Index (WBI) for $\text{R}\Pi \equiv \text{AsR}$ using the M06-2X/Def2-TZVP, B3PW91/Def2-TZVP (in round brackets), and B3LYP/LANL2DZ+dp (in square brackets) levels of theory.

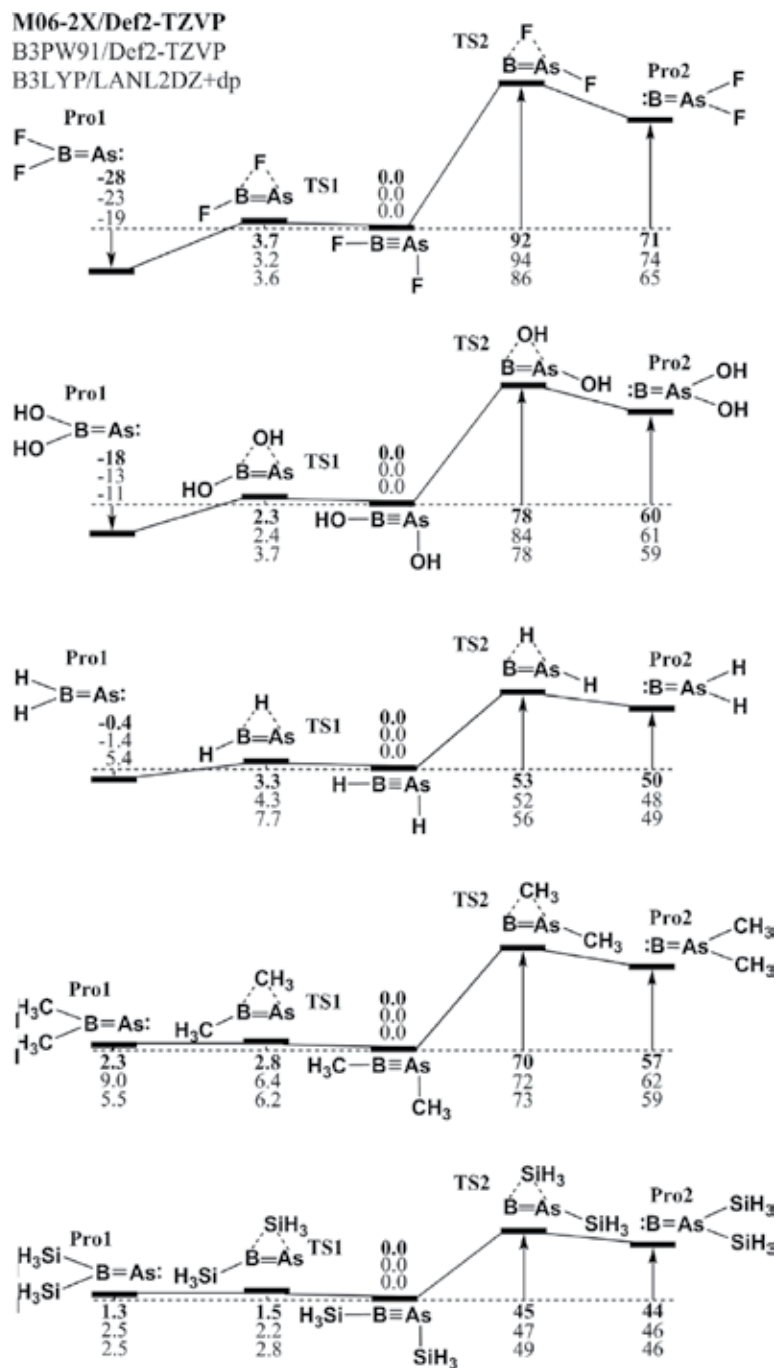


Figure 1. The relative Gibbs free energies for $RB \equiv AsR$ ($R = F, OH, H, CH_3,$ and SiH_3). All energies are in kcal/mol and are calculated at the M06-2X/Def2-TZVP, B3PW91/Def2-TZVP, and B3LYP/LANL2DZ+dp levels of theory.

M06-2X/Def2-TZVP
 B3PW91/Def2-TZVP
 B3LYP/LANL2DZ+dp

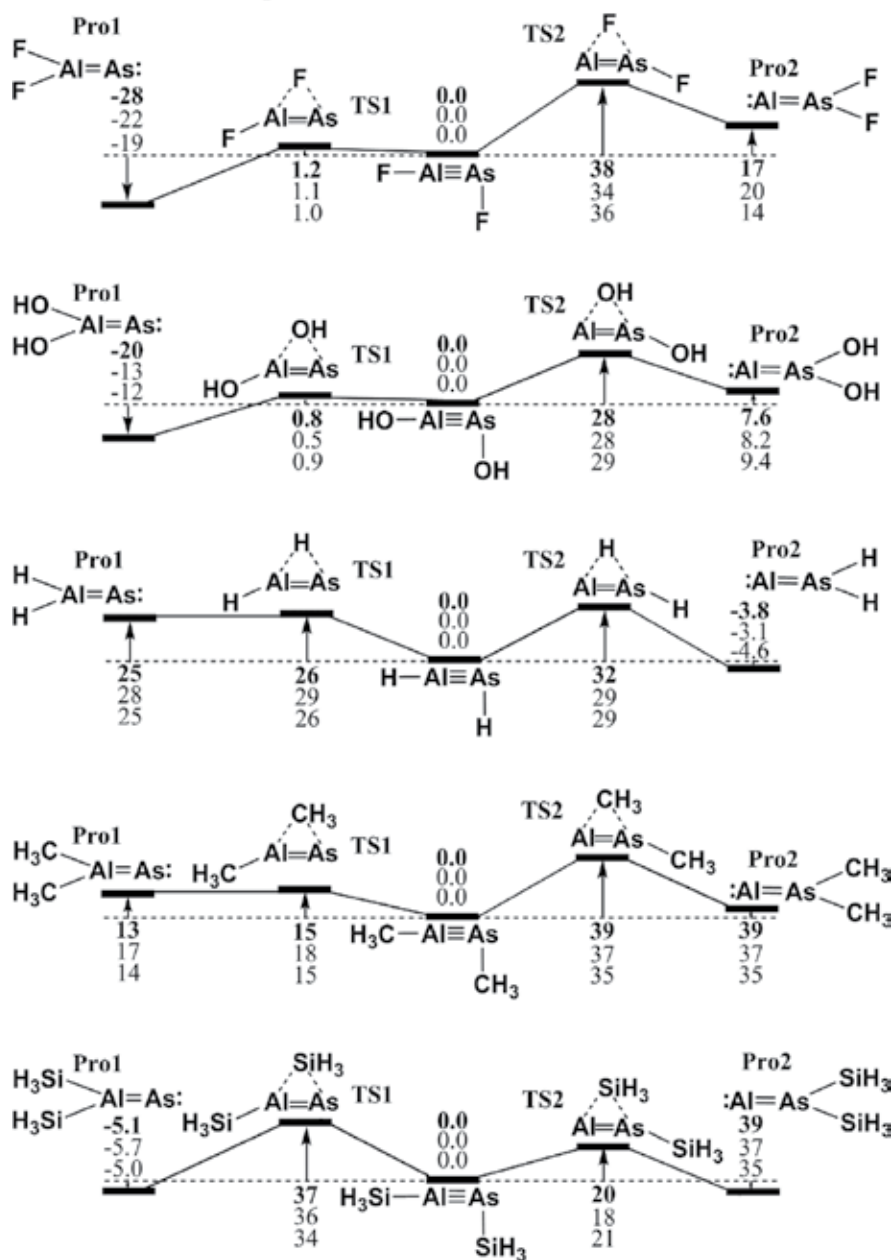


Figure 2. The relative Gibbs free energies for $RAl=AsR$ ($R = F, OH, H, CH_3$, and SiH_3). All energies are in kcal/mol and are calculated at the M06-2X/Def2-TZVP, B3PW91/Def2-TZVP, and B3LYP/LANL2DZ+dp levels of theory.

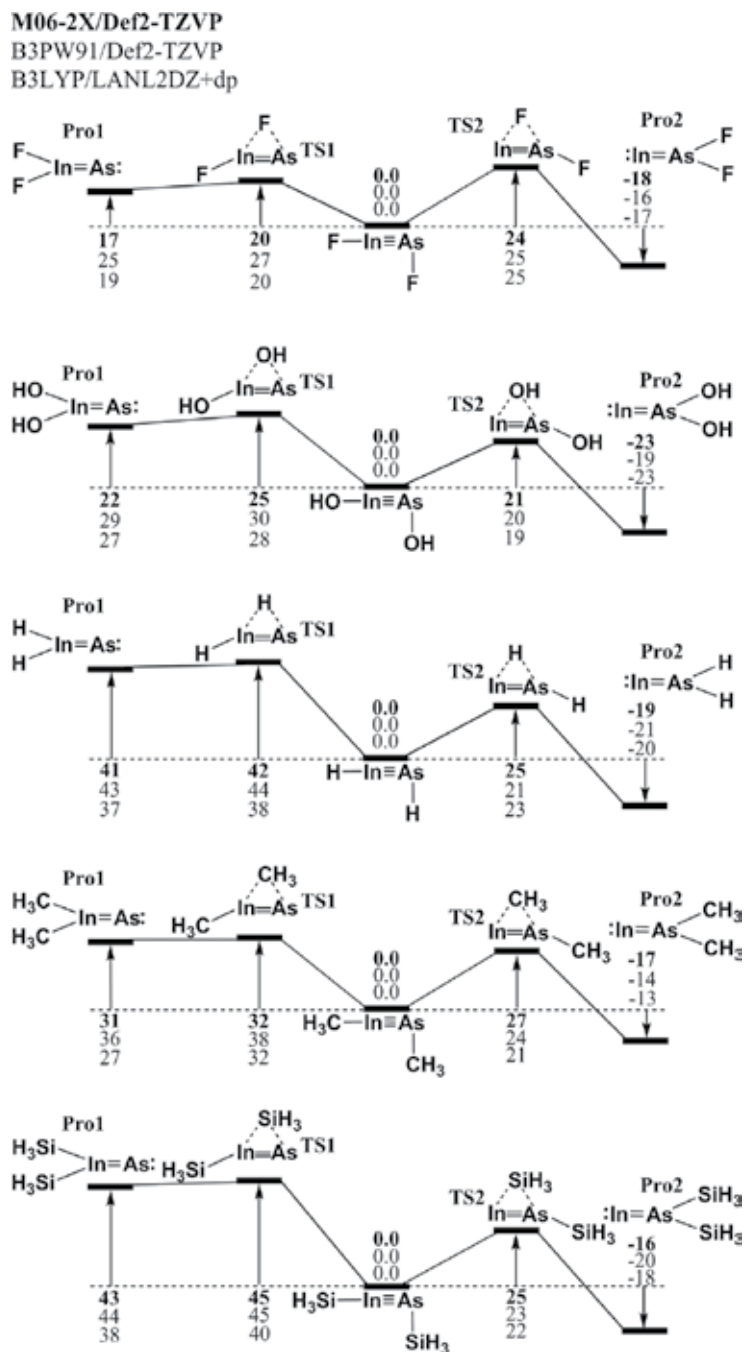


Figure 4. The relative Gibbs free energies for $R\text{In}=\text{As}R$ ($R = \text{F}, \text{OH}, \text{H}, \text{CH}_3, \text{and SiH}_3$). All energies are in kcal/mol and are calculated at the M06-2X/Def2-TZVP, B3PW91/Def2-TZVP, and B3LYP/LANL2DZ+dp levels of theory.

M06-2X/Def2-TZVP
 B3PW91/Def2-TZVP
 B3LYP/LANL2DZ+dp

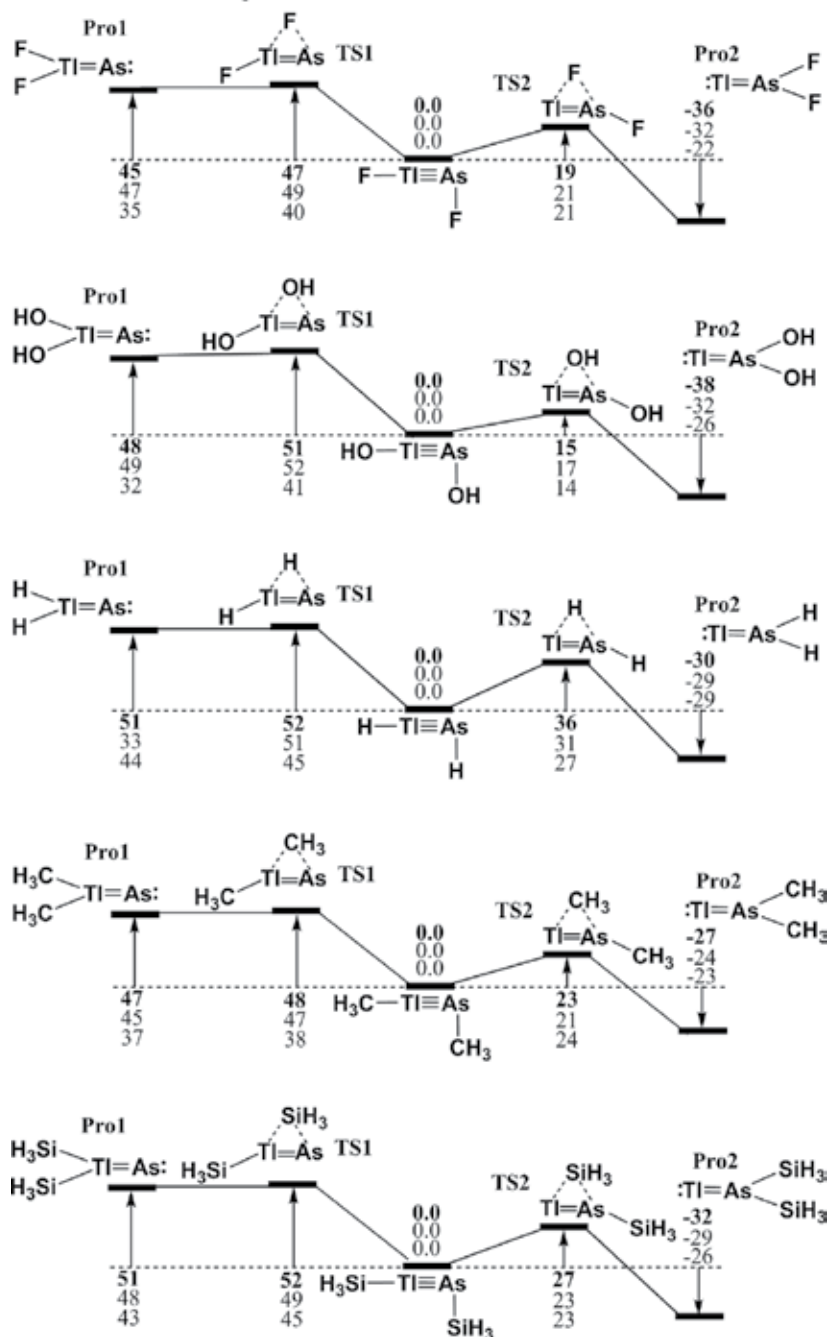
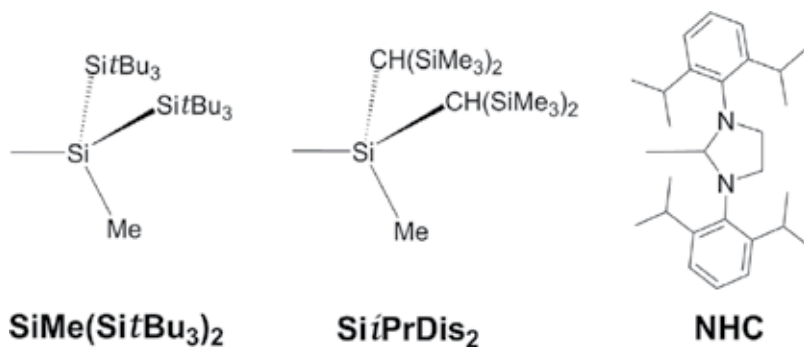


Figure 5. The relative Gibbs free energies for $RTl=AsR$ ($R = F, OH, H, CH_3$, and SiH_3). All energies are in kcal/mol and are calculated at the M06-2X/Def2-TZVP, B3PW91/Def2-TZVP, and B3LYP/LANL2DZ+dp levels of theory.

The results in **Tables 6–15** allow three conclusions to be drawn.

1. The calculations that are shown in **Tables 6 (B), 8 (Al), 10 (Ga), 12 (In), and 14 (Tl)** show that the computed $E_{13}\equiv\text{As}$ triple bond distances (\AA) for these bulkily substituted species ($R'E_{13}\equiv\text{As}R'$) are estimated to be 1.821–1.837 ($\text{B}\equiv\text{As}$), 2.257–2.307 ($\text{Al}\equiv\text{As}$), 2.252–2.316 ($\text{Ga}\equiv\text{As}$), 2.430–2.482 ($\text{In}\equiv\text{As}$), and 2.565–2.653 ($\text{Tl}\equiv\text{As}$). The values for the WBO that are shown in **Tables 6–10** (for bulky ligands) are obviously greater than those that are shown in **Tables 1–5** (for smaller ligands). These WBO values show that bulkier substituents increase the bond order for the $E_{13}\equiv\text{As}$ triple bond length.
2. Similarly to the results for small ligands, the computational results show that $R'E_{13}\equiv\text{As}R'$ species that feature large substituents all adopt a bent conformation. This phenomenon is explained by bonding model (II), which is shown in **Figure 6**.
3. The NBO values that are shown in **Tables 7 (B=As), 9 (Al=As), 11 (Ga=As), 13 (In=As), and 15 (Tl=As)** show that the acetylene-like $R'E_{13}\equiv\text{As}R'$ compounds feature a weak triple bond. For example, the B3LYP/LANL2DZ+dp data for the NBO analyses of the $\text{B}\equiv\text{As}$ π bonding in ($\text{Si}i\text{PrDis}_2\text{-B}\equiv\text{As-Si}i\text{PrDis}_2$), which shows that $\text{NBO}(\text{B}\equiv\text{As}) = 0.5880(2s2p^{99.99})\text{B} + 0.8089(4s4p^{1.00})\text{As}$, provide strong evidence that the predominant bonding interaction between the $\text{B-Si}i\text{PrDis}_2$ and the $\text{As-Si}i\text{PrDis}_2$ units results from $2p(\text{B}) \leftarrow 4p(\text{As})$ donation, whereby boron's electron deficiency and π bond polarity are partially balanced by the donation of the arsenic lone pair into the empty boron p orbital to develop a hybrid π bond. The polarization analyses using the NBO model again demonstrate the presence of the $\text{B}\equiv\text{As}$ π bonding orbital, 34.58% of which is composed of natural B orbitals and 65.42% of which is natural As orbitals. **Table 7** also shows that the $\text{B}\equiv\text{As}$ triple bond in ($\text{Si}i\text{PrDis}_2\text{-B}\equiv\text{As-Si}i\text{PrDis}_2$) has a shorter single bond character (6.04%) and a shorter triple bond character (36.74%), but a greater double bond character (57.2%), because the ionic part of the NRT bond order (0.53) is shorter than its covalent part (1.71). The same theoretical observations are also seen for the other two differently substituted $R'B\equiv\text{As}R'$ compounds, as shown in **Table 7**, and in the data for the other $R'E_{13}\equiv\text{Bi}R'$ compounds that is shown in **Tables 9 (Al), 11 (Ga), 13 (In), and 15 (Tl)**. These computational data demonstrate that these $R'E_{13}\equiv\text{As}R'$ molecules have a weak $E_{13}\equiv\text{As}$ triple bond.



Scheme 1. Three bulky ligands: $\text{SiMe}(\text{Si}^t\text{Bu}_3)_2$, $\text{Si}^i\text{PrDis}_2$, and N-heterocyclic carbene.

R'	SiMe(Si <i>t</i> Bu ₃) ₂	Si <i>i</i> PrDis ₂	NHC
B≡As (Å)	1.837	1.821	1.819
∠R'-B-As (°)	177.2	172.9	174.5
∠B-As-R' (°)	128.2	121.6	111.2
∠R'-B-As-R' (°)	179.6	177.4	171.5
Q _B ¹	-0.280	-0.397	-0.205
Q _{As} ²	-0.228	-0.134	0.061
ΔE _{ST} (kcal mol ⁻¹) ³	94.42	75.22	83.64
Wiberg BO ⁴	2.327	2.395	2.254

1 The natural charge density on the central B atom.

2 The natural charge density on the central As atom.

3 BE = E (triplet state for B-R') + E (triplet state for As-R') - E (singlet state for R'B≡AsR').

4 The Wiberg bond index (WBI) for the B-As bond.

5 ΔH₁ = E (:B=AsR'₂) - E (R'B≡AsR'); see Scheme 2.

6 ΔH₂ = E (R'₂B=As:) - E (R'B≡AsR'); see Scheme 2.

Table 6. The geometrical parameters, natural charge densities (Q_B and Q_{As}), Binding Energies (BE), the HOMO-LUMO Energy Gaps, the Wiberg Bond Index (WBI), and some reaction enthalpies for R'B≡AsR' at the B3LYP/LANL2DZ+dp//RHF/3-21G* Level of Theory.

R'B≡AsR'	WBI	NBO analysis			NRT analysis	
		Occupancy	hybridization	Polarization	total/covalent/ ionic	Resonance weight
R' = SiMe(Si <i>t</i> Bu ₃) ₂	2.31	σ = 1.98	σ : 0.6627 B (sp ^{1.46}) + 0.7489 As (sp ^{1.07})	43.91% (B) 56.09% (As)	2.35/1.66/0.69	B-As: 5.68% B=As: 60.70% B≡As: 33.62%
		π = 1.94	π : 0.5941 B (sp ^{1.00}) + 0.8044 As (sp ^{99.99})	35.29% (B) 64.71% (As)		
R' = Si <i>i</i> PrDis ₂	2.27	σ = 1.98	σ : 0.6630 B (sp ^{1.54}) + 0.7486 As (sp ^{1.22})	43.96% (B) 56.04% (As)	2.24/1.71/0.53	B-As: 6.04% B=As: 57.2% B≡As: 36.74%
		π = 1.94	π : 0.5880 B (sp ^{99.99}) + 0.8089 As (sp ^{99.99})	34.58% (B) 65.42% (As)		
R' = NHC	2.26	σ = 1.98	σ : 0.6918 B (sp ^{0.90}) + 0.7221 As (sp ^{2.66})	47.86% (B) 52.14% (As)	2.23/1.52/0.71	B-As: 7.05% B=As: 69.13% B≡As: 23.82%
		π = 1.94	π : 0.5899 B (sp ^{99.99}) + 0.8075 As (sp ^{99.99})	34.80% (B) 65.20% (As)		

Table 7. Selected results for the natural bond orbital (NBO) and natural resonance theory (NRT) analyses at the B3LYP/LANL2DZ+dp level of theory for R'B≡AsR' compounds that have large substituents.

R'	SiMe(Si ^t Bu ₃) ₂	Si ⁱ PrDis ₂	NHC
Al=As (Å)	2.285	2.257	2.307
∠R'-Al-As (°)	179.4	176.0	174.5
∠Al-As-R' (°)	116.4	118.7	113.0
∠R'-Al-As-R' (°)	176.1	170.6	176.4
Q _{Al} ¹	0.3771	0.3120	0.4392
Q _{As} ²	-0.5579	-0.4907	-0.3144
ΔE _{ST} (kcal mol ⁻¹) ³	44.64	54.23	34.53
Wiberg BO ⁴	2.171	2.184	2.185

1 The natural charge density on the central Al atom.

2 The natural charge density on the central As atom.

3 BE = E(triplet state for Al-R') + E(triplet state for As-R') - E(singlet state for R'Al=AsR').

4 The Wiberg bond index (WBI) for the Al-As bond.

5 ΔH₁ = E(:Al=AsR'₂) - E(R'Al=AsR'); see Scheme 2.

6 ΔH₂ = E(R'₂Al=As) - E(R'Al=AsR'); see Scheme 2.

Table 8. The geometrical parameters, natural charge densities (Q_{Al} and Q_{As}), binding energies (BE), the HOMO-LUMO energy gaps, the Wiberg Bond Index (WBI), and some reaction enthalpies for R'Al=AsR' at the B3LYP/LANL2DZ+dp//RHF/3-21G* level of theory.

R'Al=AsR'	WBI	NBO analysis		NRT analysis		
		Occupancy	hybridization	Polarization	total/covalent/ ionic	Resonance weight
R' = SiMe(Si ^t Bu ₃) ₂	2.21	σ = 1.92	σ : 0.5080 Al (sp ^{1.59}) + 0.8614 As (sp ^{1.14})	25.81% (Al) 74.19% (As)	2.24/1.66/0.58	Al-As : 6.51% Al=As : 70.32% Al≡As : 23.17%
		π = 1.92	π : 0.4437 Al (sp ^{99.99}) + 0.8962 As (sp ^{99.99})	19.69% (Al) 80.31% (As)		
R' = Si ⁱ PrDis ₂	2.29	σ = 1.92	σ : 0.4956 Al (sp ^{1.84}) + 0.8685 As (sp ^{1.06})	24.57% (Al) 75.43% (As)	2.27/1.73/0.54	Al-As: 4.52% Al≡As : 57.55% Al=As : 37.93%
		π = 1.91	π : 0.4383 Al (sp ^{99.99}) + 0.8988 As (sp ^{99.99})	19.21% (Al) 80.79% (As)		
R' = NHC	2.36	σ = 1.87	σ : 0.5834 Al (sp ^{0.99}) + 0.8122 As (sp ^{10.87})	34.04% (Al) 65.96% (As)	2.30/1.59/0.71	Al-As : 6.61% Al=As : 74.90% Al≡As : 18.49%
		π = 1.94	π : 0.4408 Al (sp ^{90.78}) + 0.8976 As (sp ^{99.99})	19.43% (Al) 80.57% (As)		

Table 9. Selected results for the natural bond orbital (NBO) and natural resonance theory (NRT) analyses at the B3LYP/LANL2DZ+dp level of theory for R'Al=AsR' compounds that have large substituents.

R'Ga≡AsR'	WBI	NBO analysis			NRT analysis	
		Occupancy	Hybridization	Polarization	total/covalent/ ionic	Resonance weight
R' = SiMe(Si <i>t</i> Bu ₃) ₂	2.19	σ = 1.90	σ : 0.5320 Ga (sp ^{1.52}) + 0.8468 As (sp ^{1.32})	28.30% (Ga) 71.70% (As)	2.27/1.62/0.65	Ga-As : 4.72% Ga=As : 56.61% Ga=As : 38.67%
		π = 1.93	π : 0.4467 Ga (sp ^{99.99}) + 0.8947 As (sp ^{99.99})	19.95% (Ga) 80.05% (As)		
R' = Si <i>i</i> PrDis ₂	2.25	σ = 1.91	σ : 0.5386 Ga (sp ^{1.49}) + 0.8426 As (sp ^{1.46})	29.01% (Ga) 70.99% (As)	2.31/1.64/0.67	Ga-As : 7.03% Ga=As : 68.13% Ga=As : 24.84%
		π = 1.92	π : 0.4392 Ga (sp ^{99.99}) + 0.8984 As (sp ^{99.99})	19.29% (Ga) 80.71% (As)		
R' = NHC	2.33	σ = 1.85	σ : 0.6076 Ga (sp ^{0.98}) + 0.7942 As (sp ^{12.06})	36.92% (Ga) 63.08% (As)	2.14/1.71/0.43	Ga-As : 7.12% Ga=As : 75.34% Ga=As : 17.54%
		π = 1.93	π : 0.4370 Ga (sp ^{82.50}) + 0.8995 As (sp ^{99.99})	19.09% (Ga) 80.91% (As)		

Table 11. Selected results for the natural bond orbital (NBO) and natural resonance theory (NRT) analyses at the B3LYP/LANL2DZ+dp level of theory for R'Ga≡AsR' compounds that have large substituents.

R'	SiMe(Si <i>t</i> Bu ₃) ₂	Si <i>i</i> PrDis ₂	NHC
In≡As (Å)	2.446	2.430	2.482
∠R'-In-As (°)	155.9	168.4	171.3
∠In-As-R' (°)	127.8	120.3	110.8
∠R'-In-As-R' (°)	173.9	162.0	168.3
Q _{In} ¹	0.874	0.880	1.021
Q _{As} ²	-0.783	-0.822	-0.359
ΔE _{ST} (kcal mol ⁻¹) ³	41.5	45.2	35.7
Wiberg BO ⁴	2.174	2.271	2.141

1 The natural charge density on the central In atom.

2 The natural charge density on the central As atom.

3 BE = E(triplet state for In-R') + E(triplet state for As-R') - E(singlet state for R'In≡AsR').

4 The Wiberg bond index (WBI) for the In-As bond.

5 ΔH₁ = E(:In=AsR'₂) - E(R'In≡AsR'); see Scheme 2.

6 ΔH₂ = E(R'₂In=As:) - E(R'In≡AsR'); see Scheme 2.

Table 12. The geometrical parameters, natural charge densities (Q_{In} and Q_{As}), Binding Energies (BE), the HOMO-LUMO Energy Gaps, the Wiberg Bond Index (WBI), and some reaction enthalpies for R'In≡AsR' at the B3LYP/LANL2DZ+dp//RHF/3-21G* Level of Theory.

R'In=AsR'	WBI	NBO analysis			NRT analysis	
		Occupancy	Hybridization	Polarization	total/covalent/ ionic	Resonance weight
R' = SiMe(Si ^t Bu ₃) ₂	1.50	$\sigma = 1.87$	$\sigma : 0.4940 \text{ In}$ (sp ^{1.58}) + 0.8695 As (sp ^{1.28})	24.41% (In) 75.59% (As)	2.31/1.55/0.76	In-As : 5.78% In=As : 55.2 % In=As : 39.0%
		$\pi = 1.85$	$\pi : 0.4411 \text{ In}$ (sp ^{2.80}) + 0.8975 As (sp ^{4.33})	19.45% (In) 80.55% (As)		
R' = Si ⁱ PrDis ₂	1.48	$\sigma = 1.87$	$\sigma : 0.4854 \text{ In}$ (sp ^{1.71}) + 0.8743 As (sp ^{1.26})	23.56% (In) 76.44% (As)	2.18/1.62/0.56	In-As : 6.01% In=As : 56.29% In=As : 37.70%
		$\pi = 1.83$	$\pi : 0.3873$ In (sp ^{99.99}) + 0.9220 As (sp ^{1.00})	15.00% (In) 85.00% (As)		
R' = NHC	1.33	$\sigma = 1.80$	$\sigma : 0.5709 \text{ In}$ (sp ^{1.07}) + 0.8210 As (sp ^{8.66})	32.60% (In) 67.40% (As)	2.21/1.48/0.73	In-As : 7.72% In=As : 78.30% In=As : 13.98%
		$\pi = 1.94$	$\pi : 0.4805$ In (sp ^{37.19}) + 0.8770 As (sp ^{14.95})	23.09% (In) 76.91% (As)		

Table 13. Selected results for the natural bond orbital (NBO) and natural resonance theory (NRT) analyses at the B3LYP/LANL2DZ+dp level of theory for R'In=AsR' compounds that have large substituents.

R'	SiMe(Si ^t Bu ₃) ₂	Si ⁱ PrDis ₂	NHC
$\text{TI}=\text{As}$ (Å)	2.615	2.565	2.653
$\angle \text{R}'-\text{TI}-\text{As}$ (°)	176.9	177.6	178.7
$\angle \text{TI}-\text{As}-\text{R}'$ (°)	127.7	121.8	108.0
$\angle \text{R}'-\text{TI}-\text{As}-\text{R}'$ (°)	172.2	170.4	175.2
Q_{TI}^1	0.310	0.246	0.262
Q_{As}^2	-0.462	-0.440	-0.313
ΔE_{ST} (kcal mol ⁻¹) ³	45.07	32.71	34.83
Wiberg BO ⁴	2.157	2.214	2.209

1 The natural charge density on the central TI atom.

2 The natural charge density on the central As atom.

3 BE = E(triplet state for TI-R') + E(triplet state for As-R') - E(singlet state for R'TI=AsR').

4 The Wiberg bond index (WBI) for the TI-As bond.

5 $\Delta H_1 = E(-\text{TI}=\text{AsR}'_2) - E(\text{R}'\text{TI}=\text{AsR}')$; see Scheme 2.

6 $\Delta H_2 = E(\text{R}'_2\text{TI}=\text{As}) - E(\text{R}'\text{TI}=\text{AsR}')$; see Scheme 2.

Table 14. The geometrical parameters, natural charge densities (Q_{TI} and Q_{As}), Binding Energies (BE), the HOMO-LUMO Energy Gaps, the Wiberg Bond Index (WBI), and some reaction enthalpies for R'TI=AsR' at the B3LYP/LANL2DZ+dp//RHF/3-21G* Level of Theory.

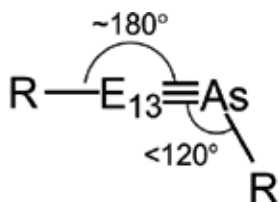
R'Tl=AsR'	WBI	NBO analysis			NRT analysis	
		Occupancy	Hybridization	Polarization	total/covalent/ ionic	Resonance weight
R' = SiMe(Si ^t Bu ₃) ₂	2.15	σ = 1.74	σ : 0.5404 Π (sp ^{1.51}) + 0.8414 As (sp ^{2.20})	29.20% (Π) 70.80% (As)	2.24/1.68/0.56	Π-As : 6.11% Π=As : 57.27% Π=As : 36.62%
		π = 1.79	π : 0.3968 Π (sp ^{4.25}) + 0.9179 As (sp ^{1.51})	15.74% (Π) 84.26% (As)		
R' = Si ⁱ PrDis ₂	2.21	σ = 1.90	σ : 0.3627 Π (sp ^{38.20}) + 0.9318 As (sp ^{1.44})	13.16% (Π) 86.84% (As)	2.16/1.73/0.43	Π-As : 7.01% Π=As : 66.48% Π=As : 26.51%
		π = 1.94	π : 0.3315 Π (sp ^{99.99}) + 0.9435 As (sp ^{1.00})	10.99% (Π) 89.01% (As)		
R' = NHC	2.11	σ = 1.97	σ : 0.7814 Π (sp ^{0.07}) + 0.6240 As (sp ^{52.63})	61.06% (Π) 38.94% (As)	2.14/1.71/0.43	Π-As : 6.71% Π=As : 75.51% Π=As : 17.78%
		π = 1.97	π : 0.4726 Π (sp ^{57.71}) + 0.8812 As (sp ^{17.96})	22.34% (Π) 77.66% (As)		

Table 15. Selected results for the natural bond orbital (NBO) and natural resonance theory (NRT) analyses at the B3LYP/LANL2DZ+dp level of theory for R'Tl=AsR' compounds that have large substituents.

4. Conclusion

This study of the effect of substituents on the possibility of the existence of triply bonded RE₁₃=AsR allows the following conclusions to be drawn (**Scheme 2**):

1. The theoretical observations provide strong evidence that bonding mode (B) is dominant in the triply bonded RE₁₃=BiR species, because their structures are bent due to electron transfer (denoted by arrows in **Figure 1**) and the relativistic effect, which increases stability.
2. The theoretical evidence shows that both the electronic and the steric effects of substituents are crucial to rendering the E₁₃=As triple bond synthetically accessible. However, this theoretical study shows that these E₁₃=As triple bonds are weak. They are not as strong as the traditional C≡C triple bond. The results of this theoretical study show that triply bonded R'E₁₃=AsR' molecules that feature bulky substituents are more stable because bulky substituents not only protect the central E₁₃=As triple bond because there is large steric hindrance but also prohibit polymerization reactions.



$E_{13} = \text{B, Al, Ga, In, and Tl}$

$R = \left\{ \begin{array}{l} \text{F, HO, H, CH}_3, \text{ and SiH}_3 \\ \text{SiMe(Si}^t\text{Bu}_3)_2, \text{ Si}^i\text{PrDis}_2, \text{ and NHC} \end{array} \right.$

Scheme 2. The predicted structure for the triply bonded $\text{RE}_{13}\equiv\text{AsR}$ molecules based on the present theoretical computations.

Acknowledgements

The authors are grateful to the National Center for High-Performance Computing of Taiwan in providing huge computing resources to facilitate this research. They also thank the Ministry of Science and Technology of Taiwan for the financial support.

Author details

Jia-Syun Lu¹, Ming-Chung Yang¹, Shih-Hao Su¹ and Ming-Der Su^{1,2*}

*Address all correspondence to: midesu@mail.ncyu.edu.tw

¹ Department of Applied Chemistry, National Chiayi University, Chiayi, Taiwan

² Department of Medicinal and Applied Chemistry, Kaohsiung Medical University, Kaohsiung, Taiwan

References

- [1] Power PP. π -Bonding and the lone pair effect in multiple bonds between heavier main group elements. *Chemical Review*. 1999;**99**:3463-3504
- [2] Jutzi P. Stable system with a triple bond to silicon or its homologues: Another challenge. *Angewandte Chemie International Edition*. 2000;**39**:3797-3800
- [3] Weidenbruch M. Some recent advances in the chemistry of silicon and its homologues in low coordination states. *Journal of Organometallic Chemistry*. 2002;**646**:39-352
- [4] Power PP. Silicon, germanium, tin and lead analogues of acetylenes. *Chemical Communications*. 2003;**17**:2091-2101

- [5] Power PP. Synthesis and some reactivity studies of germanium, tin and lead analogues of alkynes. *Applied Organometallic Chemistry*. 2005;**19**:488-493
- [6] Lein M, Krapp A, Frenking G. Why do the heavy-atom analogues of acetylene E_2H_2 ($E = Si-Pb$) exhibit unusual structures? *Journal of the American Chemical Society*. 2005;**127**:6290-6299
- [7] Sekiguchi A, Ichinohe M, Kinjo R. The chemistry of disilyne with a genuine si-si triple bond: Synthesis, structure, and reactivity. *Bulletin of the Chemical Society of Japan*. 2006;**79**:825-832
- [8] Power PP. Bonding and reactivity of heavier group 14 element alkyne analogues. *Organometallics*. 2007;**26**:4362-4372
- [9] Sekiguchi, A. Disilyne with a silicon-silicon triple bond: A new entry to multiple bond chemistry. *Pure and Applied Chemistry*. 2008;**80**:447-457
- [10] Sekiguchi A, Kinjo R, Ichinohe M. Interaction of π -bonds of the silicon-silicon triple bond with alkali metals: An isolable anion radical upon reduction of a disilyne. *Synthetic Metals*. 2009;**159**:773-775
- [11] Fischer RC, Power PP. π -bonding and the lone pair effect in multiple bonds involving heavier main group elements: Developments in the new millennium. *Chemical Review*. 2010;**110**:3877-3923
- [12] Peng Y, Fischer RC, Merrill WA, Fischer J, Pu L, Ellis BD, Fettinger JC, Herber RH, Power PP. Substituent effects in ditetrel alkyne analogues: Multiple vs. single bonded isomers. *Chemical Science*. 2010;**1**:461-468
- [13] Sasamori T, Han J S, Hironaka K, Takagi N, Nagase S, Tokitoh N. Synthesis and structure of stable 1,2-diaryldisilyne. *Pure and Applied Chemistry*. 2010;**82**:603-612
- [14] Sekiguchi A, Kinjo R, Ichinohe M. A stable compound containing a silicon-silicon triple bond. *Science*. 2004;**305**:1755-1757
- [15] Wiberg N, Vasisht S K, Fischer G, Mayer P. Disilynes. iii [1] a relatively stable disilyne $RSi\equiv SiR$ ($R = SiMe(SitBu_3)_2$). *Zeitschrift für anorganische und allgemeine Chemie*. 2004;**630**:1823-1828
- [16] Sasamori T, Hironaka K, Sugiyama T, Takagi N, Nagase S, Hosoi Y, Furukawa Y, Tokitoh N. Synthesis and reactions of a stable 1,2-diaryl-1,2-dibromodisilene: A precursor for substituted disilenes and 1,2-diaryldisilyne. *Journal of the American Chemical Society*. 2008;**130**:13856-13857
- [17] Stender M, Phillips AD, Wright RJ, Power PP. Synthesis and characterization of a digermanium analogue of an alkyne. *Angewandte Chemie International Edition*. 2002;**41**:1785-1787
- [18] Stender M, Phillips AD, Power PP. Formation of $[Ar^*Ge\{CH_2C(Me)C(Me)CH_2\}CH_2C(Me)N]_2$ ($Ar^* = C_6H_3-2,6-Trip_2$; $Trip = C_6H_2-2,4,6-i-Pr_3$) via reaction of $Ar^*GeGeAr^*$ with 2,3-dimethyl-1,3-butadiene: Evidence for the existence of a Germanium analogue of an alkyne. *Chemical Communication*. 2002;**12**:1312-1313

- [19] Pu L, Phillips AD, Richards AF, Stender M, Simons RS, Olmstead MM, Power PP. Germanium and tin analogues of alkynes and their reduction products. *Journal of the American Chemical Society*. 2003;**125**:11626-11636
- [20] Sugiyama Y, Sasamori T, Hosoi Y, Furukawa Y, Takagi N, Nagase S, Tokitoh N. Synthesis and properties of a new kinetically stabilized digermene: New insights for a germanium analogue of an alkyne. *Journal of the American Chemical Society*. 2006;**128**:1023-1031
- [21] Spikes GH, Power PP. Lewis base induced tuning of the Ge-Ge bond order in a "digermene". *Chemical Communication*. 2007;**1**:85-87
- [22] Phillips AD, Wright RJ, Olmstead MM, Power PP. Synthesis and characterization of 2,6-Dipp₂-H₃C₆SnSnC₆H₃-2,6-Dipp₂ (Dipp = C₆H₃-2,6-Prⁱ₂): A Tin analogue of an alkyne. *Journal of the American Chemical Society*. 2002;**124**:5930-5931
- [23] Pu L, Twamley B, Power PP. Synthesis and characterization of 2,6-Trip₂-H₃C₆PbPbC₆H₃-2,6-Trip₂ (Trip = C₆H₂-2,4,6-*i*-Pr₃): A stable heavier group 14 element analogue of an alkyne. *Journal of the American Chemical Society*. 2000;**122**:3524-3525
- [24] Danovich D, Ogliaro F, Karni M, Apeloig Y, Cooper DL, Shaik S. Silynes (RC=SiR') and disilynes (RSi=SiR'): Why are less bonds worth energetically more? *Angewandte Chemie International Edition*. 2001;**40**:4023-4026
- [25] Gau D, Kato T, Saffon-Merceron N, Cozar AD, Cossio FP, Baceiredo A. Synthesis and structure of a base-stabilized *c*-phosphino-*Si*-amino silyne. *Angewandte Chemie International Edition*. 2010;**49**:6585-6588
- [26] Lüthmann N, Müller T. A compound with a Si-C triple bond. *Angewandte Chemie International Edition*. 2010;**49**:10042-10044
- [27] Wu P-C, Su M-D. A new target for synthesis of triply bonded plumbacetylene (RC≡PbR): A theoretical design. *Organometallics*. 2011;**30**:3293-3301
- [28] Wu P-C, Su M-D. Effects of substituents on the thermodynamic and kinetic stabilities of HCGeX (X = H, CH₃, F, and Cl) isomers. A theoretical study. *Inorganic Chemistry*. 2011;**50**:6814-6814
- [29] Wu P-C, Su M-D. Theoretical designs for germaacetylene (RC≡GeR): A new target for synthesis. *Dalton Transactions*. 2011;**40**:4253-4259
- [30] Paetzold PI, Maisch H. Borimide, II. borimide als zwischenstufen bei der abspaltung von halogenwasserstoff aus boran-aminen. *Chemische Berichte*. 1968;**101**:2870-2873
- [31] Paetzold PI, Stohr G. Borimide, III. borimide als dipolarophile bei der 1,3-dipolaren cyclisierungsreaktion. *Chemische Berichte*. 1968;**101**:2874-2880
- [32] Paetzold PI, Stohr G, Maisch H, Lenz H. Borimide, IV. Die reaktion von borimiden mit phenylacetylen. *Chemische Berichte*. 1968;**101**:2881-2888
- [33] Paetzold P, Plotho CV. Über weitere monomere borimide und ihre reaktionen. *Chemische Berichte*. 1982;**115**:2819-2825

- [34] Geschwentner M, Eleter G, Meller A. Supermesityl-stabilisierte iminoborane. III. Zeitschrift für anorganische und allgemeine Chemie. 1993;**619**:1474-1478
- [35] Gilbert TM. Ab initio computational studies of heterocycloalkynes: Structures, natural bond orders, ring strain energies, and isomerizations of cyclic iminoboranes and iminoalanes. Organometallics. 2000;**19**:1160-1165
- [36] Steuber EV, Elter G, Noltemeyer M, Schmidt H-G, Meller A. First B-organyloxy-substituted iminoboranes: Preparation, stabilization, and reactivity. Organometallics. 2000;**19**:5083-5091
- [37] Rivard E, Merrill WA, Wolf R, Spikes GH, Power PP. Boron–Pnictogen multiple bonds: Donor-stabilized P=B and As=B bonds and a hindered iminoborane with a B–N triple bond. Inorganic Chemistry. 2007;**46**:2971-2978
- [38] Braunschweig H, Matz F, Radacki K, Schneider A. Reactivity of platinum iminoboryl complexes toward covalent element–hydrogen bonds of opposing polarity. Organometallics. 2010;**29**:3457-3462
- [39] Braunschweig H, Kupfer T, Radacki K, Schneider A, Seeler F, Uttinger K, Wu H. Synthesis and reactivity studies of iminoboryl complexes. Journal of the American Chemical Society. 2008;**130**:7974-7983
- [40] Dahcheh F, Stephan DW, Bertrand G. Oxidative addition at a carbene center: Synthesis of an iminoboryl–CAAC adduct. Chemistry: A European Journal. 2015;**21**:199-204
- [41] Pyykko P, Desclaux J-P. Relativity and the periodic system of elements. Accounts of Chemical Research. 1979;**12**:276-281
- [42] Kutzelnigg W. Chemical bonding in higher main group elements. Angewandte Chemie International Edition. 1984;**23**:272-295
- [43] Pyykko P. Relativistic effects in structural chemistry. Chemical Reviews. 1988;**88**:563-594
- [44] Pyykko P. Strong closed-shell interactions in inorganic chemistry. Chemical Reviews. 1997;**97**:597-636
- [45] Wiberg KB. Application of the pople-santry-segal CNDO method to the cyclopropylcarbanyl and cyclobutyl cation and to bicyclobutane. Tetrahedron. 1968;**24**:1083-1096
- [46] Reed AE, Curtiss LA, Weinhold F. Intermolecular interactions from a natural bond orbital, donor-acceptor viewpoint. Chemical Reviews. 1988;**88**:899-926
- [47] Glendening ED, Weinhold F. Natural resonance theory: I. General formalism. Journal of Computational Chemistry. 1998;**19**:593-609
- [48] Glendening ED, Weinhold F. Natural resonance theory: II. Natural bond order and valency. Journal of Computational Chemistry. 1998;**19**:610-627
- [49] Glendening ED, Badenhoop JK, Weinhold F. Natural resonance theory: III. Chemical applications. Journal of Computational Chemistry. 1998;**19**:628-646

Theoretical Investigations of Mechanisms for the Reactions of Seven-Member Ring N-Heterocyclic Carbene and Its Heavier Analogues

Zheng-Feng Zhang, Ling-Hsuan Liu and Ming-Der Su

Additional information is available at the end of the chapter

<http://dx.doi.org/10.5772/intechopen.75227>

Abstract

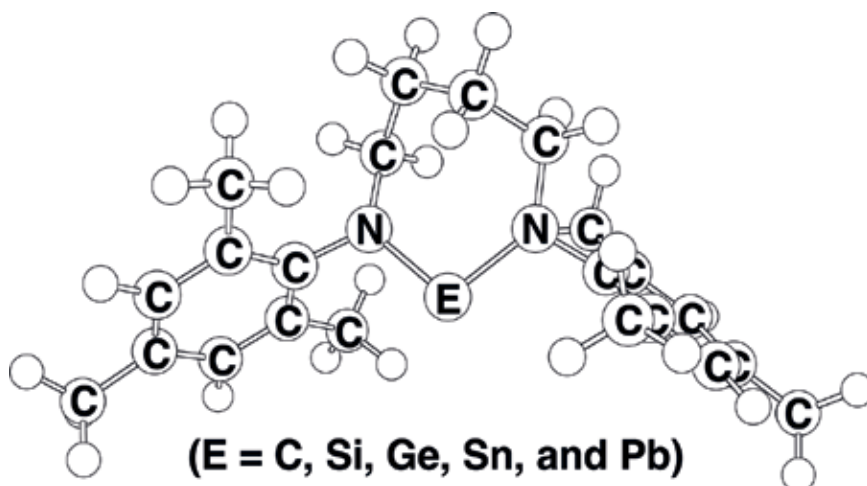
The potential energy surfaces for the chemical reactions of group 14 carbenes were studied using density functional theory (B3LYP/LANL2DZ + dp). Five group 14 carbene species containing a seven-member ring, **7-Rea-E**, where E = C, Si, Ge, Sn and Pb, were chosen as model reactants for this work. Three types of chemical reactions (water addition, imine cycloaddition and dimerization) were used to study the reactivity of these **7-Rea-E** molecules. Present theoretical investigations suggest that the relative reactivity of carbenes decreases in the order: **7-Rea-C** > **7-Rea-Si** > **7-Rea-Ge** > **7-Rea-Sn** > **7-Rea-Pb**. That is, the heavier the group 14 atom (E), the more stable its corresponding **7-Rea-E** compound to chemical reaction. This study's theoretical findings suggest that all of the seven-member **7-Rea-E** should be readily synthesized and isolated at room temperature, since they are quite inert to chemical reaction, except for reaction with moisture. Furthermore, the group 14 **7-Rea-E** singlet-triplet energy splitting, as described in the configuration-mixing model of Pross and Shaik, can be used as a diagnostic tool to predict their reactivity. The results obtained allow a number of predictions to be made.

Keywords: N-heterocyclic carbenes, seven-member carbene, group 14 elements, density functional theory, imine cycloaddition, dimerization, water addition

1. Introduction

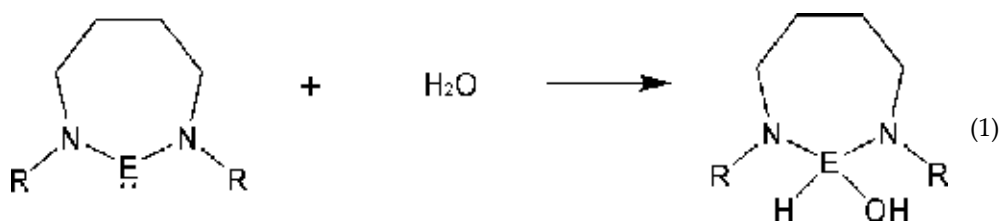
Since the first synthesis and isolation of thermally stable carbenes, imidazol-2-ylidenes, by Arduengo and co-workers [1, 2], the chemistry of N-heterocyclic carbenes (NHCs) has been the subject of intense research and has been studied both experimentally and theoretically during the last two decades [3–23]. Indeed, the isolation of stable NHCs has led to a renaissance for the nucleophilic

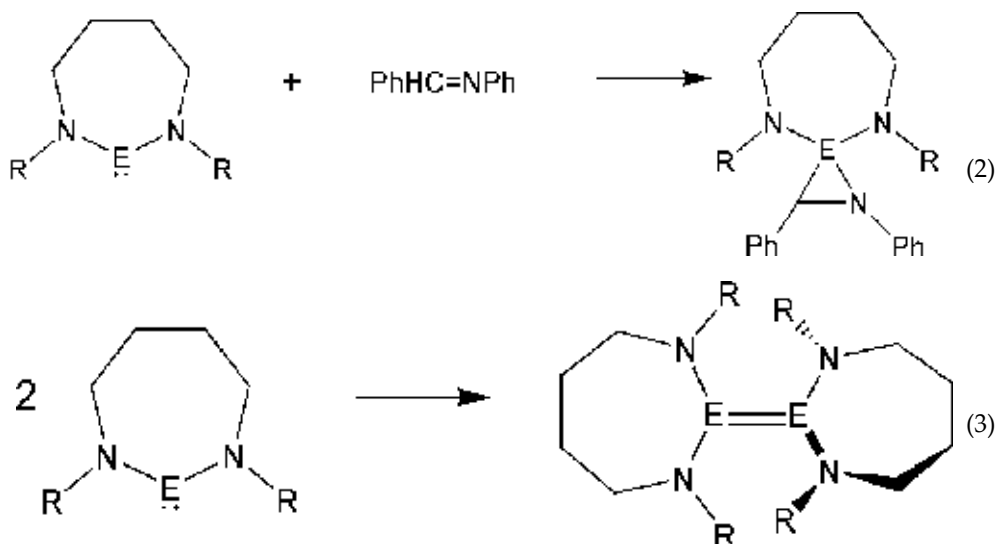
carbenes. In particular, NHCs were found to be strong, two-electron σ -donors and to be highly air- and moisture-stable substituents, which allowed the preparation of organometallic catalysts of enormous utility in organic synthesis [24–34]. Nevertheless, although a broad range of geometrical structures of NHCs have been synthesized and structurally characterized, their architectures are still limited to the three- [25], four- [36, 37], five- [35–40], and six-membered rings [41–47].



Recently, because of the elegant studies performed by Cavell, Dervisi, Fallis and many coworkers, thermally stabilized molecules that possess the seven-member ring unit, in which the carbene center is flanked by two nitrogen atoms, have been synthesized and structurally characterized [48–50]; one is 1,3-bis(2,4,6-trimethylphenyl)-4,5,6,7-tetrahydro-3H-[1,3]diazepine (**7-Mes**), a novel seven-member carbene system and the other is the first stable 1,3-bis(2,6-dimethylphenyl)-4,5,6,7-tetrahydro-3H-[1,3]diazepine (**7-Xyl**) to have been isolated, again by taking advantage of bulky substituent groups. As a result, carbene systems that feature a seven-member ring are no longer imaginary species. However, attempts to isolate other heavy carbene analogues containing the heavy group 14 elements (such as Si, Ge, Sn, and Pb) have all been unsuccessful, until now.

The objective of this work is, therefore, to enlarge upon previous experimental approaches by studying the mechanism and reactivity of seven-member heavy carbene systems, wherein the carbene center (E) is represented by group 14 atoms from carbon to lead. To the best of the authors' knowledge, neither experimental nor theoretical studies have yet been performed on seven-member-rings that possess main group elements, let alone a systematic theoretical study of the elemental effects on the reactivity of such species. In consequence, a study of three kinds of typical reactions for seven-member carbene analogues ($E'' = \text{C, Si, Ge, Sn and Pb}$), Eqs. (1)–(3), using the density functional theory (DFT), is represented as follows:





(R = 2,4,6-trimethylbenzene)

It is hoped that this theoretical study will (i) clarify the reaction mechanism and determine the possible transition-state structures and the relative energetics for Eqs. (1)–(3), (ii) examine the thermodynamics of the seven-member carbene analogues' reactions with various substrate molecules and (iii) establish general trends and predictions for the chemical reactions of seven-member-ring heavy NHCs.

2. Computational details

Geometries were fully optimized using the B3LYP level of theory, which is implemented by the Gaussian 03 program package [51]. Moreover, the LANLADZ basis sets were utilized in this study. The LANL2DZ basis sets contain the pseudo-relativistic effective core potentials on the group 14 elements modeled, using the double-zeta (DZ) basis sets augmented by a set of d-type polarization functions [52], in which the d exponents used for C, Si, Ge, Sn and Pb were 0.587, 0.296, 0.246, 0.186 and 0.179, respectively. As a result, B3LYP/LANL2DZ + dp represents the B3LYP computations. It is noteworthy that the model reactant (**7-Ring-E**; E = group 14 element) has a total of 604 (180 electrons) basis functions for LANL2DZ + dp sets. Frequency computations were executed on all of the stationary points in order to make sure whether they are the minimum points (no imaginary frequencies) or the transition states (only one imaginary frequency). Therefore, the relative energies were corrected by using the zero-point energies (ZPE, not scaled). Also, the relative free energies (ΔG) at 298 K were computed at the same level of theory.

3. Results and discussion

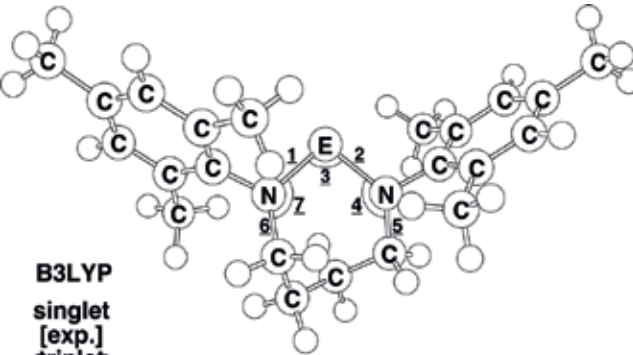
3.1. Geometric structures of 7-Mes

In order to verify that the computational method used in this work is suitable for discussion of the potential energy surfaces for the related chemical reactions (Eqs. (1)–(3)), the geometry

of free seven-member N-heterocyclic carbene, **7-Mes** is firstly considered. Since the structure of **7-Mes** has been determined by X-ray crystal analysis, its geometry optimization was first performed, in order to calibrate the B3LYP/LANL2DZ + dp calculations. As shown in **Figure 1**, the calculated average C-N and N-C (ring) distances are 1.356 and 1.493 Å, respectively. These values are very close to those of 1.348 and 1.493 Å, observed for the X-ray crystal structure [48–50]. In addition, the calculated \angle N-C-N and average \angle C-N-C (ring) angles are estimated to be 118.2° and 128.6°, which values are in good agreement with the experimental values (116.6° and 128.8° [48–50], respectively). These results strongly suggest that the B3LYP/LANL2DZ + dp calculations are reliable enough for the present purpose.

3.2. Geometric and electronic structures of 7-Rea-E

Other reactants for seven-member heavy carbene analogues (**7-Rea-E**) were also examined at both singlet and triplet states, which were calculated at the B3LYP/LANL2DZ + dp level.



7-Rea-E

E	C	Si	Ge	Sn	Pb
1	1.356 [1.349] <1.381>	1.752	1.861	2.034	2.121
2	1.356 [1.346] <1.401>	1.750	1.872	2.049	2.124
3	118.2° [116.6°] <123.0°>	109.9°	101.5°	97.25°	93.11°
4	130.7° [130.6°] <114.7°>	136.2°	132.4°	131.4°	124.7°
5	1.499 [1.502] <1.483>	1.478	1.476	1.473	1.477
6	1.487 [1.483] <1.473>	1.472	1.478	1.475	1.480
7	126.4° [126.9°] <118.5°>	137.1°	125.0°	125.2°	123.6°

Figure 1. B3LYP/LANL2DZ + dp optimized geometries (in Å and deg) of the reactants **7-Rea-E** (E = C, Si, Ge, Sn, and Pb) at the singlet and triplet states. The experimental values (see ref. [51]) are in parenthesis. Hydrogens are omitted for clarity.

The selected geometrical parameters of **7-Rea-E** for the singlet and triplet states are detailed in **Figure 1** and compared with some available experimental data [48–50]. The calculated molecular orbitals (MOs) for the **7-Rea-E** molecules are given in **Figure 2**. Several important conclusions can be drawn from these figures.

Firstly, as seen in **Figure 1**, regardless of whether it is a singlet or triplet of neutral **7-Rea-E** compounds, the E—N bond length shows a monotonic increase in the period, from C toward Pb. For instance, for the singlet neutral group 14 **7-Rea-E**, the E—N distances increase in the order: **7-Rea-C** (1.356 Å) < **7-Rea-Si** (1.751 Å) < **7-Rea-Ge** (1.867 Å) < **7-Rea-Sn** (2.042 Å) < **7-Rea-Pb** (2.123 Å). The same phenomenon is observed for the triplet neutral group 14 **7-Rea-E**, as given in **Figure 1**.

However, irrespective of its multiplicity, the bond angle, \angle NEN, decreases uniformly as the central atom, E, progresses from C to Pb. For example, the bond angle, \angle NEN, decreases in the order: 118.2° (**7-Rea-C**) > 109.9° (**7-Rea-Si**) > 101.5° (**7-Rea-Ge**) > 97.25° (**7-Rea-Sn**) > 93.11° (**7-Rea-Pb**)

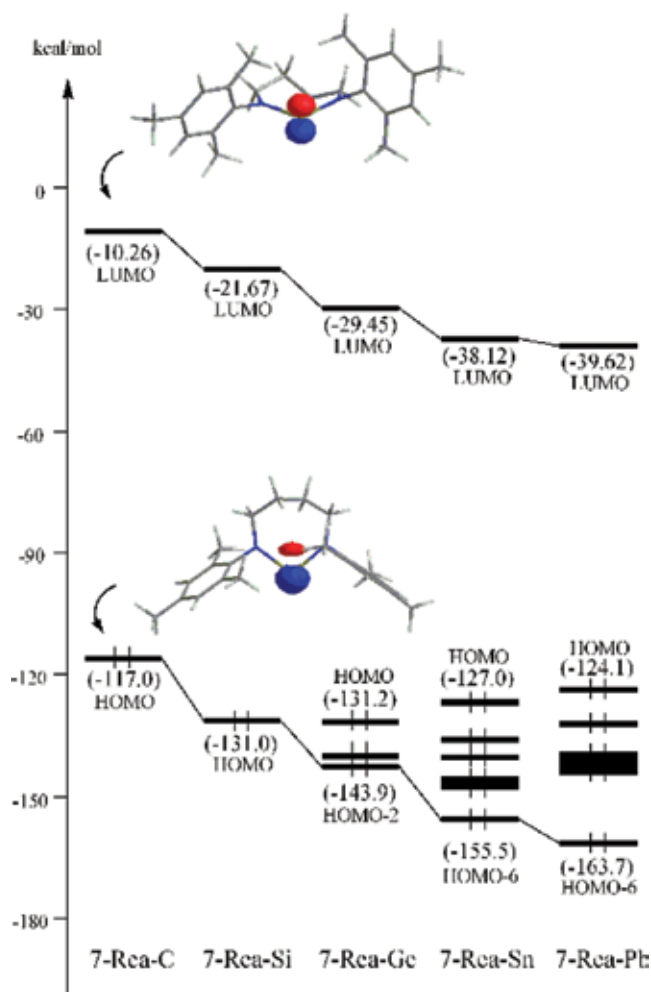


Figure 2. Calculated frontier molecular orbitals for the **7-Rea-E** (E = C, Si, Ge, Sn, and Pb) species. For more information see the text.

and 123.0° (**7-Rea-C**) > 107.2° (**7-Rea-Si**) > 96.18° (**7-Rea-Ge**) > 89.09° (**7-Rea-Sn**) > 85.64° (**7-Rea-Pb**), at the singlet and triplet states, respectively. Accordingly, it is apparent that the angles at the group 14 elements generally decrease as atomic number increases (from C to Pb). This can be attributed to the relativistic effect [54–57]. As a result, the heavier group 14 elements have a stronger tendency to maintain the $(ns)^2(np)^3$ valence electron configuration. Subsequently, the \angle NEN angle monotonously decreases from **7-Rea-C** to **7-Rea-Pb**, for both singlet and triplet states.

Secondly, in order to gain a greater understanding of the nature of the chemical bonding in the series of **7-Rea-E** reactants, the valence molecular orbitals based on the B3LYP/LANL2DZ + dp calculations are represented in **Figure 2**. Basically, there are two important key orbitals, which determine both the chemical and physical properties off the traditional carbene systems, i.e., the nonbonding σ (sp^2) orbital and the unoccupied $p-\pi$ orbital, both of which are strongly located on the carbonic center [53].

Note that the nature of the σ and the $p-\pi$ orbitals in **7-Rea-E** are quite similar to those encountered in traditional group 14 divalent compounds [53]. Nevertheless, their energy levels no longer exist on the HOMO and LUMO, respectively, as is already known for the CH₂ system [53]. As seen in **Figure 2**, the substitution of a single E atom at the **7-Rea-E** center decreases the energy of the σ orbital, on going from **7-Rea-C** to **7-Rea-Pb**. Likewise, this substitution also decreases the energy of the unoccupied $p-\pi$ orbital. The reason for such molecular orbital locations may be attributed to the “orbital non-hybridization effect”, also known as the “inert s-pair effect”, as discussed earlier [54–57].

Thirdly, the other interesting feature is the singlet-triplet splitting ΔE_{st} (= $E_{\text{triplet}} - E_{\text{singlet}}$). From **Figure 2**, it is apparent that the magnitude of the difference in energy between the occupied σ (sp^2) and unoccupied $p-\pi$ for the seven-member-ring heavy NHCs becomes larger along the series from **7-Rea-C** to **7-Rea-Pb**. The DFT calculations indicate that the ΔE_{st} for the **7-Rea-E** species increases in the order: 107 (**7-Rea-C**) < 109 (**7-Rea-Si**) < 114 < (**7-Rea-Ge**) < 123 (**7-Rea-Sn**) 124 (**7-Rea-Pb**) kcal/mol, respectively. In other words, the heavier the central group 14 atom (E), the larger is the ΔE_{st} of the seven-member **7-Rea-E** molecule. Again, as discussed earlier, the reason for this difference can be traced directly to electronic factors. In consequence, the theoretical findings reveal that the electronic perturbation effect, wherein the symmetry of frontier orbitals changes, should play a decisive role in determining the energy ordering of the frontier orbitals. This, in turn, affects the magnitude of ΔE_{st} for the seven-member carbene analogues. It should be noted that the stability of the seven-member-ring heavy NHCs is determined by the singlet-triplet energy separations in **7-Rea-E**. If ΔE_{st} is small, the carbene-type structures are unstable and subsequently easily undergo chemical reaction (such as reaction with solvents, etc.). As already mentioned, the B3LYP calculations demonstrate that the group 14 **7-Rea-E** species have comparatively large ΔE_{st} (> 107 kcal/mol). Accordingly, these molecules should be stable enough to be detected experimentally. The supporting evidence comes from the fact that, so far, one NHC compound with a seven-member ring (i.e., **7-Rea-C**) has been synthesized and characterized [48–50]. Also, the synthesis and structure of a dialkylplumbylene with a similar substitution pattern was reported recently in which the lead atom is part of a seven-member ring [58].

Finally, since the DFT calculations indicate that the **7-Rea-E** (E = C, Si, Ge, Sn and Pb) molecules all possess a singlet ground state, then all related chemical reactions (Eqs. (1)–(3)) should proceed on the singlet surface. This study shall, therefore, herewith focus on the singlet surface.

3.3. Geometries and energetics of 7-Rea-E+ H₂O

The mechanisms, which proceed via Eq. (1), are now considered, focusing on the transition states, as well as on the addition products themselves. That is, the addition mechanisms may be thought to proceed as follows: reactants (**7-Rea-E+ H₂O**) → transition state (**7-TS-E-1**) → product (**7-Pro-E-1**). The optimized geometries, calculated at the B3LYP/LANL2DZ + dp level of theory, involving **7-TS-E-1** and **7-Pro-E-1** are detailed in **Figure 3**. The corresponding relative energies at the B3LYP level of theory are given in **Table 1**. There are several important conclusions that can be drawn from these results.

Firstly, in relation to the O-H bond addition reaction path, the transition state for each **7-Rea-E** case (**7-TS-C-1**, **7-Rea-Si-1**, **7-TS-Ge-1**, **7-TS-Sn-1**, and **7-TS-Pb-1**) has been located at the DFT level of theory. As can be seen in **Figure 3**, all five transition state structures show the same three-center pattern, involving E, oxygen and hydrogen atoms. The transition state vectors indicate an addition process, primarily with O—H bond stretching, accompanied by migration of a hydrogen atom to the E center.

However, in the transition state, there is a trend for the stretching O—H' bond to become longer and for the forming E—H' bond length to increase, as E increases in atomic weight. For instance, the breaking O—H' bond lengths (Å) are 1.241 (**7-TS-C-1**), 1.303 (**7-TS-Si-1**), 1.419 (**7-TS-Ge-1**), 1.496 (**7-TS-Sn-1**) and 1.656 (**7-TS-Pb-1**), respectively, whereas the forming E—O bond lengths (Å) are 0.682 (**7-TS-C-1**), 0.459 (**7-TS-Si-1**), 0.413 (**7-TS-Ge-1**), 0.284 (**7-TS-Sn-1**) and 0.357 (**7-TS-Pb-1**) longer than that in the (7-Rea-E)(H)(OH) addition product. That is to say, the O-H bond addition happens earlier along the reaction coordinate for **7-Rea-E** with lighter carbene centers. In other words, the E—H' and E—O bond lengths in the transition structure are more product-like for E = Sn and Pb, and more reactant-like for E = C and Si. On the basis of the Hammond postulate [59], **7-TS-Sn-1** and **7-TS-Pb-1** should have the highest activation barriers and **7-TS-C-1** and **7-TS-Si-1** the smallest. Additionally, the barrier height (Gibbs free energy) for the O—H addition reaction decreases in the order (kcal/mol): **7-TS-Pb-1** (+66) > **7-TS-Sn-1** (+48) > **7-TS-Ge-1** (+44) > **7-TS-Si-1** (+30) > **7-TS-C-1** (+21). These values strongly suggest that the heavier the atomic number of the E center, the greater is the barrier to O—H addition.

System	ΔE^{\ddagger} (kcal mol ⁻¹)	ΔH^{\ddagger} (kcal mol ⁻¹)
7-Rea-C	8.51 [21.1]	-51.3 [-41.4]
7-Rea-Si	21.1 [30.2]	-19.4 [-8.96]
7-Rea-Ge	33.7 [44.2]	-12.2 [-0.105]
7-Rea-Sn	37.0 [48.2]	-7.50 [+3.89]
7-Rea-Pb	56.5 [66.4]	+29.0 [+39.0]

¹All were calculated at the B3LYP/LANL2DZ + dp level of theory. The B3LYP optimized structures of the stationary points see **Figure 3**. The Gibbs free energies are given in the square bracket.

²The activation energy of the transition state, relative to the corresponding reactants.

³The reaction enthalpy of the product, relative to the corresponding reactants.

Table 1. Relative energies for the addition reaction of the singlet group 14 **7-Rea-E** species with water: Reactants (**7-Rea-E + H₂O**) → Transition state (**7-TS-E-1**) → Addition product (**7-pro-E-1**)¹.

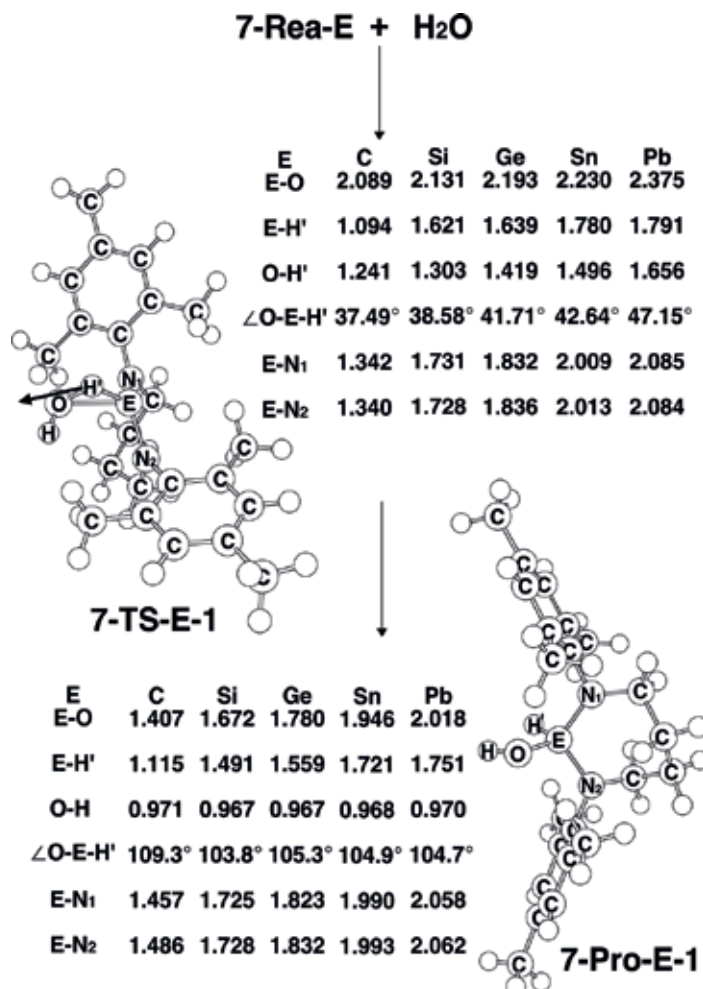


Figure 3. B3LYP/LANL2DZ + dp optimized geometries (in Å and deg) of transition states (7-TS-E-1), and water addition products (7-Pro-E-1) of 7-Rea-E (E = C, Si, Ge, Sn, and Pb). The relative energies for each species see Table 1. Hydrogens are omitted for clarity.

Secondly, as Figure 3 shows, the order of the E-O bond length for the water addition product increases as the atomic weight of the carbene atom, E: 7-Pro-C-1 (1.407 Å) < 7-Pro-Si-1 (1.672 Å) < 7-Pro-Ge-1 (1.780 Å) < 7-Pro-Sn-1 (1.946 Å) < 7-Pro-Pb-1 (2.018 Å). To the authors' best knowledge, experimental structures for such compounds have not yet been identified [48–50]. As already mentioned, a group 14 7-Rea-E with a lighter atomic weight carbene E atom reaches the transition state relatively early, whereas one with a carbene atom, E, of a heavier atomic weight arrives relatively late. For example, the order of Gibbs free enthalpy follows the same trend as the activation energy (kcal/mol): 7-Pro-C-1 (–41) < 7-Pro-Si-1 (–9.0) < 7-Pro-Ge-1 (–0.11) < 7-Pro-Sn-1 (+3.9) < 7-Pro-Pb-1 (+39). Note that the free energies of 7-Pro-C-1 and 7-Pro-Si-1 are lower than those of their corresponding starting materials, whereas the free energies of 7-Pro-Sn-1 and 7-Pro-Pb-1 are higher than those of their corresponding starting materials. Consequently, the theoretical findings strongly indicate that the seven-member carbene (7-Rea-C) and silylene (7-Rea-Si) should be greatly damaged in moist environments, while the

seven-member heavy carbene analogues (such as **7-Rea-Sn** and **7-Rea-Pb**) are moisture-stable compounds. Unfortunately, to the best of the authors' knowledge, no experiments relating to the effect of moisture on **7-Rea-E** molecules have been reported. Therefore, this is a prediction.

Thirdly, all of the above DFT results can be rationalized on the basis of the configuration-mixing (CM) model of Pross and Shaik [60–63]. According to this model, the stabilization of an addition transition state depends on the singlet-triplet splitting, ΔE_{st} ($= E_{\text{triplet}} - E_{\text{singlet}}$), of the reactant group 14 **7-Rea-E**; i.e., a smaller ΔE_{st} results in a more stable transition state, a lower activation energy, a faster addition reaction and a more exothermic reaction. It is necessary to emphasize the importance of the status of the triplet states of the group 14 **7-Rea-E** reactants. Since two new covalent bonds must be formed in the addition product, **7-Rea-E(OH)(H)** (**7-Pro-E-1**), i.e., the E-OH and E-H bonds (**Figure 3**), the bond-prepared **7-Rea-E** state thus must have at least two open shells and the lowest state of this type is the triplet state. Therefore, from the standpoint of valence-bonding [60–63], the bonding in the product can be considered to be between the triplet **7-Rea-E** state and the two doublet radicals (overall singlet), the OH radical and the hydrogen atom. This is much the same as bonding in the water molecule. Namely, H_2O is considered to be between two doublet hydrogen atoms and a triplet oxygen atom [60–63]. As indicated earlier, the DFT results suggest an increasing trend in ΔE_{st} for the **7-Rea-E** reactant, along the group 14 family. This result is in accordance with the trends in activation energy and reaction enthalpy (ΔE^\ddagger , ΔH) for group 14 seven-member **7-Rea-E** species, as already discussed. These results strongly support the previous predictions that the smaller the ΔE_{st} of the group 14 seven-member **7-Rea-E**, the lower is the barrier height and, in turn, the faster is the water addition reaction and the more exothermic is the reaction.

3.4. Geometries and energetics of **7-Rea-E**+ PhHC = NPh

The cycloaddition reactions, which proceed via Eq. (2), are now considered. To ensure consistency with previous work, the following reaction mechanism is used to examine the cycloaddition reaction of group 14 **7-Rea-E** molecules with imine: reactants (**7-Rea-E** + PhHC = NPh) \rightarrow transition state (**7-TS-E-2**) \rightarrow cycloaddition product (**7-Pro-E-2**). The geometries and energetics of the systems (E = C, Si, Ge, Sn and Pb) were calculated using the B3LYP/LANL2DZ + dp level of theory. Selected geometrical parameters and the relative energies of stationary points for the above mechanism are detailed in **Figure 4** and **Table 2**, respectively. The major conclusions to be drawn from the current study can be summarized as follows.

Firstly, a seven-member **7-Rea-E** species and imine (PhHC = NPh) are predicted to undergo a [1 + 2] cycloaddition to produce a cycloaddition product. From **Figure 4**, all of these transition states (i.e., **7-TS-C-2**, **7-TS-Si-2**, **7-TS-Ge-2**, **7-TS-Sn-2** and **7-TS-Pb-2**) proceed in a three-center pattern that involves the carbon, nitrogen and the group 14, E, atoms. The B3LYP computational normal modes associated with the single imaginary frequency are consistent with the C = N activation process, primarily the C = N bond stretching with the migration of an E atom to the double bond. It should be noted that these characteristic three-centered cyclic transition states are quite analogous to the mechanisms observed for the cycloaddition reactions of singlet carbenes [64].

Secondly, the DFT results demonstrate that the larger the $\angle N1E N2$ bond angle, the more reactant-like is the transition state structure, as shown in **Figure 4** [54–57]. Comparison of the C1—N' bond length in the TS structures with the corresponding distance in imine (1.283 Å)

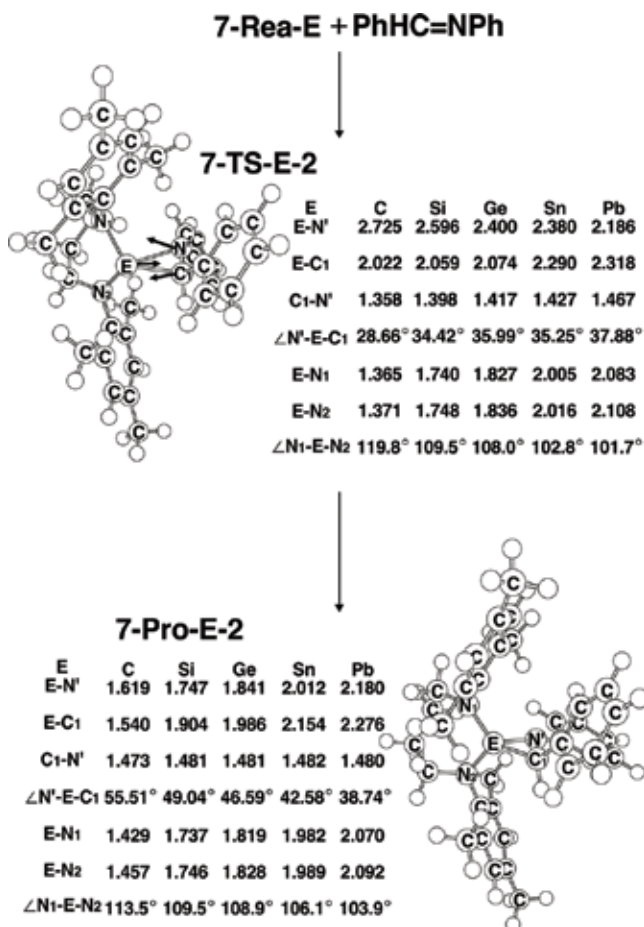


Figure 4. B3LYP/LANL2DZ + dp optimized geometries (in Å and deg) of transition states (7-TS-E-2), and cycloaddition products (7-pro-E-2) of 7-Rea-E (E = C, Si, Ge, Sn, and Pb) and imine. The relative energies for each species see Table 2. Hydrogens are omitted for clarity.

System	ΔE^{\ddagger} (kcal mol ⁻¹)	ΔH^{\ddagger} (kcal mol ⁻¹)
7-Rea-C	9.62 [14.9]	-27.0 [-20.5]
7-Rea-Si	12.4 [18.9]	+4.85 [+11.2]
7-Rea-Ge	20.9 [26.7]	+5.10 [+12.1]
7-Rea-Sn	25.5 [30.1]	+19.6 [+25.2]
7-Rea-Pb	47.5 [51.7]	+48.3 [+52.8]

¹All were calculated at the B3LYP/LANL2DZ + dp level of theory. The B3LYP optimized structures of the stationary points see Figure 4. The Gibbs free energies are given in the square bracket.

²The activation energy of the transition state, relative to the corresponding reactants.

³The reaction enthalpy of the product, relative to the corresponding reactants.

Table 2. Relative energies for the cycloaddition reaction of the singlet group 14 7-Rea-E species with imine: Reactants (7-Rea-E + PhHC=NPh) → transition state (7-TS-E-2) → addition product (7-pro-E-2)¹.

shows that the C1—N' bond distance in the transition structures is stretched by 5.9, 9.0, 10, 11 and 14% for **7-TS-C-2**, **7-TS-Si-2**, **7-TS-Ge-2**, **7-TS-Sn-2** and **7-TS-Pb-2**, respectively. All of the theoretical data indicate that the structures of the TSs (**7-TS-E-2**) are as expected from Hammond's postulate [59]. Namely, the [1 + 2] cycloaddition for the seven-member **7-Rea-E** that possesses lighter group 14 elements, E, has lower activation energy, since its TS resembles the corresponding reactants more closely than the final products. From **Table 2**, it is easily seen that the Gibbs free activation energy (kcal/mol) of the **7-TS-E-2** follows the same trend as the ΔE_{st} in the seven-member **7-Rea-E** system, i.e., **7-TS-C-2** (+15) < **7-TS-Si-2** (+19) < **7-TS-Ge-2** (+27) < **7-TS-Sn-2** (+30) < **7-TS-Pb-2** (+52). That is to say, according to the CM model [60–63], it is predicted that seven-member **7-Rea-E** molecules with a lighter atomic weight E atom have a larger $\angle N1EN2$ bond angle, a smaller ΔE_{st} and experience easier cycloaddition to imine.

Thirdly, as can be seen in **Table 3**, the Gibbs free energy of the final cycloproducts, relative to their corresponding reactants, increases in the order: **7-Pro-C-2** (–21) < **7-Pro-Si-2** (+11) < **7-Pro-Ge-2** (+12) < **7-Pro-Sn-2** (+25) < **7-Pro-Pb-2** (+53), indicating that the reactions of seven-member **7-Rea-E** molecules with heavier group 14 atoms (E) are endothermic. It should also be noted that the order of the reaction enthalpy follows the same trend as the $\angle N1EN2$ bond angle and the ΔE_{st} . In other words, the model calculations demonstrate that the values of ΔE_{st} can be used as a criterion to predict the reactivity of seven-member **7-Rea-E** compounds.

3.5. Geometries and electronic structures of dimerization reactions

The dimerization reaction of the seven-member **7-Rea-E** molecule was examined in this work in order to understand more about their kinetic stability. Selected geometrical parameters along the pathway, shown in Eq. (3) and computed at the B3LYP/LANL2DZ + dp level, are collected in **Figure 5**. The relative energies at the same level of theory are listed in **Table 3**. **Figure 5** and **Table 3** have several noteworthy features.

Firstly, as predicted, a double bond between the two group 14 E atoms should be formed during the dimerization reaction of two **7-Rea-E** molecules. However, repeated attempts to determine the transition state for the concerted dimerization of two **7-Rea-E** compounds, using the B3LYP/LANL2DZ + dp level of theory, are always unsuccessful. That is to say, no transition states exist on the B3LYP surface for such dimerization reactions. Further, the B3LYP calculations demonstrate that all five dimers (i.e., **7-Pro-C-3**, **7-Pro-Si-3**, **7-Pro-Ge-3**, **7-Pro-Sn-3** and **7-Pro-Pb-3**) do not have the imaginary frequency. Therefore, they can be considered as true minima on the potential energy surfaces. As stated earlier, unfortunately, because of a lack of experimental and data on such species, geometrical information studied in this work should be considered as predictions for future investigations.

Secondly, as demonstrated in **Figure 4**, the E = E bond length in the dimer molecule was calculated to decrease in the order: 1.436 Å (**7-Pro-C-3**) < 2.491 Å (**7-Pro-Si-3**) < 2.602 Å (**7-Pro-Ge-3**) < 2.941 Å (**7-Pro-Sn-3**) < 3.493 Å (**7-Pro-Pb-3**), which correlates with the atomic size of the main group 14 element, E, as it changes from carbon to lead. It must be stressed that the computed E = E double bond lengths are somewhat larger than the experimental values (1.356 [65, 66], 2.139–2.360 [67, 68], 2.212–2.509 [69, 70], 2.601–2.961 [71, 72] and 2.990–3.537 [73, 74] Å, for C=C, Si=Si, Ge=Ge, Sn=Sn and Pb=Pb, respectively). The former

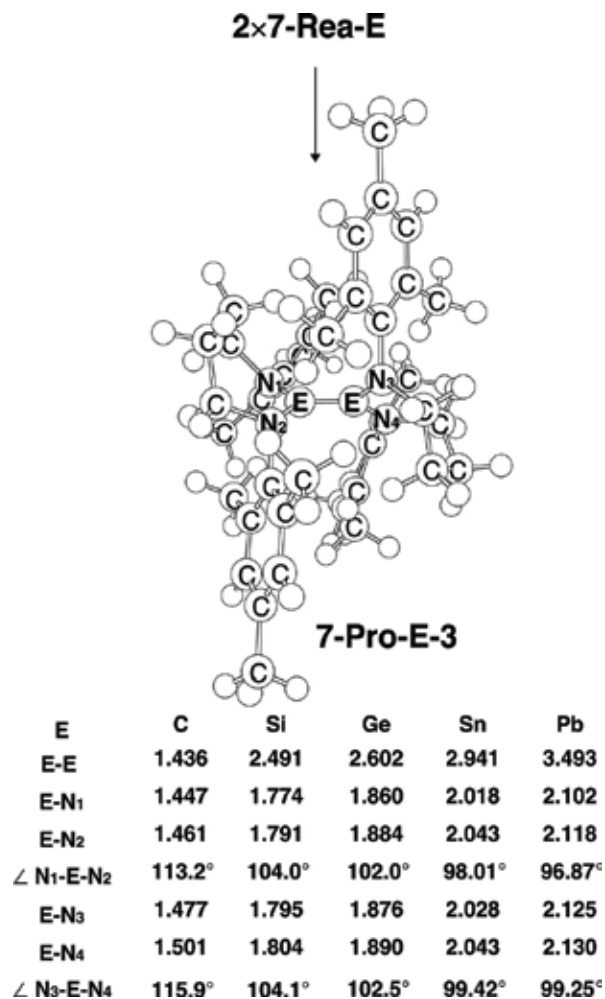


Figure 5. B3LYP/LANL2DZ + dp optimized geometries (in Å and deg) of the dimer products of 7-Rea-E (E = C, Si, Ge, Sn, and Pb). The relative energies for each species see Table 3. Hydrogens are omitted for clarity.

System	ΔH^{\ddagger} (kcal mol ⁻¹)	ΔG^{\ddagger} (kcal mol ⁻¹)
7-Rea-C	+9.31	+16.3
7-Rea-Si	+13.1	+21.0
7-Rea-Ge	+20.7	+28.7
7-Rea-Sn	+23.0	+31.2
7-Rea-Pb	+44.1	+56.0

¹All were calculated at the B3LYP/LANL2DZ + dp level of theory. The B3LYP optimized structures of the stationary points see Figure 5.

²The reaction enthalpy of the product, relative to the corresponding reactants.

³The Gibbs free enthalpy of the product, relative to the corresponding reactants.

Table 3. Relative energies for the dimerization reaction of the singlet group 14 7-Rea-E species: Reactants (2 7-Rea-E) → dimerization product (7-Pro-E-3)¹.

computed values might be attributable to steric effects, which cause the dimer formed by seven-member N-heterocyclic carbene analogues to have a longer double bond distance than the less substituted dimetallene itself. However, the DFT calculations show that the energy of the final product (dimers), relative to its corresponding reactants, is 33 (**7-Pro-C-3**), 38 (**7-Pro-Si-3**), 43 (**7-Pro-Ge-3**), 49 (**7-Pro-Sn-3**) and 54 (**7-Pro-Pb-3**) kcal/mol. Also, as seen in **Table 3**, the difference in the values of ΔG between the reactants and the dimer are 46, 58.4, 55, 57 and 68.2 kcal/mol, for carbon, silicon, germanium, tin and lead species, respectively. Consequently, the computational results predict that the dimerization reaction should not occur during the formation of the seven-member **7-Rea-E** (E = C, Si, Ge, Sn and Pb) species at room temperature.

4. Conclusion

This study uses the B3LYP level of theory to study the mechanisms and reactivity for three types of chemical reactions of carbene analogues, **7-Rea-E** (E = C, Si, Ge, Sn and Pb), which possess a seven-member-ring. It should be noted that this study provides the first theoretical demonstration of the reaction trajectory and the first theoretical estimation of the activation energy and the reaction enthalpy for these chemical processes. In relation to the aforementioned five seven-member heavy carbene systems and their related chemical reactions, as studied in this paper, the following conclusions can be drawn:

1. With regard to both the activation barrier and the reaction enthalpy, based on the model calculations presented here, it is concluded that the seven-member **7-Rea-E** reactivity order is as follows: **7-Rea-C** > **7-Rea-Si** > **7-Rea-Ge** > **7-Rea-Sn** > **7-Rea-Pb**. In other words, a **7-Rea-E** molecule possessing a group 14 atom, E, of lower atomic number accelerates chemical reactions, whereas a **7-Rea-E** compound bearing a group 14 atom, E, of higher atomic number hinders reactions. From this conclusion, it is predicted that the heavy carbene analogues with a seven-membered ring can be synthesized and isolated. Indeed, it was recently reported that the stable carbon(II) and lead(II) compounds bearing a seven-membered ring, the so-called dialkylcarbene (**7-Rea-C**) and dialkylplumbylene, have been synthesized and structurally characterized [48–50, 58].
2. This theoretical work suggests that seven-member cyclic **7-Rea-E** compounds that feature a lighter group 14 element, E (such as **7-Rea-C** and **7-Rea-Si**) should be moisture-sensitive, whereas the seven-member heavy carbene analogues (such as **7-Rea-Sn** and **7-Rea-Pb**) are moisture-stable compounds.
3. This theoretical work reveals that the [1 + 2] imine cycloadditions of seven-member **7-Rea-E** molecules produces the final cycloadduct in a concerted manner. That is, these cycloadditions proceed stereospecifically and result in cycloproducts that retain their stereochemistry.
4. These theoretical investigations strongly suggest that the dimerization reaction should not occur during the formation of the seven-member **7-Rea-E** (E = C, Si, Ge, Sn and Pb) species. Indeed, this theoretical conclusion is in good agreement with the available experimental observations [48–50].

5. This study shows that knowledge of the singlet-triplet splitting (ΔE_{st}) of the seven-member carbene analogues **7-Rea-E** is of great importance in achieving a deeper understanding of their reactivity, since it is the driving force for the related reactions.
6. This study demonstrates that the heavier the atomic weight of group 14 elements, E, involved in the seven-member **7-Rea-E**, the larger is the ΔE_{st} , the higher is the activation barrier and the smaller is the enthalpy of its final product. Consequently, based on these theoretical conclusions, it is easily predicted that the heavier seven-member **7-Rea-E** (such as E = Si, Ge, Sn and Pb) should be readily synthesized and isolated at room temperature.

Acknowledgements

The authors are grateful to the National Center for High-Performance Computing of Taiwan for generous amounts of computing time and to the Ministry of Science and Technology of Taiwan for the financial support.

Author details

Zheng-Feng Zhang¹, Ling-Hsuan Liu¹ and Ming-Der Su^{1,2*}

*Address all correspondence to: midesu@mail.ncyu.edu.tw

¹ Department of Applied Chemistry, National Chiayi University, Chiayi, Taiwan

² Department of Medicinal and Applied Chemistry, Kaohsiung Medical University, Kaohsiung, Taiwan

References

- [1] Arduengo AJ III, Harlow RL, Kline M. A stable crystalline carbene. *Journal of the American Chemical Society*. 1991;**113**:361-363
- [2] Arduengo AJ III. Looking for stable Carbenes: The difficulty in starting anew. *Accounts of Chemical Research*. 1999;**32**:913-921
- [3] Mendoza-Espinosa D, Donnadiou B, Bertrand G. Synthesis of 4- and 4,5-functionalized Imidazol-2-ylidenes from a single 4,5-Unsubstituted Imidazol-2-ylidene. *Journal of the American Chemical Society*. 2010;**132**:7264-7265 and related references therein
- [4] Martin D, Baceiredo A, Gornitzka H, Schoeller WW, Bertrand G. A stable P-heterocyclic Carbene. *Angewandte Chemie International Edition*. 2005;**44**:1700-1703
- [5] Hahn FE, Langenhahn V, Luegger T, Pape T, Le Van D. Template synthesis of a coordinated Tetracarbene Ligand with crown ether topology. *Angewandte Chemie International Edition*. 2005;**44**:3759-3763

- [6] Krahulic KE, Tuononen HM, Parvez M, Roesler R. Isolation of free Phenylide-like Carbanions with N-heterocyclic Carbene frameworks. *Journal of the American Chemical Society*. 2009;**131**:5858-5865
- [7] Martin D, Melaimi M, Soleilhavoup M, Bertrand G. A brief survey of our contribution to stable Carbene chemistry. *Organometallics*. 2011;**30**:5304-5313
- [8] Herrmann WA, Köcher C. N-heterocyclic Carbenes. *Angewandte Chemie International Edition*. 1997;**36**:2162-2187
- [9] Bourissou D, Guerret O, Gabbai FP, Bertrand G. Stable Carbenes. *Chemical Reviews*. 2000;**100**:39-92
- [10] Nai V, Bindu S, Sreekumar V. N-heterocyclic Carbenes: Reagents, not just Ligands! *Angewandte Chemie International Edition*. 2004;**43**:5130-5135
- [11] Canac Y, Soleilhavoup M, Conejero S, Bertrand G. Stable non-N-heterocyclic carbenes (non-NHC): Recent progress. *Journal of Organometallic Chemistry*. 2004;**689**:3857-3865
- [12] Hahn FE, Jahnke MC. Heterocyclic Carbenes: Synthesis and coordination chemistry. *Angewandte Chemie International Edition*. 2008;**47**:3122-3172
- [13] Vignolle J, Cattoën X, Bourissou D. Stable noncyclic singlet Carbenes. *Chemical Reviews*. 2009;**109**:3333-3384
- [14] Tapu D, Dixon DA, Roe C. ¹³C NMR spectroscopy of "Arduengo-type" Carbenes and their derivatives. *Chemical Reviews*. 2009;**109**:3385-3407
- [15] Arnold PL, Casely IJ. F-block N-heterocyclic Carbene complexes. *Chemical Reviews*. 2009;**109**:3599-3611
- [16] Díez-González S, Marion N, Nolan SP. N-heterocyclic Carbenes in late transition metal catalysis. *Chemical Reviews*. 2009;**109**:3612-3676
- [17] Poyatos M, Mata JA, Peris E. Complexes with poly(N-heterocyclic carbene) Ligands: Structural features and catalytic applications. *Chemical Reviews*. 2009;**109**:3677-3707
- [18] Samojłowicz C, Bieniek M, Grela K. Ruthenium-based olefin metathesis catalysts bearing N-heterocyclic Carbene Ligands. *Chemical Reviews*. 2009;**109**:3708-3742
- [19] Van Otterlo WA, de Koning CB. Metathesis in the synthesis of aromatic compounds. *Chemical Reviews*. 2009; **109**:3743-3782.
- [20] Monfette S, Fogg DE. Equilibrium ring-closing metathesis. *Chemical Reviews*. 2009; **109**:3783-3816
- [21] Alcaide B, Almendros P, Luna A. Grubbs' ruthenium-Carbenes beyond the metathesis reaction: Less conventional non-Metathetic utility. *Chemical Reviews*. 2009;**109**: 3817-3858
- [22] Hindi KM, Panzner MJ, Tessier CA, Cannon CL, Youngs WJ. The medicinal applications of Imidazolium Carbene-metal complexes. *Chemical Reviews*. 2009;**109**:3859-3884

- [23] Kato T, Maerten E, Baceiredo A. Non-NHCs Stable Singlet Carbene Ligands. *Topics in Organometallic Chemistry*. 2010;**30**:131-147
- [24] Dubinina GG, Furutachi H, Vicic DA. Active Trifluoromethylating agents from well-defined copper(I)-CF₃ complexes. *Journal of the American Chemical Society*. 2008;**130**:8600-8601
- [25] Jana A, Schulzke C, Roesky HW. Oxidative addition of Ammonia at a silicon(II) center and an unprecedented hydrogenation reaction of compounds with low-Valent group 14 elements using Ammonia Borane. *Journal of the American Chemical Society*. 2009;**131**:4600-4601
- [26] Hällner L, Page MJ, Macgregor SA, Mahon MF, Whittlesey MK. Allylic rearrangements. XLI. The reaction of Thionyl chloride with steroid Allylic alcohols. *Journal of the American Chemical Society*. 2009;**131**:4604-4606
- [27] Jeong W, Shin EJ, Culkin DA, Hedrick JL, Waymouth RM. Zwitterionic polymerization: A kinetic strategy for the controlled synthesis of cyclic Poly lactide. *Journal of the American Chemical Society*. 2009;**131**:4884-4891
- [28] Boydston AJ, Holcombe TW, Unruh DA, Fréchet MJ, Grubbs RH. A direct route to cyclic organic nanostructures via ring-expansion metathesis polymerization of a Dendronized macromonomer. *Journal of the American Chemical Society*. 2009;**131**:5388-5389
- [29] Aktas H, Sloatweg JC, Schakel M, Ehlers AW, Lutz M, Spek AL, Lammertsma K. N-heterocyclic Carbene-functionalized ruthenium Phosphinidenes: What a difference a twist makes. *Journal of the American Chemical Society*. 2009;**131**:6666-6667
- [30] Iwai T, Fujihara T, Terao J, Tsuji Y. Iridium-catalyzed addition of acid chlorides to terminal alkyenes. *Journal of the American Chemical Society*. 2009;**131**:6668-6669
- [31] Galan BR, Pitak M, Gembicky M, Keister JB, Diver ST. Ligand-promoted Carbene insertion into the aryl substituent of an N-heterocyclic Carbene Ligand in ruthenium-based metathesis catalysts. *Journal of the American Chemical Society*. 2009;**131**:6822-6832
- [32] Xiong Y, Yao S, Driess M. An isolable NHC-supported Silanone. *Journal of the American Chemical Society*. 2009;**131**:7562-7563
- [33] Zeng X, Frey GD, Kinjo R, Donnadie B, Bertrand G. Synthesis of a simplified version of stable bulky and rigid cyclic (alkyl)(amino)carbenes, and catalytic activity of the ensuing gold(I) complex in the three-component preparation of 1,2-Dihydroquinoline derivatives. *Journal of the American Chemical Society*. 2009;**131**:8690-8696
- [34] Chiang P-C, Rommel M, Bode JW. α' -Hydroxyenones as mechanistic probes and scope-expanding surrogates for α,β -unsaturated Aldehydes in N-heterocyclic Carbene-catalyzed reactions. *Journal of the American Chemical Society*. 2009;**131**:8714-8718
- [35] Lavallo V, Canac Y, Donnadiu B, Schoeller WW, Bertrand G. Cyclopropenylidenes: From interstellar space to an isolated derivative in the laboratory. *Science*. 2006;**312**:722-724

- [36] Despagnet-Ayoub E, Grubbs RH. A stable four-Membered N-heterocyclic Carbene. *Journal of the American Chemical Society*. 2004;**126**:10198-10199
- [37] Despagnet-Ayoub E, Grubbs RH. A ruthenium olefin metathesis catalyst with a four-Membered N-heterocyclic Carbene Ligand. *Organometallics*. 2005;**24**:338-340
- [38] Enders D, Breuer K, Raabe G, Runsink J, Teles JH, Melder J, Ebel K, Brode S. Preparation, structure, and reactivity of 1,3,4-Triphenyl-4,5-dihydro-1H-1,2,4-triazol-5-ylidene, a new stable Carbene. *Angewandte Chemie International Edition in English*. 1995;**34**:1021-1023
- [39] Krahulic KE, Tuononen HM, Parvez M, Roesler R. Isolation of free Phenylide-like Carbanions with N-heterocyclic Carbene frameworks. *Journal of the American Chemical Society*. 2009;**131**:5858-5865
- [40] Mendoza-Espinosa D, Donnadiou B, Bertrand G. Synthesis of 4- and 4,5-functionalized Imidazol-2-ylidenes from a single 4,5-Unsubstituted Imidazol-2-ylidene. *Journal of the American Chemical Society*. 2010;**132**:7264-7265 and related references therein
- [41] Alder RW, Blake ME, Bortolotti C, Bufali S, Butts CP, Linehan E, Oliva JM, Orpen AG, Quayle M. Complexation of stable carbenes with alkali metals. *Chemical Communications*. 1999;**0**:241-242
- [42] Mayr M, Wurst K, Ongania K-H, Buchmeiser MR. 1,3-Dialkyl- and 1,3-Diaryl-3,4,5,6-tetrahydropyrimidin-2-ylidene rhodium(I) and palladium(II) complexes: Synthesis, structure, and reactivity. *Chemistry-A European Journal*. 2004;**10**:1256-1266
- [43] Driess M, Yao S, Brym M, Wüllen CV. A Heterofulvene-like Germylene with a Betain reactivity. *Angewandte Chemie International Edition*. 2006;**45**:4349-4352
- [44] Yao S, Brym M, van WC, Dries M. From a stable Silylene to a mixed-Valent Disiloxane and an isolable Silaformamide-Borane complex with considerable silicon-oxygen double-bond character. *Angewandte Chemie International Edition*. 2007;**46**:4159-4162
- [45] Bazinet P, Ong T-G, O'Brien JS, Lavoie N, Bell E, Yap GPA, Korobkov I, Richeson DS. Design of Sterically Demanding, electron-rich Carbene Ligands with the Perimidine scaffold. *Organometallics*. 2007;**26**:2885-2895
- [46] Gómez-Bujedo S, Alcarazo M, Pichon C, Alvarez E, Fernández R, Lassaletta JM. Isoquinolin-1-ylidenes as electronically tuneable ligands. *Chemical Communications*. 2007;**0**:1180-1182
- [47] Yao S, Wullen C van, Sun, X-Y, Driess M. Dichotomic Reactivity of a Stable Silylene toward Terminal Alkynes: Facile C—H Bond Insertion versus Autocatalytic Formation of Silacycloprop-3-ene. *Angewandte Chemie International Edition*. 2008;**47**:3250-3253.
- [48] Jazzar R, Liang H, Donnadiou B, Bertrand G. A new synthetic method for the preparation of protonated-NHCs and related compounds. *Journal of Organometallic Chemistry*. 2006;**691**:3201-3205

- [49] Iglesias M, Beetstra DJ, Stasch A, Horton PN, Hursthouse MB, Coles SJ, Cavell KJ, Dervisi A, Fallis IA. First examples of Diazepanylidene Carbenes and their late-transition-metal complexes. *Organometallics*. 2007;**26**:4800-4809
- [50] Iglesias M, Beetstra DJ, Knight JC, Ooi L-L, Stasch A, Coles S, Male L, Hursthouse MB, Cavell KJ, Dervisi A, Fallis IA. Novel expanded ring N-heterocyclic Carbenes: Free Carbenes, silver complexes, and structures. *Organometallics*. 2008;**27**:3279-3289
- [51] Frisch MJ, Trucks GW, Schlegel HB, Scuseria GE, Robb MA, Cheeseman JR, Scalmani G, Barone V, Mennucci B, Petersson GA. et al. Gaussian, Inc., Wallingford CT; 2013
- [52] Check CE, Faust TO, Bailey JM, Wright BJ, Gilbert TM, Sunderlin LS. Addition of polarization and diffuse functions to the LANL2DZ basis set for P-block elements. *The Journal of Physical Chemistry A*. 2001;**105**:8111-8116
- [53] Carroll FA. In: *Perspectives on Structure and Mechanism in Organic Chemistry*. New York: Brooks/Cole Company; 1998. p. 275
- [54] Pyykkö P, Desclaux J-P. Relativity and the periodic system of elements. *Accounts of Chemical Research*. 1979;**12**:276-281
- [55] Kutzelnigg W. Chemical bonding in higher main group elements. *Angewandte Chemie International Edition in English*. 1984;**23**:272-295
- [56] Pyykkö P. Relativistic effects in structural chemistry. *Chemical Reviews*. 1988;**88**:563-594
- [57] Pyykkö P. Strong closed-shell interactions in inorganic chemistry. *Chemical Reviews*. 1997;**97**:597-636
- [58] Izod K, McFarlane W, Wills C, Clegg W, Harrington RW. Agostic-type B-H...Pb interactions stabilize a Dialkylplumbylene. Structure of and bonding in $[\{n\text{Pr}_2\text{P}(\text{BH}_3)\}(\text{Me}_3\text{SiC}(\text{CH}_2)_2)_2\text{Pb}]$. *Organometallics*. 2008;**27**:4386-4394
- [59] Hammond GS. A correlation of reaction rates. *Journal of the American Chemical Society*. 1955;**77**:334-338
- [60] Shaik S, Schlegel HB, Wolfe S. In: *Theoretical Aspects of Physical Organic Chemistry*. USA: John Wiley & Sons Inc.; 1992
- [61] Pross, A. In: *Theoretical and Physical Principles of Organic Reactivity*. USA: John Wiley & Sons Inc.; 1995.
- [62] Shaik S, Hiberty PC. In: *A Chemist's Guide to Valence Bond Theory*. USA: Interscience, Wiley; 2008
- [63] Su M-D. Theoretical study on the Reactivities of Stannylene and Plumbylene and the origin of their activation barriers. *Chemistry-A European Journal*. 2004;**10**:6073-6084
- [64] Su M-D. Role of Spin-Orbit Coupling and Symmetry in Triplet Carbenic Addition Chemistry. *The Journal of Physical Chemistry*. 1996;**100**:4339-4349; and related references therein.

- [65] Raabe G, Michl J. Multiple bonding to silicon. *Chemical Reviews*. 1985;**85**:419-509
- [66] West R. Chemistry of the silicon-silicon double bond. *Angewandte Chemie International Edition*. 1987;**26**:1201-1211
- [67] Kinjo R, Ichinohe M, Sekiguchi A, Takagi N, Sumimoto M, Nagase S. Reactivity of a Disilyne $\text{RSi}\equiv\text{SiR}$ ($\text{R} = \text{Si}^i\text{Pr}[\text{CH}(\text{SiMe}_3)_2]_2$) toward π -bonds: Stereospecific addition and a new route to an isolable 1,2-Disilabenzene. *Journal of the American Chemical Society*. 2007;**129**:7766-7767
- [68] Iwamoto T, Kobayashi M, Uchiyama K, Sasaki S, Nagendran S, Isobe H, Kira M. Anthryl-substituted Trialkyldisilene showing distinct Intramolecular charge-transfer transition. *Journal of the American Chemical Society*. 2009;**131**:3156-3157
- [69] Simons RS, Pu L, Olmstead MM, Power PP. Synthesis and characterization of the Monomeric Diaryls $\text{M}\{\text{C}_6\text{H}_3\text{-}2,6\text{-Mes}_2\}_2$ ($\text{M} = \text{Ge}, \text{Sn}, \text{or Pb}$; $\text{Mes} = 2,4,6\text{-Me}_3\text{C}_6\text{H}_2\text{-}$) and Dimeric aryl-metal chlorides $[\text{M}(\text{Cl})\{\text{C}_6\text{H}_3\text{-}2,6\text{-Mes}_2\}]_2$ ($\text{M} = \text{Ge}$ or Sn). *Organometallics*. 1997;**16**:1920-1925
- [70] Schäfer H, Saak W, Weidenbruch M. Azadigermiridines by addition of diazomethane or Trimethylsilyldiazomethane to a Digermene. *Organometallics*. 1999;**18**:3159-3163
- [71] Klinkhammer KW, Fässler TF, Grützmacher H. The formation of Heteroleptic Carbene homologues by Ligand exchange—Synthesis of the first Plumbanediyl Dimer. *Angewandte Chemie International Edition*. 1998;**37**:124-126
- [72] Drost C, Hitchcock PB, Lappert MF. Thermally stable Heterobinuclear bivalent group 14 metal complexes $\text{Ar}_2\text{M-Sn}[1,8\text{-(NR)}_2\text{C}_{10}\text{H}_6]$ ($\text{M}=\text{Ge}, \text{Sn}$; $\text{Ar}=2,6\text{-(Me}_2\text{N)}_2\text{C}_6\text{H}_3$; $\text{R}=\text{CH}_2\text{tBu}$). *Angewandte Chemie International Edition*. 1999;**38**:1113-1116
- [73] Stürmann M, Saak W, Weidenbruch M, Klinkhammer KW. A Heteroleptic Diplumbene and a magnesium Dibromide stabilized Plumbylene Dimer. *European Journal of Inorganic Chemistry*. 1999;**4**:579-582
- [74] Stürmann M, Saak W, Marsmann H, Weidenbruch M. Tetrakis(2,4,6-triisopropylphenyl) diplumbene: A molecule with a lead-lead double bond. *Angewandte Chemie International Edition*. 1999;**38**:187-189

Edited by Saravanan Chandraleka

The book “Chemical Reactions in Inorganic Chemistry” describes an overview of chemical reagents used in inorganic chemical reactions for the synthesis of different compounds including coordination, transition metal, organometallic, cluster, bioinorganic, and solid-state compounds. This book will be helpful for the graduate students, teachers, and researchers, and chemistry professionals who are interested to fortify and expand their knowledge about sol-gel preparation and application, porphyrin and phthalocyanine, carbon nanotube nanohybrids, triple bond between arsenic and group 13 elements, and N-heterocyclic carbene and its heavier analogues. It comprises a total of five chapters from multiple contributors around the world including China, India, and Taiwan.

Published in London, UK
© 2018 IntechOpen
© Nikolay Tsuguliev / iStock

IntechOpen

